Aerial Sensing Platform for Greenhouses

Thesis

Presented in Partial Fulfillment of the Requirements for the Degree Master of Science in

the Graduate School of The Ohio State University

By

Aditya Raj

Graduate Program in Food, Agricultural & Biological Engineering

The Ohio State University

2021

Thesis Committee

Dr. Peter Ling

Dr. Sami Khanal

Dr. Heping Zhu

Abstract

Precision variable-rate sprayers regulate the spray dosage based on the canopy density of plants; hence a precise structural measurement is essential. Although a ground-based acquisition system mounted with laser sensors can accurately extract plant dimension, an indoor greenhouse environment presents several structural limitations in capturing multiple views of the canopy to prevent occlusions. Consequently, a mini-unmanned aerial vehicle (UAV) was chosen to mount the sensors allowing greater mobility and maneuverability. The system integrated UAV's control system, a 2D laser range sensor, a vision-based positioning system, an onboard microcomputer, and a ground computer using Robot Operating System (ROS). The study developed customized algorithms for autonomous UAV control independent of GPS signal availability, offline processing of point cloud, and graphical user interface (GUI) to simplify human-machine interaction. The autonomous navigation performance was evaluated in a GPS-denied environment by calculating the deviation, performing a second-order regression of the UAV position from a straight line reference, and evaluating variation in flight parameters. The deviation in positions reduced (88, 75, 60, 68 cm), and the coefficient of determination (R^2) increased (0.971, 0.986, 0.998, 0.998) as the speed increased (0.6, 0.8, 1.0, and 1.2 m/s) and shorter duration flights were more stable. Additionally, the performance of UAV attitude control was evaluated using barometric height feedback and compared to more accurate range

sensor derived height feedback, both resulted in similar performance with overall

deviation under 5 cm. The effect of propellers downdraft on plant measurement was

evaluated by mounting aerial platform on a constant speed track and comparing the

measurements under varying sensor inclinations, and propeller running with propeller

turned off. The length and height measurements were stable beyond 40 cm of UAV with

0° inclination, and width measurements had the least variation with 35° inclination within

100 cm of UAV.

Keywords: UAV, LiDAR, Guidance, Autonomous Control, Indoor Navigation, Altitude

Control, Path Planning, Downdraft

Acknowledgments

No words are sufficient to describe the gratitude I have towards Dr. Peter Ling to provide his unceasing guidance, vision, and support that helped transform a farfetched idea into reality. I consider myself extremely fortunate to have received the creative environment, freedom, and platform while pursuing my master's degree at Ohio State under his mentorship, which has helped reshape my life goal and career.

I would also like to thank Dr. Sami Khanal and Dr. Heping Zhu for providing their technical expertise and directions, which cleared the pathway leading to my research goal. I thank Scott Wolfe for his continuous, prompt, and ingenious solutions that helped us preserve invaluable research hours. I am obliged for all the time he spent in the greenhouse and laboratory and training me to fly the drone. Without his support, I could not see this project reaching its completion.

As an international student, I would like to thank Candy McBride for her swift support and guidance in keeping my master's journey smooth and free from any unpleasant surprises. I thank my fellow graduate student and a great friend Uchit Nair for his technical and psychological support during challenging situations.

I thank Ramon Salcedo, Luis Huezo, Kaylee South, Asmita Khanal, Anirudh Akula, Shyam Sivaprasad, Parisa Nazemi, and Andrea Landaverde for their long-lasting bond of friendship and filling every day with joy and excitement.

I would also like to thank my family members Nikita Khozin, Samuel Khozin, and Dora Khozin, for their love and support throughout my master's carrier. Finally, I thank my mother for fueling my strength and fighting spirit, which I needed every day to reach my goal.

Vita

2009–2013 ………………………..B.Tech Electronics and Communnication
                                   Engineering, Integral University, India

2014-2018………………………… System Engineer, Tata Consultancy Services, India

2018-Present………………………MSc. Food, Agricultural and Biological Engineering,
                                   The Ohio State University

Fields of Study

Major Field: Food, Agricultural, and Biological Engineering

Table of Contents

List of Tables

List of Figures

xii

xvi

xvii

Chapter 1. Introduction

1.1 Background

Controlled Environment Agriculture (CEA) provides microclimate control to achieve optimum environmental conditions for crops, enabling year-round production capability, higher yield, and increased control over plant growth than open-field farming systems (Duarte-Galvan et al., 2012). Although these artificial conditions promote plant growth, it creates a conducive environment for pest infestation (Sammons et al., 2005). Consequently, extensive use of pesticides is a common practice among greenhouse growers. However, incorrect pesticide application rates can result in over or under applications, reducing efficiency in terms of economic costs, groundwater pollution, and impact on human health (Miranda-Fuentes et al., 2016). Moreover, pesticide overuse increases production costs and has adverse health effects, and excess runoff can lead to soil, ground, and surface water pollution (Abhilash and Singh, 2009; Sharma et al., 2019). Exposure to pesticides can have a detrimental impact on human health, primarily due to the absorption of aerosols absorption through the skin, inhalation, and consuming food with pesticide residues (Hernández et al., 2003; Nuyttens et al., 2009). Additionally,

high humidity levels and air temperature of the greenhouse amplify pesticide exposure risk compared to the open-field application (Archibald et al., 1995).

Handheld spraying is the most commonly used methodology in greenhouses due to its simplicity and adaptability to any greenhouse structure (Derksen et al., 2007). However, spray uniformity primarily depends on the skill of the operator. Considering the scale of commercial greenhouses, manual operation can be time-consuming and tedious, making it prone to errors and leading to economic losses and health hazards. The use of mechanized systems can help overcome these drawbacks (Pilarski et al., 2002; Sezen, 2003; Henten et al., 2000). Nuyttens et al. (2004) compared the level of total body exposure in a greenhouse to pesticides using a handheld spray gun, a spray lance, a self-propelled vehicle (Fumimatic), and a manually pulled trolley. Compared to the spray gun (100%), the mechanized Fumimatice had the least human exposure (1%) among the group.

However, a mechanized system spraying can be inefficient at a constant rate since it cannot adjust its spray rate whether there are plants in the area or not, not with canopy variation in shape and size. Precise spray dose adjustments can result in a controlled pesticide application, reducing the overuse and its harmful effects (Gil et al., 2007; Llorens et al., 2011; Solanelles et al., 2006; Stajnko et al., 2012). Previous studies have shown that the plant geometry or canopy variation influences the spray rate; consequently, accurate determination of the plant dimensions has been a field of extensive research (Chen et al., 2012; Escolà et al., 2011; Gil et al., 2007; Rosell et al., 2009; Siegfried et al., 2007; Walklate et al., 2002; Wei and Salyani, 2004). Gil et al.

(2007) showed that variable-rate sprayers with the capability of extracting plant structure had similar spray penetration and coverage to constant rate sprayers, whereas the spray consumption was 41.2% of constant rate sprayers. A variable-rate sprayer capable of synchronizing its spray rate with the variability of canopy characteristics has shown a significant reduction in pesticide losses compared to constant rate sprayers (Chen et al., 2012, 2013; Jeon and Zhu, 2012).

Sophisticated instruments such as cameras, ultrasonic sensors, radar sensors, and ranging sensors are mounted on a moving platform to extract plant structural information. However, the current research focuses on the greenhouse environment, which can limit the selection scope of the sensors and sensing platform. Most of the studies have focused on utilizing farm machines such as tractors as scanning platforms, which could be infeasible for a greenhouse environment due to limited maneuverability in enclosed space where greenhouse plants are tightly spaced. Hence it was necessary to investigate alternative mobile platforms suitable for greenhouse application.

1.2 Objectives

This research aimed to evaluate the feasibility of using an aerial sensing platform for plant characterization in the greenhouse environment. Specific objectives of this research -

- Establish an aerial sensing platform including sensor selection, data collection, and map generation,

- Develop an autonomous flight control system for flight path planning and autonomous navigation,

- Evaluate autonomous flight control performance along a single path

- Document downdraft effect on the plant measurements

1.3 Thesis Organization

This study investigates the challenges of the greenhouse environment and establishes a sensing platform capable of extracting the highest quality plant data. Chapter 2 investigates the selection of sensing platforms based on existing works, followed by a review of indoor positioning systems to address the unavailability of GPS signals. Chapter 2 also focuses on path planning and automation of aerial platforms, followed by the limitation of the selected platform affecting the data quality. The final section of chapter 2 focuses on the sensor selection criterion. Chapter 3 discusses the materials and methods used to achieve the desired objectives. Chapter 4 evaluates the results of the experiments conducted, including the discussion. The final chapter (Chapter 5) presents the conclusion of the thesis and recommendations for future study.

Chapter 2. Literature Review

2.1 Mobile Sensing Systems

2.1.1 Irrigation boom based scanner

Specific to the greenhouse application, a 2-D line scanner or LiDAR (Light Detection

And Ranging) sensor was mounted on an irrigation/spray boom to extract dimensions of

underlying crops (Yan et al., 2018). However, commercial greenhouses usually comprise

multiple bays with separate sprayers, and such a design would require mounting the

sensing platform and data acquisition system on each and every sprayer boom, making it

undesirable.

Moreover, due to the limited operating range of the LiDAR, its accuracy in measuring

plant width deteriorated as the plants moved away from the LiDAR's mounting location.

This limitation can be attributed to the shape and size of LiDAR's footprint, which is

circular at the center and becomes more ellipsoidal as it moves away from the center,

reducing the beam intensity and resulting in poorer resolution (Pang et al., 2011). The

study also found that the measurement accuracy deteriorated as the spacing between the

objects reduced, presenting a challenge while scanning tightly spaced greenhouse crops.

It is primarily caused due to the inability of LiDAR to penetrate the farther plants and

reach the ground. Since the LiDAR only captured a single perspective of the plants, it

could not generate the plant's complete geometry, whereas previous studies have shown

that complete reconstruction of plants requires bidirectional scanning for complete

reconstruction (Arnó et al., 2013; Rosell et al., 2009). Since the boom can travel only in

forward/backward direction and lateral movement is restricted, it cannot overcome

previously mentioned limitations. Although mounting multiple LiDARs on a single boom

can overcome this limitation, it will increase the setup cost and require costly

modification to existing greenhouse structures. Given the scale of commercial

greenhouses, such a design will be economically and computationally infeasible.

2.1.2 Unmanned Ground vehicles

A more practical solution is using a mobile robot that can carry the sensing platform

across the greenhouse, thereby eliminating multiple sensing platforms. Wheeled robots

have been used in greenhouses for automated spraying to reduce manual effort and

maintain accuracy, uniformity, and time efficiency for repetitive maintenance tasks.

Grounded steel pipes and hot water pipes are ubiquitous for greenhouses, providing a

path for rolling the wheeled robots (Gan-Mor et al., 1996; Rafiq et al., 2014; Sammons et

al., 2005). Although pipes were spread across the greenhouse floor, Sammons et al.

(2005) had to manually move the robot to the next row, making the process discontinuous

and requiring manual effort to switch rows. Later works focused on developing robots

that used self-localization techniques to estimate their relative greenhouse location

allowing autonomous navigation (Durmus et al., 2016; Harik and Korsaeth, 2018; Hyuc

Ko et al., 2014; Ko et al., 2015; Wu et al., 2020). Despite having the advantage of

navigating along the crop boundary and high payload capacity, they cannot reach the

crops far away from the boundary. Additionally, greenhouse growers utilize most of the

floor space for plants reducing the available pathways for navigating ground robots to scan the crops from multiple viewing angles. These limitations restrict the sensors ability to acquire high-quality data for plant characterization.

2.1.3 Unmanned Aerial Vehicles

Overcoming the mentioned limitations requires the sensing platform to navigate freely through the greenhouse dimensions. Consequently, a mini Unmanned Aerial Vehicle (UAV) has the potential to be used for this purpose (Roldán et al., 2015). The past decade has witnessed unprecedented growth in the UAV application in the field of agriculture, such as vineyard management (Campos et al., 2019; Comba et al., 2015, 2015; Nolan et al., 2015; Primicerio et al., 2012; Turner et al., 2011), forestry (Chisholm et al., 2013; Getzin et al., 2012; Merino et al., 2012; Rokhmana, 2015), and animal detection (Israel, 2012; Ward et al., 2016). The primary reasons for the growth in UAV-based agriculture applications are their small size, affordable cost, and off-the-shelf availability. Moreover, UAVs are easy to transport, integrate with multiple sensors, and customize based on user requirements. The National Purchase Diary Panel (NPD) in 2017 reported that UAV sales were more than doubled for that year, increasing at a rate of 117% each year, and growing technology is comparable to the cellular revolution (Sylvester, 2018).

 Previous studies have used a wide variety of UAV mounted sensors such as RGB cameras (Jannoura et al., 2015; Schirrmann et al., 2016), multispectral camera (Caturegli et al., 2016; Vega et al., 2015), hyperspectral camera (Aasen et al., 2015; Uto et al., 2013), thermal camera (Aasen et al., 2015; Santesteban et al., 2017), NIR cameras (Primicerio et al., 2012), and LiDAR (Lei et al., 2019; Liu et al., 2018; Zhou et al., 2020)

to monitor crop parameters with flight height ranging from over 100 m to under 6 m. Their low altitude stability allows users to inspect crops at a much closer range (6 – 4 m from the ground) than traditional satellite and aircraft-based sensing systems, allowing greater control and cheaper operating cost (Anthony, 2017; Christiansen et al., 2017). Specific to plant canopy characterization, UAV-borne LiDAR can capture different viewing geometries allowing complete construction of the scene compared to terrestrial scanning systems (Bareth et al., 2016) and overcoming the effect of occlusions, which is a primary limitation of boom-based scanners. Although these UAV-based platforms extract varying phenotyping traits such as plant biomass, yield, height, leaf area index (LAI), chlorophyll, nitrogen content, and water stress, they have not been widely tested for the complex indoor environment such as a greenhouse. Roldán et al. (2015) used mini-UAV (A.R. 2.0, Parrot, France) carrying analog sensors to measure greenhouse environmental parameters. This study aimed to develop an airborne sensory system that can travel through the greenhouse, eliminating the need to use multiple environment sensors to reduce the setup costs for commercial greenhouses. Although the UAV followed a pre-defined line using visual odometry and stopped at the squares printed on the ground to collect data, the study did not evaluate the UAV's navigational accuracy. Moreover, the study did not evaluate the sensors intended for extracting plant architectures. As plant canopy size information is important for many greenhouse operations, and GPS signals are significantly attenuated in metal framed structures such as greenhouses, it is of interest to investigate the parameters affecting the accuracy of

8

plant measurement and to evaluate performance of a non-GPS based local navigation system with the UAV.

2.1.4 UAV selection criterion

The first selection criterion involves looking at the basic design of the UAV, which is either fixed-wing or rotary-wing type. Due to the vertical takeoff and landing (VTOL) capability of fixed-wing UAV, they have better controllability with higher payload capacity, hoverable, and easier to maneuver in smaller environments (González-Jorge et al., 2017). Haghighattalab et al. (2016) compared the performance of low-cost rotary-wing quadcopter UAV (IRIS+, 3DR, USA) mounted with a digital camera (S100, Canon Inc., Japan) to industrial-grade fixed-wing UAV (eBee Ag, senseFly, Switzerland) carrying a multispectral camera. The former system had better performance due to its ability to operate at relatively lower altitudes and lower flight speed. The payload capacity is a crucial parameter and depends on the study's purpose, which can vary from developing a remote sensing platform, spraying applications, UAV swarms for a coordinated job, logistics operation and so forth. Since the objective of this study is to develop a remote sensing platform, the selected UAV should be able to house and carry a scanning sensor, environmental sensors, an onboard computer, and geopositioning sensors.

The UAVs are further categorized based on size and weight. A rotary-wing UAV under 25 kg is classified as small and as a mini-UAV if they range from few grams to several kilograms (Radoglou-Grammatikis et al., 2020). The size and weight play a critical role in the current study, where the goal is to choose the smallest possible platform as it will

be more maneuverable in tight environments such as greenhouses. Additionally, higher

UAV weight would require more thrust from propellers to take off and hover, causing

increased air-turbulence, adversely affecting the UAV stability in a closed environment

than an open field, and causing arbitrary shape changes of the underlying plant. Based on

the rotor configuration, rotary-wing UAVs are classified into quadcopters, hexacopter,

and octocopter. Although increasing the propeller count improves the payload capacity

and thrust, it increases the downdraft and turbulence underneath the UAV. Based on

design parameters, a mini-quadrotor UAV fits the current requirement.

Higher flight time is always a desirable trait; however, rotary-wing UAVs exhibit lower

flight times than fixed-wing counterparts as they are more aerodynamic than rotary-wing

UAVs. The flight times can be improved using larger or multiple batteries (González-

Jorge et al., 2017). Additionally, the flight path pattern affects the battery consumption by

choosing a path with fewer turns reduces the braking and accelerating instances, thereby

increasing the overall flight time (Christiansen et al., 2017). Flight autonomy allows the

users to control UAV's movement by sending commands to electronic speed control

(ESC) to manipulate the propeller speeds instead of manual control from remote control

stick wherein precision control is subject to the pilot experience. If the geopositioning is

available, the entire flight can be pre-programmed by setting the waypoints (GPS

coordinates of fixed locations), and UAV can trace the path to these fixed points while

collecting the data. However, in this study, since GPS signals are unavailable or too weak

in an indoor environment, the standard waypoint methodology for automating UAV

control can not be used, and other approaches need to be investigated.

10

2.2 Indoor Positioning System

Most of the UAV-based studies have focused on open-field agriculture. In contrast, an indoor greenhouse environment can present several challenges such as unreliable GPS signals, static obstacles, limited air space, relatively lower flying altitude, and limited UAV payload capacity (Wang et al., 2013). The GPS signal suffers attenuation and multipath effect due to obstacles such as walls, ceiling, and other typical greenhouse structures. Moreover, the signal strength further reduces since no direct line of sight (LOS) between the satellite and the receiver is available. Consequently, the satellite signals become too weak to be decoded by the conventional GPS receiver (Nirjon et al., 2014). Therefore, it is necessary to investigate and review the available Indoor Positioning Systems (IPS) to test their qualification with the UAV platform and greenhouse environment limitations. Extensive research has been done in the field of accurate indoor positioning using off the shelf technologies such as Bluetooth (Cantón Paterna et al., 2017; Neburka et al., 2016), radio frequency identification (Januszkiewicz et al., 2016; Pierlot and Droogenbroeck, 2014), WiFi (Fang et al., 2015; Ignjatovic et al., 2013), ultrasonic(Ilkovicova, 2016; Nong et al., 2018), infrared (Hauschildt and Kirchhof, 2010; Januszkiewicz et al., 2016), and ultra-wideband (Mahfouz et al., 2008; Tiemann et al., 2015).

2.2.1 Bluetooth

A typical range of Bluetooth signal is 10-15 m, so to design a Bluetooth-based IPS, tags must be placed around the search area within this range and receiver on the mobile

11

platform. Faragher and Harle (2014) tested the positioning accuracy of Bluetooth Low Energy (BLE) beacons via fingerprinting (analyzing the radio signal strength pattern at any given location) methodology to track the smartphones attached to pedestrians walking along a corridor. The deployment of beacons was not uniform and based on the point of interest where users were expected to walk. The presence of obstacles reduces the signal strength, and fingerprinting accuracy deteriorates with time and surrounding changes. Although the positioning accuracy of BLE is in the range of few centimeters, the receiver must be within a meter of the transmitter and increasing this distance results in rapid increases in positional uncertainty. For instance, the uncertainty could reach 5 m at a distance of 10 m from the transmitter. Since the surrounding environment of a greenhouse can change on a regular basis and they are composed of wall-like structures, which can impede the signal strength

 Bluetooth technology's advantage is its low cost, low power consumption, and small size of tags. BLE technology consumes even less power, extending the battery exhaustion period by months. Despite these advantages, Bluetooth suffers from location latency up to 10-30 s (Chawathe, 2009). For each new location, the system enters the discovery phase, where the mobile device (mounted with receiver tag) tries to detect the transmitting tags. This considerable delay is unacceptable for real-time applications. Additionally, the location accuracy of 2-3 m, presence of obstructions, and constantly changing surrounding environment (growers tend to relocate plants and other objects) makes it challenging to locate the UAV in the complex greenhouse environment.

2.2.2 Radio frequency identification system (RFID)

RFID comprises at least one reader (with integrated antenna) mounted on the roving

device and multiple transmitter tags spread around the search area. The reader

continuously broadcasts radio signals that charge the nearby tags, and they send a

response to the reader allowing the receiver to pinpoint its location relative to the tags.

Since the radio signals can pass through obstructions, this system does not require direct

LOS. Nevertheless, its strength gets attenuated, whose magnitude depends on the

property of material, highest for steel, wood, and concrete (commonly found in a

greenhouse environment).

Saab and Nakad (2011) evaluated the positional accuracy of low-cost passive RFID tags

by placing eight tags parallel to the travel path to maintain a constant distance of 2 m

between the mobile platform and tags. Even though tests resulted in a 10 cm error

(acceptable for our scenario), the system is highly constrained, and a change in flight path

could affect the overall accuracy. Due to inherent drift in UAV and the user requirement,

the UAV trajectory may change in every iteration. As a result, it is not feasible to

maintain a constant distance between UAV carrying the receiver and tags. Additionally,

high tag density (1 tag per 1.2 m) is impractical for commercial greenhouses, which

would require a massive number of tags to cover the entire scan area effectively, and they

must be pre-programmed with accurate location information.

2.2.3 Wi-Fi LAN

It is the most widely used IPS because of WLAN's (Wide Local Area Network)

widespread availability in most indoor architecture. Yang and Shao (2015) evaluated the

performance of WiFi-based IPS using hybrid Time of Arrival (ToA)/Angle of Arrival (AoA) technique resulting in positioning accuracy of 2.2 m and 1 m at 20 MHz and 40 MHz bandwidth, respectively. Compared to BLE, it requires a lesser number of transmitter tags. In addition to its cost-effective architecture, it does not require LOS (since it uses radio signals similar to RFID). Although the accuracy is very coarse (20-40 m), it can be improved by increasing the number of wireless routers (accuracy depends on the number of routers in the search area). However, similar to RFID, the signals get attenuated by greenhouse architecture and have a high power consumption. Moreover, removal, addition, or relocation of Access Points (AP -router) affects the positioning accuracy and requires costly updates to databases (Hernández et al., 2017).

2.2.4 Ultrasonic system

Ultrasonic sound waves can also be used to determine the distance between the transmitter (tags spread across the area) and the receiver (mounted on the mobile platform) by transmitting both the ultrasonic and radio signals. Since the radio signal travels nearly at the speed of light, it is received instantly, telling the receiver which transmitter is currently transmitting. The ultrasonic signal (traveling with the speed of sound) received later calculates the relative distance between the transmitting tag and receiver. Medina et al. (2013) tested the accuracy of the ultrasonic sensor to measure the position of the receiver relative to the transmitters. Although the results show subcentimeter accuracy, the experiment was very constrained, and it did not evaluate the effects of a real-world system. The tests were conducted in an obstacle-free room (7 x 5m) with four transmitters mounted on the ceiling's corners and the receiver placed on a

tripod-supported bench parallel to the ceiling. The receiver was moved parallel to the x and y-axis in steps of 10 cm (recording eight such positions), and each position was calculated by averaging 300 measurements. Experimenting in such ideal conditions disagrees with the real-world scenario where the motion is unconstrained in 3 dimensions and requires real-time positioning information wherein position can change significantly over 300 samples. The advantage of this system is its low cost. However, a direct LOS must be maintained since it employs sound waves, and multipath reflectance can lead to incorrect range estimation. The system is also sensitive to temperature changes, causing the range estimation to deviate by 2 mm in response to a 1°C change in the temperature.

2.2.5 Infrared (IR)

IR is also a prevalent IPS technology wherein the mobile platform continuously transmits IR signals captured by an IR receiver placed at a precisely known location. Although it has a high accuracy of up to 1 cm, it needs direct LOS between the transmitter and receiver. Similar to ultrasonic waves, they get reflected from the indoor structures causing the multipath error. Additionally, the architecture is expensive and requires high maintenance costs. The IPS technologies mentioned above suffer from multipath error since the bandwidth of these signals is narrow. Consequently, they can fail to distinguish between the signal that reached directly and those received after reflecting from the obstructions.

2.2.6 Ultrawideband (UWB)

The wide frequency range of Ultrawideband (UWB) signals allows it to resolve multipath propagation errors. Tiemann et al. (2015) tested the UWB system accuracy to track the

15

UWB receiver node under two scenarios, first mounted on the arm moving along a circular trajectory and in the second case, mounted on a UAV (Firefly, Ascending Technologies, USA) hovering at a fixed location for 220 s. In both scenarios, the receiver node was tracked by eight transmitting nodes spread along a rectangular boundary (7.2 m x 4.8 m). The resulting positioning error in tracking circular trajectory was 10 and 20 cm, respectively, along the horizontal plane and 3D space. In the second case, UAV held its position in a radius of 50 cm.

Further tests were conducted to test the repeatability of UAV (Bebop, Parrot, France) carrying UWB node to follow a pre-defined eight-shaped trajectory, and optical tracking provided the ground truth data (Tiemann and Wietfeld, 2017). This resulted in a positional error of 12.3 cm, 11.8 cm, and 28.8 cm along the x, y, and z-axis, respectively. Although UWB provides sub-centimeter positioning accuracy, the accuracy is greatly affected by the arrangement of transmitting tags (anchor constellation) which are evaluated by calculating Dilution of Precision (DOP), and a lower DOP is desirable. Both the studies involving Even though one constellation may result in low DOP for one flight pattern, changing the flight pattern (flight altitude, overlapping, and overall coverage) can result in a different DOP resulting in varying positional accuracy. Additionally, each node has its clock drift, which requires accurate clock synchronization for precise positioning.

The greatest challenge with the technologies mentioned above (including UWB) is their tag-based architecture, which requires multiple receivers to be mounted at precisely known locations of the scan area, which tracks the transmitter on the roving platform. As

a result, increasing the operation area requires new tags, which increases the setup cost and computational complexity. Additionally, varying tag constellation can result in varying positioning accuracies, thereby making it site-specific, which means that a tag setup in one environment may not produce similar accuracy if the environment is changed or the flight path is changed.

2.2.7 Visual odometry

The review of multiple IPS technologies by Mainetti et al. (2014) suggests that vision-based systems have the highest accuracy (except UWB) among the available technologies. However, their cost and complexity levels are relatively higher, but with improving computational capabilities, the processing algorithms are becoming very efficient. The most common types of vision-based systems have either a fixed camera system (Al Habsi et al., 2016; Liu and Paquin, 2018) or a mobile camera system (Iversen, 2018; Lee et al., 2011; Li et al., 2019; Mustafah et al., 2012). In the former case, cameras are present at fixed locations, and they track the mobile device in the 3D environment. While in the latter case, the mobile platform carries the camera and tracks the environmental features to estimate the motion and orientation. The positioning is performed either by comparing the extracted feature with stored features (with precise location information) (Xiao et al., 2018; Xu et al., 2019) or by calculating translation and rotation of the same feature in subsequent images (Dong et al., 2019; Lee et al., 2011; Zhou et al., 2014). Feature matching returns estimated translation and rotation between two adjacent views, and this transformation matrix can be used to locate the mobile platform.

The mobile camera system has an advantage over the fixed camera system since it does not require any pre-setup of the unknown environment, like mounting the multiple cameras at fixed locations. The fixed camera system has a restricted area of operation, which is limited by the field of view of the mounted cameras. Moreover, motion capture systems have high complexity and high setup cost (Tiemann et al., 2015). Although the area of operation does not restrict the mobile camera system, the environment should have detectable features that can be tracked in subsequent images. For the mobile camera system, matching features with the stored feature is restrictive in terms of storage capacity. As the area of operation increases, it needs to store more distinctive features in the database. Consequently, the system requires a greater amount of time to iterate through the image database that can impact real-time operation.

Stereo imaging can overcome this drawback, where features are detected in the first image (from left/right camera) and are tracked in the second image (from right/left camera). The disparity between the two images gives the coordinate data of the features. Thus, removing the need for storing the coordinates of features in a database (Iversen, 2018; Li et al., 2019). Kise and Zhang (2008) tested the tractor's automated steering accuracy by calculating its position relative to the crop row using a tilted stereo-camera (STH-MD1, VidereDesign, USA) mounted at the height of 2.2 m. This resulted in a maximum error under 0.30 m/s and RMSE of 0.11 m/s while traveling in a speed range of 0.70 to 1.10 m/s. Owing to the advantages of sub-centimeter accuracy, real-time operation, no pre-setup requirement, and unlimited range of operation (within certain altitude) makes it the most viable solution for UAV tracking (Achtelik et al., 2009; Lee et

al., 2011; Madison et al., 2007; Mustafah et al., 2012; Wu et al., 2016). Table 1 and Table 2 (tables were split to accommodate in a single page) presents a summary of existing IPS technology, which suggests that mobile vision technology fits the airborne platform requirements navigating in a non-GPS environment.

2.2.8 Comparison of technologies

Table 1. Overview of existing IPS technology using Bluetooth, RFID, Wi-Fi, and Ultrasonic systems.

Technology	Range (m)	Accuracy (cm)	Advantages	Limitations	Previous works
Bluetooth	10-15	200-300	Low Cost Low power consumption Small-sized tags	High location latency Poor accuracy	(Cantón Paterna et al., 2017; Chawathe, 2009; Faragher and Harle, 2014; Neburka et al., 2016)
RFID	1-10	10	LOS not needed High accuracy	High tag density Pre-programming tags with precise location information	(Kim et al., 2013; Ni et al., 2003; Saab and Nakad, 2011)
WiFi	20-50	10	Lower tag density Cost-effective LOS not needed	High power consumption Signal attenuated by obstructions	(Fang et al., 2015; Meng et al., 2012; Wang et al., 2013; Yang and Shao, 2015)
Ultrasonic	2-10	1-10	Low Cost High accuracy	LOS needed Multipath error Temperature-sensitive	(Itagaki et al., 2012; Kim and Kim, 2013; Nong et al., 2018)

Table 2. Overview of existing IPS technology using Infrared, UWB, and Mobile vision systems.

Technology	Range (m)	Accuracy (cm)	Advantages	Limitations	Previous works
Infrared	1-5	1	High accuracy	LOS needed Multipath error Expensive and high maintenance cost	(Hauschildt and Kirchhof, 2010; Januszkiewicz et al., 2016; Pierlot and Droogenbroeck, 2014)
UWB	1-10	0.1	Very high accuracy	Tag synchronization Temperature effects	(Dabove et al., 2018; Gigl et al., 2007; Yang et al., 2017)
Mobile Vision	NA	1	High accuracy No range restriction No initial setup	Feature-rich environment Good lighting conditions	(Dong et al., 2019; Lee et al., 2011; Mustafah et al., 2012; Xu et al., 2019)

2.3 UAV Flight Control

2.3.1 Path planning

Developing the flight plan is essential for an airborne platform, which can vary depending on the user objectives, such as choosing the shortest path, reducing the maximum number of turn, avoiding obstacles, overlapping percentage, and so forth (Bortoff, 2000; Koch et al., 2019; Mangiameli et al., 2013; Szczerba et al., 2000). The objective of the current study is to overcome the limitation of boom-based scanning, resulting in reduced measurement accuracy of crops placed further away from LiDAR's center due to its limited operating range and improving data quality by merging data collected from multiple perspectives that provide more information about occluded

regions and increase point density. With the sensor mounted on the airborne platform, it

is possible to divide the entire width into smaller segments of overlapping sets and fly the

UAV along these pre-planned paths. Christiansen et al. (2017) found that flight path

patterns can directly affect the accuracy of extracted point clouds and battery

consumption. The mini quadcopter UAV (Matrice 100, DJI, China) was flown along two

paths – the crop border and crop rows. Although the scanning along row resulted in much

higher point cloud density, more heterogeneity, and better volume estimates, it consumed

a higher battery and covered only a third area than the crop border scan. Since scanning

along crop rows allowed greater permeation of LiDAR, it resulted in a higher number of

points per unit area. However, the path had a higher number of turns, causing the UAV to

decelerate, reorient and accelerate at each turn, consuming extra power for covering the

same area. Sofonia et al. (2019) had similar findings regarding the influence of flight

pattern and range on the spatial resolution of the point cloud. Consequently, the amount

of time spent scanning the given area was proportional to density, whereas the distance to

target and speed was inversely proportional to density. To achieve these objectives, it is

necessary to pre-define UAV trajectory and path parameters such as distance, speed,

orientation, altitude, and the number of individual scans needed. Additionally, the flight

plan must also include the scan area's dimensions, which will define the length and

number of flight paths needed to scan the area completely for high-quality data.

2.3.2 Autonomous flight

To accurately follow the pre-planned flight plan, it is necessary to automate the flight

control. The primary need for autonomous flight is to reduce the human operator's

unintended inaccuracies and handle emergencies such as obstacle proximity, loss of

communication, sensor failure, and undesired trajectory (Nonami et al., 2010). Manual

piloting is more challenging than open areas; moreover, in the current study, since there

is no real-time video transmission of the scanning area, it can be a challenge to estimate

stopping/turning points (or waypoints). Additionally, it is challenging for a manual

operator to maintain constant velocity between waypoints, affecting the point cloud data

quality. Simultaneous Localization And Mapping (SLAM) algorithm has been widely

used for real-time navigation and control, which requires a horizontally mounted LiDAR,

and it localizes itself using the Laser Scan matching technique (Bachrach et al., 2009;

Diosi and Kleeman, 2005; G. et al., 2017; Li et al., 2014). However, in our current

system, LiDAR is mounted vertically downward to map the greenhouse floor crops.

Using additional horizontally mounted LiDAR is outside the scope of the current study.

Additionally, SLAM implementation is the computationally intensive and limited

processing power of mini-onboard computer can present a challenge for real-time

operation. Consequently, this research will evaluate using relative position information

from a vision-based sensor to locate and navigate the UAV in the indoor environment.

Furthermore, for controlling the real-time flight operations, it is necessary to develop a

User Interface (UI) to communicate with the UAV onboard system and send flight

commands from the ground station. This UI will also record, save, and transmit the flight

data, which will eventually be used to analyze the flight performance. Another objective

of the UI is to simplify the user-machine interaction and synchronize the sequence of

operations, making it user-friendly and comprehensive.

2.4 Data Quality Factors

Since the sensing platform is mounted on the UAV, its performance can be affected by the UAV platform itself (vibration and downdraft), flight parameters (travel speed, flight altitude), and sensing conditions (distance to target, off-nadir scanning, plant density). The following section discusses the influence of these factors on the output measurements and which conditions are suitable for improving data quality.

2.4.1 Platform vibration

Rotary wing UAVs control their movement by creating a difference in one propeller's rotational velocities with respect to another, which creates unsteady aerodynamic effects, ultimately leading to platform vibration (Verbeke et al., 2017). The primary vibration sources include high-speed rotation of propellers, the vibration of the center plate, extension arm, and payload. These vibrations can travel to the IMU sensors, affecting the accelerometer and gyroscope data, which could lead to flight instability (Li et al., 2015). It can also affect the quality of collected images and the performance of onboard optical positioning systems, which rely on the continuous registration of images resulting in erroneous positioning information (Dahlin Rodin et al., 2019). Radkowski and Szulim (2014) demonstrated that using four symmetrically-spaced blades or two propellers on a single motor can potentially eliminate the vibration. Anti-vibration mounts and dampers have been widely used to isolate the payload from the vibration sources (Changshuai et al., 2019; Tulldahl and Larsson, 2014; Wallace et al., 2012). Changshuai et al. (2019) subjected UAV carrying radar a Grms (root mean square acceleration) of 7.35g, 3.62g,

6.29g in x, y, z directions, respectively, in a frequency range of (4-2000 Hz). The study measured the acceleration response after mounting the payload on T-type dampers, which reduced to 1.73 g, 0.94g, 1.41 g in x, y, and z directions, respectively, which validated the ability of dampers to absorb the high-frequency vibrations originating from propellers. Li et al. (2017) investigated the performance of four dampers – silicone ball damper, silicone foam, Sorbothane sheet, and Kyosho zeal sheet in isolating the structural and motor vibration. The results showed that the Kyosho Zeal sheet reduced the vibration amplitudes by 97 % along the z-axis. Under extreme maneuvering, high flight speeds, and sudden accelerations, the magnitude of vibrations can become significant. However, in the current study, the UAV operation is limited to an indoor environment isolated from external wind and operating at very low speeds. Thus, the effect of vibration on the measurement accuracy of the sensor is neglected and can be part of future efforts.

2.4.2 Fly altitude

Since the range of LiDAR is limited, increasing flight altitude increases the distance to the target, thereby reducing the point cloud's spatial resolution (Sofonia et al., 2019). However, LiDAR mounted UAV must fly as low as possible to maintain its proximity with the crops. Airborne LiDAR system has been shown to improve height estimates at lower altitudes, reducing the RMSE from 14 to 6 cm as the altitude reduced from 1200 to 700 m, respectively (García-Quijano et al., 2008). Previous studies have shown the ability of mini-UAV mounted LiDAR to estimate the crop height while flying close to the ground with an increased spatial resolution of measurements. Anthony et al. (2014)

measured corn height with 0.75 m row spacing using a small range LiDAR mounted on a mini-hexacopter (Firefly, Ascending technologies, USA) flying close to 4 m above the ground resulting in less than 4 cm measurement error. Christiansen et al. (2017b) used a 2D LiDAR mounted on a quadrotor UAV (Matrice 100, DJI, China) to estimate winter wheat volume with a 0.12 m row spacing while flying at an altitude of 6 m above the ground. Although lower UAV altitude increases spatial resolution and point density, it also increases the downdraft from propellers, distorting the underlying plants (Christiansen et al., 2017). Additionally, lower flight altitude reduces LiDAR's field of view resulting in lesser coverage per flight. Consequently, it will require multiple flights with higher overlapping between adjacent flight paths to scan the same region. However, for indoor operation, the flight altitude is limited by overhead clearance of the area (greenhouse), and studies have not evaluated the impact on the measurement accuracy of UAV-borne LiDAR in such an environment. Nevertheless, Yan et al. (2018) evaluated the effect of varying LiDAR height (mounted on a constant speed track) on the width measurement of the artificial plants placed at proximity (within a detection height of 1 m). The study found that scanning below 0.75 m height significantly increased the measurement error along the width. This occurs due to the scanning pattern of the LiDAR, which throws light pulses along a circular arc. Consequently, the pulses are orthogonal at the center, but they become increasingly oblique as the target moves away from the LiDAR center. For the same plant setup (scene), decreased height limits the viewing range and makes scan lines more slanting, reducing their probability to reach the ground resulting in inaccurate measurements (Figure 1).
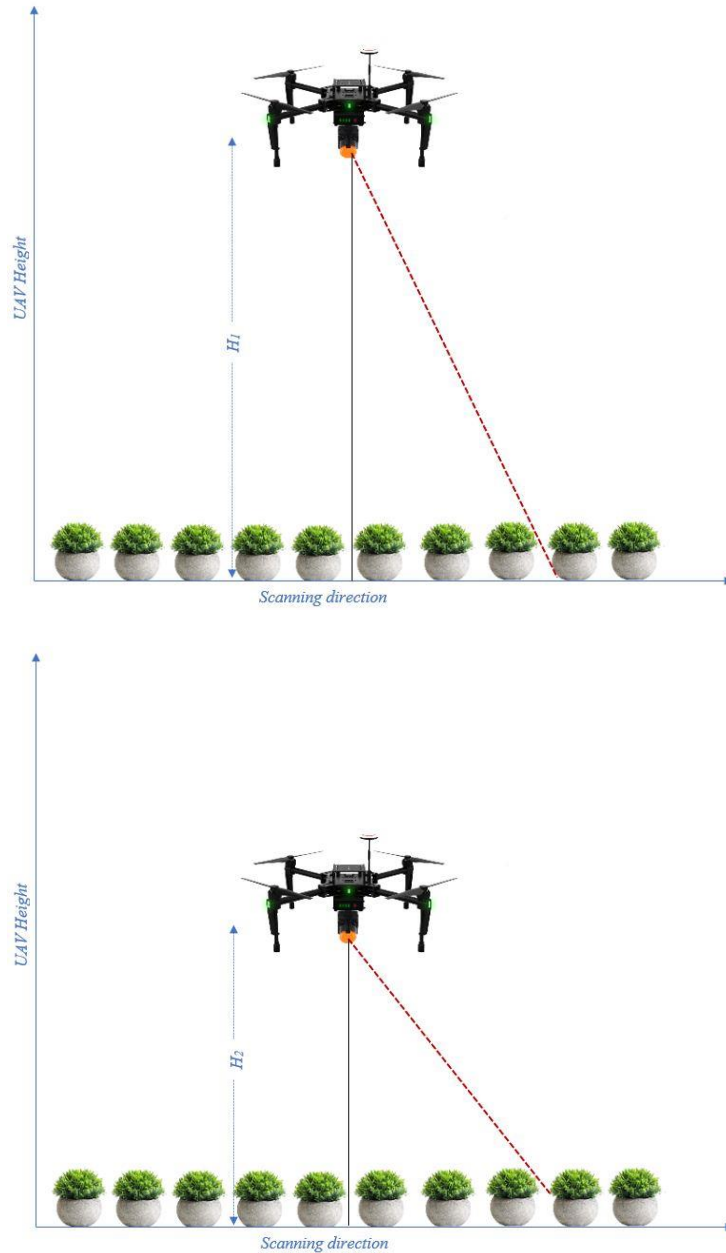
Figure 1. Decreasing LiDAR height reduces the field of view, and consequently, while scanning the same plant in both cases (a, b) for relatively lower height (H2 in (b)), the LiDAR is unable to reach the ground in case (b).

2.4.3 Travel speed

LiDAR sensors have limited and relatively low operating frequency; thus, varying travel

speed has a measurable effect on the point cloud resolution (Addis et al., 2018; French et

al., 2016; Walter et al., 2019; Zhang and Grift, 2012). Zhang and Grift (2012) tested the accuracy of a tractor-mounted 2D laser range sensor in measuring crop height at varying travel speeds resulting in increased error from 3.7% to 6.5 % as the travel speed increased from 0.20 to 0.41 m/s. Thus the travel speed is often in proportion to LiDAR's specified scan rate. Addis et al. (2018) used a UTM-30LX (Hokuyo Automatic USA) laser sensor mounted on a sliding rail at the height of 1.65 m, looking vertically downward for measuring the width and height of artificial trees under varying travel speeds. The increasing travel speed (0.3 to 0.9 m/s) increased the RMSE of width measurement (11 to 160 mm) but did not significantly affect the height measurement. The study also found that under low travel speeds, the RMSE in the width and height measurements did not vary with increasing horizontal distance (1.8 m -2.2 m). However, at a higher travel speed (0.9 m/s), RMSE in the measurement of both parameters increased significantly with the detection distance (horizontal distance). Consequently, maintaining low travel speeds is desirable for higher point density and thereby better measurement estimation.

2.4.4 Downdraft effect

Downdraft or downwash creates a turbulent downward airstream due to the movement of rotor blades, which can cause the underlying plants to deform or deflect, resulting in shape changes compared to the rest state (under no downdraft condition). Consequently, extracting the deformed plant shape can result in an incorrect estimation of their dimensions. Thus, it is necessary to identify the effect of the downdraft on the canopy structure and mitigate it. Previous studies have conducted three-dimensional computational fluid dynamics (CFD) simulations to analyze the distribution of flow fields

around a multirotor UAV (Ni et al., 2017; Roldán et al., 2015; Wen et al., 2019; Wu et al., 2019; Yang et al., 2017; Yao et al., 2019; Zhang et al., 2016; Zheng et al., 2018). The flow fields distributions along the vertical plane suggested that the downdraft effect is maximum beneath the rotors and significantly lower underneath the UAV abdomen. The distribution of flow fields along the horizontal plane is symmetrical around the UAV's center. The magnitude of air turbulence along the horizontal and vertical plane reduces as the distance between target and UAV center increases. Consequently, increasing distance to the target (either vertical distance, i.e., UAV altitude or horizontal distance) can minimize the impact of downdraft. However, the increasing distance from the target will deteriorate the measurement accuracy of ranging sensors due to their limited operating range.

To reduce the impact of downdraft on plant measurements, it is necessary to determine the region of influence of downdraft thereby, identifying the methodologies to avoid this region. Ni et al. (2017) investigated the magnitude and region of the air velocity under a quadrotor UAV (Phantom, DJI, China) while hovering 1.3 m from the ground. The maximum air velocity underneath the UAV dropped from 1.2 to 0.87 m/s as the vertical distance from the UAV increased from 0.4 to 1.2 m indicating that air velocity reduced with increasing vertical distance from the UAV. Additionally, the area of influence gradually spread with the increased vertical distance, specifically at 1.2 m, where the radius of the flow field was 0.60 m. Similar results were found for a hexacopter (SLK-5, Xian Wideworldz Aviation Science and Technology Limited Corp, China) hovering at 3.5 m, wherein the high-speed regions were concentrated around propellers reaching a

maximum value of 10 m/s underneath the propellers (Yang et al., 2017). As the vertical

distance increased to 3.4 m, the magnitude of air velocity reduced significantly to less

than 5 m/s, and the distribution became uniform with a maximum radius of 1.2 m. Wu et

al. (2019) measured the wind velocity underneath a hexacopter hovering at 2.6 m at three

different ground heights 1.0, 0.75, and 0.4 m. The velocity range reduced with increasing

distance from UAV recorded as 2.5-5.0 m/s, 2.0-3.0 m/s and 1.8-2.5 m/s.

As evident from the findings, the plants falling within the downdraft region would

experience structural deformity resulting in incorrect estimation of dimension. However,

the downdraft is concentrated to a fixed region whose magnitude reduces considerably

with increasing vertical or horizontal distance from the UAV center. Consequently, the

simplest solution is to scan the canopy at the maximum possible altitude; however, the

maximum flight height is limited due to the greenhouse's structural limitations and sensor

range. Another solution is to mount the sensor outside the region of the downdraft. Ni et

al. (2017) mounted two multispectral crop growth sensors at the ends of a 1.5 m carbon

fiber rod passing through the UAV center, thereby pushing the sensors outside the

downdraft region. The NDVI (Normalized difference vegetation index) and RVI (Ratio

Vegetation Index) values obtained from the UAV borne platform were linearly related to

a commercial spectrometer output with R^2 values of 0.82 and 0.77, respectively.

However, such a design is susceptible to vibration, and the sensors mounted at the ends

of the rod will experience significant vibration, which can deteriorate the data quality.

Yao et al. (2019) improved the existing design by using a damping rod to absorb the

vibration. The crop growth sensors were mounted at three different horizontal distances

from UAV's center – 0 m, 0.3 m, and 0.6 m. For the first distance, the sensor field of view was entirely inside the unstable region, and in the second distance, they covered both the stable and unstable regions. Whereas in the last case, they were entirely inside the stable region. The R^2 of RVI value was considerably higher (0.81) for the last case than the first two cases (0.63 and 0.66, respectively) compared to the handheld spectrometer.

2.4.5 Off-nadir scanning

Although these results demonstrate improved measurements as the sensors move outside the downdraft region, such design will affect the UAV maneuverability and stability and limit the navigational space. An alternative to mounting the sensor outside the downdraft region is to move the scanning plane of the LiDAR. Instead of mounting it vertically downward, which will scan crops directly beneath the rotors, mounting it at an angle (off-nadir) such that the scanning plane hits the crops outside the unstable region can reduce the downdraft effect on measurement accuracy. Although off-nadir scanning can focus on the targets outside the unstable region, it introduces certain limitations that can affect the point cloud quality.

Increasing the off-nadir scan angle increases LiDAR footprint diameter, consequently decreasing height estimation precision (Pang et al., 2011). Typically, the LiDAR footprint is circular at the nadir, becoming more elliptical as it moves away from the zenith, and at 30º, the area of the footprint is 54% greater than that at the nadir point (Sheng, 2008). As the footprint increases, the returning wave's intensity decreases, reducing the LiDAR's measurement accuracy.

The viewable gap fraction (VGF), or fraction of land visible from above, is greatly influenced by the sensors' viewing angle, which is largest at nadir and decreases as it moves to off-nadir (Liu et al., 2008). Compared to nadir, the VGF was less than half when scanning at 30˚ off-nadir angle. A similar effect can be experienced by the greenhouse crops placed on the ground, wherein a plant can obstruct the laser pulses to hit the bottom portion of the plant present in the next row. This effect is not significant during an overhead scan since it can extract the top view of the canopy allowing it to distinguish adjacent plant rows. However, scanning densely packed plant rows at an oblique angle increases the probability of obstructing laser pulses from reaching the next crop row with increasing mounting angles and row densities.

Figure 2 illustrates the effect of varying LiDAR mounting angles (θ) and UAV altitude (h) on the location of the scanning plane (L) (relative to the UAV center), affecting its ability to hit the ground and distinguish adjacent rows (shown by three plants). Equation (1) describes the mathematical relation between three parameters. In both cases (Figure 2 (a), (b)), the UAV altitude is equal (2 m) but with a varying LiDAR mounting angle of 20˚ and 35˚, respectively. For an off-nadir angle of 20˚, the scanning plane moved 0.72 m ahead of the UAV center, requiring a minimum row spacing of 0.09 m to avoid obstruction from the previous plant row. Although increasing the mounting angle to 35˚ (at the same UAV altitude) moves the scanning plane further away to 1.4 m from the UAV center, the same plant's minimum row spacing requirement doubled to 0.18 m. Additionally, with increasing angle, distance to same target increases ($r_2 > r_1$), and beam spot area increases resulting in reduced accuracy. Consequently, the choice of mounting

angle is a tradeoff between the impact of propeller movement and the limited operational

range of LiDAR. The impact of varying UAV altitudes at the same LiDAR mounting

angle is depicted in Figure 2 (b) and Figure 2 (c), which shows that increasing the UAV

altitude at a given mounting angle (35˚) pushes the scanning plane further away from the

UAV center; however it does not affect the spacing between adjacent plant rows.

$$L = h \times \tan \theta \qquad (1)$$

Where, $'L'$ is the distance of scanning plane ahead of UAV's center

$'h'$ is the UAV altitude

$'\theta'$ is the LiDAR mounting angle with respect to nadir
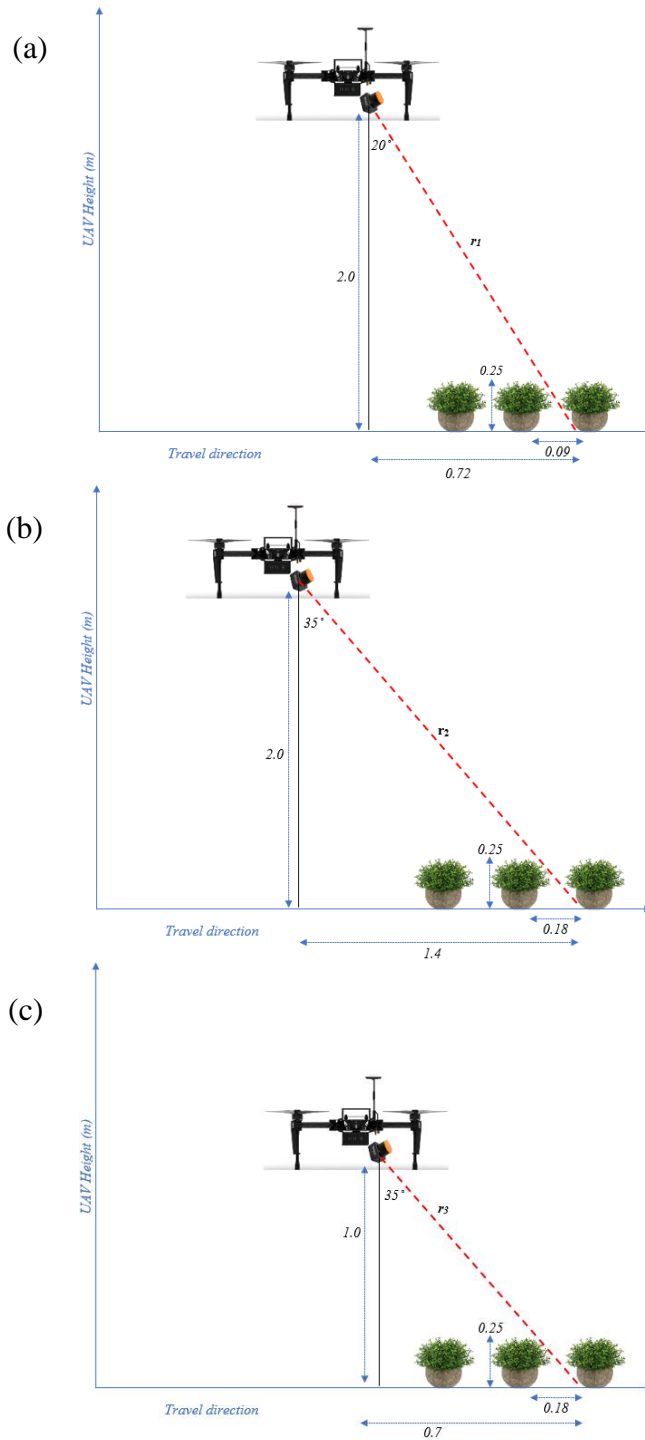
Figure 2. (a), (b) Impact of varying LiDAR mounting angle for UAV scanning same plant (0.25 m high) at an altitude of 2.0 m from the ground. Case (a) and (b) with a mounting angle of 20˚ and 35˚ scan ahead by 0.72 m and 1.4 m and require a row spacing of 0.09 m and 0.18 m. (b), (c) Impact of varying UAV altitudes at the same mounting angle (35˚). Case (b) and (c) with UAV altitudes of 2.0 m and 1.0 m move the scanning plane ahead by 1.4 m and 0.7 m, respectively. However, the row spacing requirement is the same for both cases.

2.5 Sensing Platform Design

2.5.1 Greenhouse climate sensing

Although the climatic conditions in a greenhouse are controlled, they are more rigorous

than open farms, and the sensors must meet those specifications. Specifically,

greenhouses have relatively higher operating temperatures (up to 38ºC) and higher

relative humidity than outdoor environments (Sammons et al., 2005). Thus, the selected

sensor should have a relatively higher tolerance in ambient temperature and humidity

ranges.

 Owing to the structural limitation of greenhouses, they have limited overhead space

compared to open farms, and as a result, the sensing range is limited to few meters.

Consequently, a sensor with a relatively smaller operational range (in few meters) is more

suitable. However, the plants are more densely packed than those in an open farm,

requiring a high precision sensor. Even though the greenhouse environment is insulated

from natural climatic conditions such as rain or duststorm, they often operate a spraying

system to water the crops or apply pesticides and have some dust particles. These

conditions may hinder or affect sensors' accuracy; consequently, they should have some

protective enclosure to prevent hazardous materials from entering the sensor's internal

parts. Therefore, it is necessary to choose a sensor with a suitable IP (Ingress Protection)

rating to protect the sensor. Although cost is not a primary limiting factor, selecting a

lower-cost sensor improves the system's economic feasibility for its use in commercial

greenhouses.

2.5.2 Plant sensing

The primary objective of this study is to generate high-quality 3D point cloud data of the

greenhouse crops, which will serve as input data for intelligent sprayers for analyzing

plant health and plant growth. Multiple sensors and previous work focus on collecting

plant structural information; the following section discusses the most relevant sensing

mechanism for extracting plant structural properties.

2.5.2.1 Camera-based system

The camera imaging technique is a prevalent methodology in extracting structural

information using various methods such as structure from motion, depth imaging, IR

(Infrared) imaging, airborne imaging, thermal imaging, and satellite imaging.

The optical flow technique requires translating a single photometric camera along a crop

row to obtain overlapping image sequences of the scene, and comparing the non-invariant

features in the successive images generates the point cloud data (Jay et al., 2015). Since

in a greenhouse, multiple plants of similar structures are tightly stacked in a single row,

features in the current image can pair with multiple features (instead of one distinct

feature) in the previous image leading to incorrect point cloud comparison. Developing

point cloud data from 2D image data is a tedious process that requires determining SIFT

(Scale-Invariant Feature Transform) between adjacent images (Lowe, 1999), followed by

bindle adjustment (Triggs et al., 2000) to refine the visual reconstruction and dense

reconstruction by matching non-feature points. Differently, LiDAR scan sensors only

require simple assembling of the individual scan lines.

Additionally, developing high-density point cloud data from the image requires low altitude (1-1.2 m) extraction to maintain acceptable resolution for image matching (Jay et al., 2015). The study acquired plant images at the height of 1 m using a single lens camera (Canon 500D, 1176 x 784 pixel resolution) to estimate plant height (savoy cabbage, sunflower, cauliflower, and brussels sprout), resulting in an overall RMSE of 1.1 cm. However, at such low altitudes, UAV's downdrafts can cause significant shape distortion of the underlying plants, reducing the accuracy of image matching.

Jin et al. (2017) analyzed the sowing density of winter wheat using a single camera (Sony ILCE 5100L, 6024 x 4024-pixel resolution) mounted on a hexacopter at three varying altitudes (3 m, 5 m, and 7 m) with an average row spacing of 16.4 cm. The increased UAV altitude from 3 m to 5 m resulted in an increased RMSE error of 27.3, 52.4, and 77.8 plants/m^2. The density estimation performance was influenced by the spatial resolution of extracted images, which requires low altitude flight for higher image resolution. Furthermore, the study did not evaluate the impact of UAV's downdraft measurement accuracy of the plant dimension, which can cause significant shape distortion in the underlying plants affecting that increases with decreasing altitude. Jay et al. (2015) concluded that external wind poses a major obstacle in rendering plant structure through a single camera as the plant position can change in subsequent images. Single camera-based extraction requires a high overlapping percentage (around 80%) between adjacent flight paths (Jin et al., 2017; Moeckel et al., 2018), thereby reducing the coverage area per flight. In addition to side overlap, the images also require a high frontal

overlap. Jay et al. (2015) acquired crop images at every 4 cm using a manually moved ground vehicle at an altitude of 1.2 m. For a commercial greenhouse, extracting images at this frequency will consume a considerable portion of the onboard computer's limited memory space, and for overlapping scans, the memory requirement will multiply. Another source for plant data extraction is the 3D Time of Flight (TOF) cameras, which measure the phase shift of the reflected light with respect to incident light for each pixel, with a wavelength of 850 nm (Hemming et al., 2014; Klose et al., 2011). Klose et al. (2011) compared the performance of high-resolution (200 x 200) CamCube 3.0 (PMDTechnologies) and lower-resolution IFM Efector 3D (50 x 64) in measuring plant height. The study found that measuring the height of standard boxes at 1 m/s resulted in an error of 30 cm and 5 cm with CamCube and IFM, respectively. This error can be attributed to motion blur. Additionally, the study measured distance to a whiteboard under varying illuminations and found that TOF imaging is sensitive to variation in light intensity; consequently, increased light intensity (from 3000 lux -halogen to 50000 lux - direct sunlight) resulted in an increasing error in the measured distance of 4 cm. Specifically for greenhouse crops, the system's measurement accuracy would vary as the intensity of supplemental lighting changes. Moreover, TOF cameras have a high weight range – 510 gm (SR-4000, Mesa Imaging AG) and 1438 gm (CamCube 3.0, PMDTechnologies), which can be a limiting factor for UAV platform, and they require a warmup time of up to 40 minutes to achieve measurement stability (Piatti and Rinaudo, 2012).

Stajnko et al. (2004) used thermal imaging to estimate the number and diameter of orchard apples. The accuracy in estimating fruit count varied with its growing stages, which increased as the fruit ripened. The accuracy in diameter measurement had a similar pattern resulting in lower accuracy during the vegetative period. The study could not distinguish the fruits from the leaves, which were growing deep into the canopy. Furthermore, the accuracy depends on the time of the day, which was conducted in the late afternoon when the temperature gradient between fruit and background is highest. The thermal camera weight was over 2.26 kg, which is not a feasible payload for a mini-UAV.

Despite the ease of use, they suffer from certain disadvantages. Typically, stereovision offers less accuracy than the laser-based system and requires appropriate calibration to generate acceptable results (Rosell and Sanz, 2012). The extraction process is complex and requires highly overlapping images, making it extremely resource-intensive and time-consuming to process larger scanned areas. The output resolution is influenced by the image quality, which can be affected by varying lighting conditions and downdraft effect from propellers, as discussed earlier

2.5.2.2 Ultrasonic sensor

Ultrasonic sensors emit 5 to 10 ultrasonic sound waves every second, and measure the time taken by the returning wave to calculate the distance to the target. This distance information can estimate the target's structure and has been widely used in multiple studies(Gil et al., 2007; Moltó et al., 2000; Tumbo et al., 2002; Zaman et al., 2005, 2006).

The studies used multiple ultrasonic sensors mounted on a vertical bar to extract plant height information, and such a design is impractical for a UAV platform. Additionally, operating multiple sensors at the same time can cause interference leading to faulty readings. (Tumbo et al., 2002) compared the accuracy of the laser scanner and ultrasonic sensor in measuring the canopy volume with manual measurement. The results showed that the laser scanner had higher accuracy in estimating the volume of partially or fully defoliated trees than ultrasonic sensors. This is because laser scanning sensors have much higher sensing speeds than ultrasonic sensors. As discussed before, using multiple sensors may lead to interference, and it also increases the computational load and maintenance cost. The major drawback of ultrasonic sensors is their large divergence angle, limiting the resolution and accuracy of measurements; additionally, multiple sensors are required to extract data of the region of interest (Rosell and Sanz, 2012).

2.5.2.3 LiDAR sensor

LiDAR releases light beams to targets and calculates the distance from analyzing the returning wave. The working principle is either based on the Time of Flight principle (time taken by the reflected wave to reach the laser sensor) or by calculating the phase shift of the returning wave compared to the incident light source (Rosell and Sanz, 2012). The three most common platforms used for LiDAR-based extraction are Airborne laser scanning (ALS), Terrestrial laser scanning (TLS), and Mobile laser scanning (MLS). ALS uses an aircraft to carry a LiDAR at high altitudes whose precise location and orientation are calculated from DGPS (Differential GPS) and IMU (Inertial Measurement

39

Unit), respectively. The range values obtained from the reflected objects generate a georeferenced point cloud. ALS has been used for landscape characterization (Anderson et al., 2016), classification of tree species (Lin and Hyyppä, 2016), and studies of the surface properties such as surface structure, slope, reflectivity, and roughness (Hug et al., 2004). In agriculture, it has been used for estimating the vegetation height and density from the height data (Lindberg et al., 2012). A significant limitation of ALS is its inability to characterize the below canopy biomass(Hilker et al., 2010).

TLS is a stationary scanning methodology wherein the scanner is mounted on a tripod. TLS is typically useful for surveying small areas and generating a detailed point cloud of the regions having a radius in tens of meters. TLS requires a clear LOS between the scanner and target, and occlusion occurs where laser beams are blocked before reaching the object of interest. Multiple scans from different perspective angles is an approach to reduce the occlusion challenge, and it requires numerous background targets to register multiple-view point cloud data (Moorthy et al., 2008). Keightley and Bawden (2010) used TLS based approach to estimate vine volume and compared it to analog volume (measured as the volume of water displaced by immersed vine). The measurement accuracy not only varied with the number of scans but also with the viewing angle. The RMSE in volume measurement doubled from 2.15 liters to 4.23 liters as the number of scans reduced from 10 to 2. To test the effect of varying viewing angle, two scans with three viewing angles were taken with opposing (180˚ to each other) views resulted in different measurement errors (3.67 and 2.61 liters in RMSEs). TLS methodology was also implemented in the greenhouse environment to develop 3D geometry of tomato

crops by placing the tripod-mounted LiDAR in three different positions, along a circumference of 5.0 m radius circles with a spacing of 120º from each other (Hosoi et al., 2011). Each position took over 15 minutes to complete the scan, and the tests were conducted under windless conditions to make sure the canopies did not move in the successive scans.

From the review of past studies, the drawbacks of the TLS are evident despite their high accuracy. Firstly, as the scan area increases, the number of stationary scans required also increases. Secondly, it requires multiple references with precise coordinate information to stitch the separate scans into a single scan. Additionally, it requires manual effort to create the entire setup, which is time taking and prone to error. Typically for an indoor environment, each scan captures only a small section of the entire canopy, and it would be impractical (in terms of time consumption) to scan the entire greenhouse. Furthermore, terrestrial LiDAR (3D-LiDAR) costs are very high (19,000 $ (ILRIS 3D, Optech Inc., Canda), which reduces its commercial viability (Maddern et al., 2015). MLS is similar to ALS but with a relatively smaller mobile platform traveling either on the ground or in the air at very low altitudes. The system requires a real-time accurate positioning system (GPS for outdoor systems and Indoor positioning system (IPS) for indoor systems) and orientation from the IMU. A robotic vehicle (either grounded or airborne) carries the scanner, and the system is typically useful for scanning areas in close range. The range of scanning area is limited by LiDAR's operating range and platform's navigation range (large – UAV, medium –ground vehicle, small – irrigation boom, or guided tracks). Compared to other LiDAR-based mapping methodologies, the

41

UAV-based LiDAR system meets the requirement of scanning flexible and larger regions (Lin, 2015).

The MLS typically employs 2D LiDAR, which has the advantage of significantly lower weight, cost, and size than stationary (3D) LiDAR counterparts. As the name indicates, the 2D LiDAR scans only in two dimensions resulting in a line scan. The third dimension is added by moving the sensor perpendicular to its scanning plane, and continuous assembling of individual scan lines along the travel direction generates the point cloud (Sanz-Cortiella et al., 2011). Mobile mapping systems fill the void between terrestrial and airborne scanning, taking advantage of both systems (Barber et al., 2008).

Table 3. List of 2D LiDAR compatible with a mini-UAV platform

Specifications	Commercial LiDAR				
	URG 04 LX	UST 10 LX	RPLIDAR A3	TiM 561	Velodyne Puck Lite
Power (W)	2.5	3.6	2.25	3	8
Supply Voltage (V)	5	12-24	5	9-28	9-18
Scan Range (m)	5.6	10	25	0.05-10	100
Weight (gm)	160	130	190	250	590
Scan Rate (Hz)	10	40	10-20	15	5-20
Angular Resolution (degree)	0.3	0.25	0.34	0.33	0.1-0.4
Scan Angle (degree)	240˚	270˚	360˚	270˚	360˚
Communication	CN1 (USB mini)	Ethernet	TTL Serial Port	Ethernet	Ethernet
Dimension (mm)	50x70	50x70	72x41	60x60x86	89x72
Cost ($)	1080	1680	600	2100	4000

2.5.3 Climate sensors

Greenhouses require precise measurement of several environmental parameters to maintain adequate climatic conditions for ensuring plant health and productivity. Measurements of these parameters allow growers to automate several greenhouse-related activities such as environmental monitoring by recording air temperature and humidity to control heating systems, ventilation, and foggers (Pahuja et al., 2013; Pawlowski et al., 2009). Greenhouses are equipped with shading screens that control the incident solar radiation responsible for maintaining appropriate temperature and heat transfer operation (Pawlowski et al., 2009). Wireless Sensor Networks (WSN) have been widely used to measure environmental variables by deploying battery-powered sensors throughout the greenhouse (Akyildiz et al., 2001; Li et al., 2014; Matese et al., 2009). However, to operate each node, WSN requires an external battery, communication module, and controller whose operating cost can increase significantly with the area of operation (Ruiz-Larrea et al., 2016). Consequently, mobile robots can overcome this limitation by carrying the sensor set and collecting measurements of the region of interest. UGVs are useful for measuring ground properties such as soil temperature and humidity. On the other hand, UAVs have the ability to reach any point in three-dimensional space, making them suitable for collecting aerial measurements such as air temperature and humidity, solar radiation, CO_2 concentration, and Photosynthetic Active Radiation (PAR).

PAR constitutes a part of the radiation spectrum ranging from 400 nm to 700nm, which is utilized by crops to control photosynthetic activity. Most of the greenhouses employ supplementary lightings such as high-pressure sodium (HPS) lamps (Heuvelink and

Challa, 1989) and energy-efficient light-emitting diodes (LEDs) (Schwend et al., 2016) to maintain the daily light integral (DLI) requirement for continued photosynthesis. Barnard et al. (2014) developed an inexpensive PAR sensor (PARduino) using Licor PAR (LI-190 SA, LI-COR Inc., USA) sensor. The low output signal of the PAR sensor was amplified by Universal Transconductance Amplifier (EME Systems, USA), powered by a 6 V battery, and data was logged on using Arduino (Pro Mini, Arduino). The sensor can be used as an alternative to existing research-grade data loggers.

 Alternative to PARduino could be Quantum sensor from Apogee, which has similar standard deviations, and the cost could be 25% to 50% lesser when compared to PARduino but has a drawback of reduced spectral response near Infra-Red/Deep-Red region. Few variants of Apogee quantum sensors are self-powered, which could be helpful, considering the power consumption constraints of UAV.

Similar to PAR, solar irradiance reaching the greenhouse crops affect the photosynthetic rate (S. Hemming et al., 2006), accumulation of biomass (Hatfield, 2014), and transpiration rate (Medrano et al., 2005). Moreover, in a greenhouse environment, the different cover materials can diffuse the incoming radiation invariably, affecting the radiation use efficiency (Cabrera et al., 2009). Consequently, measuring solar irradiance is critical for greenhouse crop monitoring. Thus, three climatic sensors (PAR, solar irradiance, temperature, and humidity) were selected for this study. The choice of selection depended on sensor weight, dimension, and power consumption.

2.5.4 UAV constraints

UAV's flight time is primarily influenced by its payload and decreases significantly with increasing weight. Consequently, the selected sensor should have the lowest possible weight. As mentioned previously, due to indoor operation, a mini-UAV is suitable for the current study, whose payload is limited to a few kilograms (Vergouw et al., 2016). As a result, sensor weight becomes a crucial selection parameter. Like the payload, UAV's power supply is also limited, so choosing a low power-consuming sensor is essential for higher flight times, allowing it to scan a greater area in a single charge. Previous studies using LiDARs for plant structural reconstruction have shown reduced accuracy with increasing travel speed due to sparser (low-density) point cloud data. However, commercial UAVs are usually developed for their high-speed endurance, and unlike UGVs, traveling at low speed can be a challenge. Consequently, a higher frequency sensor is desirable to ensure accurate measurement with a high-speed platform. Chen et al.(2019) developed an energy consumption model for a drone. The findings suggested that energy consumption (referred to as State of Charge or SOC) depends primarily on travel distance, payload, speed, and initial SOC of battery. The study simulated performance of the battery (Ultimate PX-04 LIPO, 1000 mAH) under varying parameters as mentioned before. The SOC had an inverse relationship with horizontal speed, making the low-speed operation less optimal from an energy standpoint. The results of energy consumption at varying speeds (2 m/s -8 m/s) showed that under the same conditions of payload (0.4 kg) and travel distance (1000 m), the SOC reduced to 0% with 2 m/s speed compared to 60%, 70%, and 80% when flying at 4, 6 and 8 m/s, respectively.

46

2.6 Conclusions of Literature Reviewed

The analysis of available sensing platforms for greenhouse applications illustrates the limitation of navigating UGV and irrigation boom-mounted sensor to the region of interest and capturing multi-view data of crops. An aerial sensing platform is highly beneficial for greenhouse crop monitoring yet has several challenges. Absence or limited GPS signal availability inside a greenhouse requires a local positioning system to localize UAV position with centimeter grade accuracy. Existing tag-based architecture have a limited range of operation, needs pre-setup, require precise pre-positioning of transmitter tags, leads to costly database update with changing environment and varying tag architecture can lead to varied positional accuracy. However, an environment with good lighting conditions and feature-rich ground such as a greenhouse is most compatible (consistent) with stereovision odometry. Since for greenhouse application, UAV operating altitude is very low (within few meters above the ground), it ensures that stereo camera is able to track the greenhouse floor at all times resulting in centimeter grade positional accuracy. To overcome the drawback of occlusion in existing (UGV and boom-based) platforms and limited operating range of sensors, it is necessary to scan the crops from different perspectives and extract multi-view geometry. Consequently, precise path planning is needed to achieve this objective which can navigate the UAV through a set of overlapping parallel paths. Additionally, to address the UAV and sensor limitation, the plan must also include UAV altitude, speed, and scanning direction.

It can be challenging for a manual operator to accurately and precisely maintain (and repeat) the set parameters of the flight plan, thereby essentializing the autonomous navigation of the UAV. Moreover, manual flights can be susceptible to sudden variations in flight parameters (speed, altitude, and yaw orientation), impacting the point cloud quality. The propellers' movement creates a downward airflow field, which can affect the shape of the underlying plants, thereby affecting the measurement accuracy of plant dimensions. However, these effects reduce significantly as the target canopy moves away from the unstable (underneath the propeller) region. Consequently, scanning the plants outside the downdraft region can reduce the impact of downdraft on measurement errors, and instead of scanning vertically downwards, mounting the LiDAR at an off-nadir angle can move the scanning plane away from the unstable region. The limitations of matching distorted (under propeller downdraft) 2D plant images from a camera and the need for multiple ultrasonic sensors make the point cloud acquisition challenging for a low-altitude UAV platform. Consequently, a high-frequency, low-cost, and lightweight 2D LiDAR mounted on an aerial platform meets the requirement of extracting plant dimensions in an indoor environment.

Chapter 3. Materials and Methods

3.1 Aerial Sensing Platform

3.1.1 Hardware setup

The aerial platform (Model DJI Matrice 100, SZ DJI Technology Co., Ltd., China)

chosen for the test was a quadcopter with a 65 cm diagonal wheelbase and a maximum

payload of 1000 g (excluding battery). A TB48D (SZ DJI Technology Co., Ltd., China)

battery with a power output of 130 Watt-hr and weighing 676 g was used to power the

UAV, resulting in 16 minutes and 28 minutes of flight time at full payload and no

payload, respectively. However, the UAV model has the option of using two batteries at a

time, which can improve the flight time to 40 minutes with no payload; this study used a

single battery at a time. The propellers (length of 36 cm) were protected by guards to

prevent the UAV from getting damaged in case of a crash.

3.1.1.1 Positioning system

The vision-based sensor (Model DJI Guidance, SZ DJI Technology Co., Ltd., China)

used for positioning the UAV comprised five sensors, each with a stereo camera and

stereo ultrasonic sensor for visual odometry and obstacle sensing, respectively. The

system was chosen for its high positioning accuracy (up to 5 cm), wide operating range

(0.2 m to 20 m), acceptable weight (325 g, within the payload capacity), compatibility

with the UAV platform, and advantage over existing IPS technologies explained earlier.

The module was mounted beneath the UAV battery compartment.

3.1.1.2 Plant measurement sensor

The laser range sensor (Model UST-10LX, Hokuyo Automatic Co., Ltd., Japan) used for

extracting ground truth data has a 270˚ field of view and angular resolution of 0.25˚,

resulting in 1080 measurement points in a single sweep at a frequency of 40 Hz. It has an

operating range of 0.06 m to 10 m (maximum range of 30.0 m) with an accuracy of 40

mm. It has the advantage of lightweight (130 g) and small dimensions (50 x 50 x 70 mm),

allowing easy installation without obstructing the visual sensors. LiDAR was mounted on

the UAV to face vertically downward, allowing it to scan objects on the ground from the

top view. A set of three mounting kits were 3D printed for attaching the LiDAR at the

gimbal mounting location of the UAV. Each had different viewing angles with respect to

nadir – 0˚, 20˚, and 35˚ allowing the LiDAR to scan off-nadir. The off-nadir mounting

kits attempted to collect plant information without been affected by downdraft when the

UAV was directly above plants during flight.

3.1.1.3 Data collection and flight control

An external microcomputer (Model Odroid XU4, Hardkernel Co., Ltd., South Korea) was

used as the onboard processor to connect all the sensors and peripherals. It was

responsible for running specially designed algorithms written in C++ to control the UAV

autonomously and store sensor data. To maintain communication between the ground

computer and onboard computer (Odroid XU4) over LAN (Local Area Network), a USB

(Universal Serial Bus)-powered WiFi antenna (Model Odroid WiFi Module 5A,

Hardkernel Co., Ltd., South Korea) was also used. The communication involved

receiving flight commands and sending recorded sensor data to the ground computer.

A Dell Lattitude 5590 laptop computer was used as the ground station with the following

specifications – Intel® Core^{TM} i5-8565U CPU @ 1.70 GHz processor, 64-bit operating

system, and 8 GB RAM. It served as an interface and communication channel for the

onboard computer, allowing the user to control UAV operations remotely. It was used for

performing offline processing to generate point cloud data from the sensory information

received from the onboard computer. The ground station computer also generated a flight

plan (or pattern) based on user inputs and greenhouse dimensions, and these patterns

were eventually used to navigate the UAV through the indoor environment.

3.1.1.4 System assembly

The Guidance was mounted underneath the UAV such that the downward-facing sensor

could track the ground movement. The remaining four Guidance sensors were mounted

along the four directions, each looking forward, backward, left, and right of the UAV.

Since the study did not employ any camera, the LiDAR was installed on the gimbal

mounting position using 3D printed mounts. The downward-facing LiDAR provided scan

data of the objects placed on the ground, which served as a reference for testing

automated flights' repeatability. For simplicity, the onboard computer, Odroid, was

mounted on the top of the battery compartment allowing easy connectivity with other

peripherals.

Figure 3 shows the schematic used for interconnecting and powering the peripherals. A step-down converter (UBEC DC/DC Step-down (buck) converter, Adafruit, USA) was used to convert 22.2 V supply from UAV for powering Odroid at its operating voltage (5V). The UAV battery directly powered the other two sensors (LiDAR and Guidance). Although the UAV can communicate to the onboard computer using both USB and Universal Asynchronous Receiver Transmitter (UART) port, the USB port was chosen. However, with this communication architecture, all three USB ports of the onboard computer were occupied. Figure 4 shows the front view of the final unit. In the future, the UAV can be connected using the UART port, freeing one USB port to connect analog sensors via Arduino. Additionally, a RAM Steel Reinforced VESA plate with a ball (RAM Mounts, National Products Inc., USA) was attached at the top of the battery compartment to mount the UAV on a speed track.
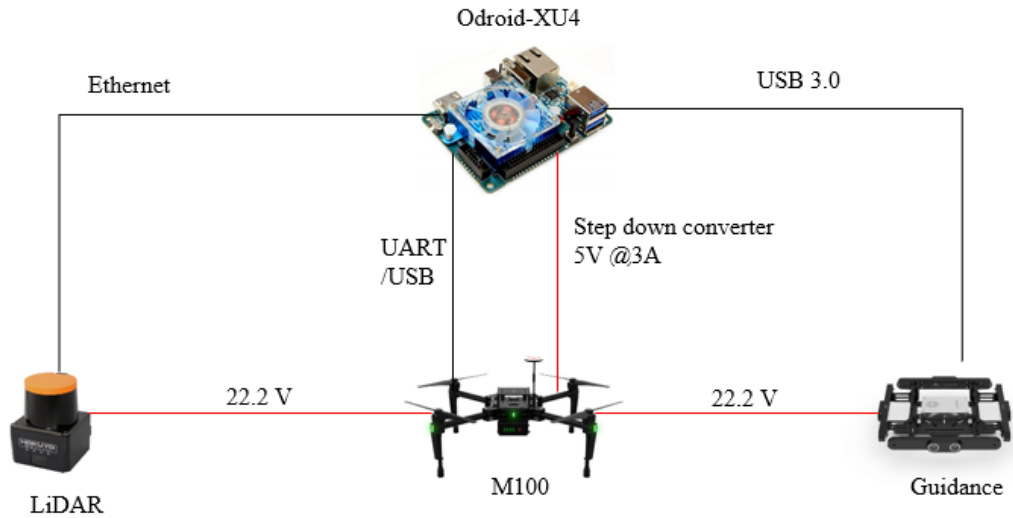
Figure 3. Schematic of components, power supply (red), and communication channel (black).
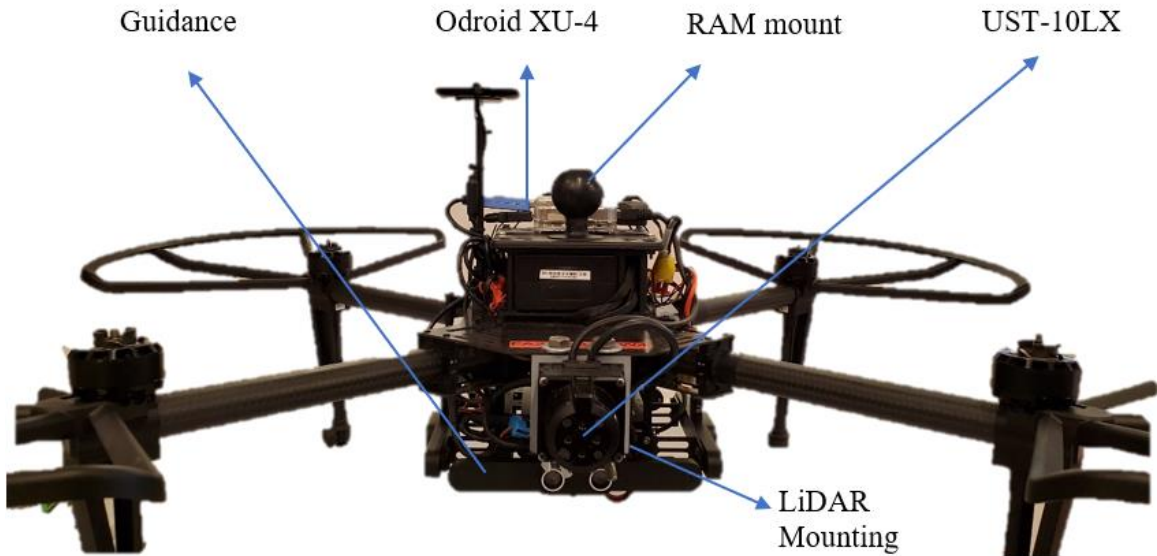
Figure 4. Front view of the aerial platform, showing the primary components.

3.1.2 Software setup

Since it was infeasible to manually access the onboard computer while the UAV is in flight, a Ground Control Station (GCS) was needed to maintain a communication link with the onboard computer using the available wireless local area network (WLAN). A MATLAB (version 9.8.0.1417392 (R2020a) Update 4) based program on GCS analyzed

the sensor data to generate a flight plan and greenhouse dimension data. MATLAB was also used as a statistical tool to analyze the flight data.

Qt Creator (Qt Co. Ltd., version 4.11.0) is an open-source tool used to develop a graphical user interface to allow users to interact with the UAV. Qt takes greenhouse dimension inputs from MATLAB and generates a flight plan or trajectory depending on the data quality requirement. Qt was also used to develop a flight control console, which sends the flight control instructions to the onboard computer. Additionally, it allows users to record the sensor data and send it back to the GCS.

Robot Operating System (ROS, version Melodic Morenia) running on Ubuntu 18.04 was used to integrate, record, and store the sensor data. ROS is a widely-used open source robotic control software that provides a wide array of built-in libraries, tools, and functions for interconnecting sensors to achieve the desired task or objective. Individual process or sensor data are treated as nodes (ROS nodes), and they communicate using ROS topics. The primary purpose of the ROS topic is to either publish data (send sensor data) or subscribe data (receive sensor data). Any node can subscribe to any topic allowing multiple sensors to communicate with each other allowing the user (developer) to create an interconnected network of sensors. Using this architecture, a C++-based flight control program was written in ROS to process flight commands received from GCS and navigate the UAV correspondingly. The real-time processes were complied on Odroid, referred to as Onboard Control System (OCS/OC) in this study. The primary purpose of OCS was to – (1) communicate with all the onboard peripherals and collect sensor data, (2) control UAV position through attitude control (pitch, roll, and yaw

54

orientation), and (3) transfer (recorded sensor data) and receive (flight command) data from GCS.

3.1.3 Generating point cloud data map

3.1.3.1 Raw data synchronization

Based on user requirement, the aerial platform was manually flown (pitched) along the scanning area, and OCS recorded the following sensor data – (1) orientation and linear acceleration from IMU, (2) position and velocity from Guidance, and (3) range and intensity data from LiDAR. Post data collection, the flight data (recorded sensor data) was sent to GCS, which was processed by a custom program written in MATLAB to generate the 3-D map of the scanned area (Figure 5). Since each sensor data was recorded with a global timestamp and had a fixed frequency, they were combined using the nearest timestamp.

3.1.3.2 Flight data selection

Post synchronization, the flight path was filtered to remove the take-off and landing sections which were followed by the identification of pitched (forward motion) and rolled (lateral motion). Since the useful scan data was available only along the pitched portions, the final dataset was comprised of successive pitched portions. Furthermore, non-constant portions of the flight path caused instability in the scanning plane. In autonomous flight, the initial acceleration region and the deceleration region at the end of flight caused this error, so the algorithm identified and filtered these regions from the flight path data before processing them.

3.1.3.3 Geometrical distortion correction

Since a 2-D LiDAR was used in this study, it was necessary to translate the 2-D coordinates along the traveling direction to generate 3-D data. For simplicity, the x and y-axis were chosen as UAV's traveling and LiDAR's scanning direction, respectively. Unlike GPS coordinates, Guidance's positional coordinates were relative, which could change the axis of travel from one flight to the other, so it was necessary to identify the major axis of travel (either x or y) and transform it along the x-axis. The following steps were followed – (1) identify the major axis of UAV travel direction, (2) calculate its angle from the x-axis, and (3) rotate the flight path about the z-axis by equal and opposite magnitude.

3.1.3.4 Identification and removal of flight instability

The point cloud data quality was affected by the instability of the UAV platform. Three sources of error were identified and corrected, created by UAV drift along scanning axis, variation in altitude, and UAV heading variation. The drift correction was obtained by translating each point along the y-axis and altitude correction using Guidance-derived altitude as a reference and translating each point along the z-axis. The heading error was corrected by calculating the yaw error from the average yaw heading (entire flight path) from IMU at each UAV location and rotating each line by this error value. The same algorithm was used for generating point cloud data for both manual and autonomous flights. The entire process was repeated for each pitched portion.
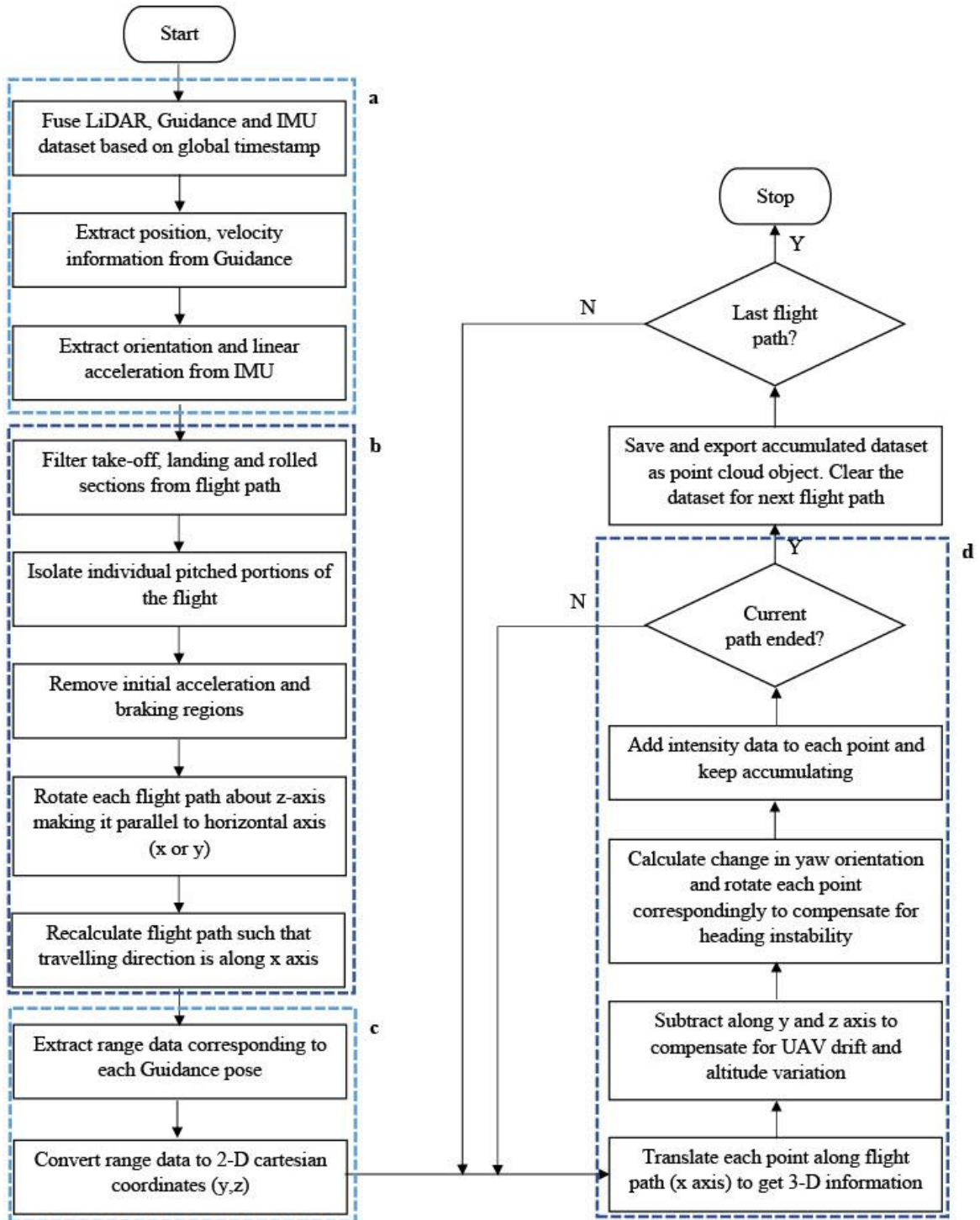
Figure 5. Flowchart of offline processing program written in MATLAB. (a) Read and synchronize multiple sensor data, (b) extract and align pitched flight portion, (c) get range data, (d) generate 3-D data and remove flight instability.

57

3.2 Autonomous Navigation

3.2.1 User-defined flight area

Since the UAV is navigating in a GPS denied environment, it must know the scan area's aerial parameters – length, width, height, and orientation. Figure 5 illustrates the flowchart of the offline processing of the manual flight data by the MATLAB-based algorithm to extract greenhouse information and get user requirements. Table 4 illustrates the parameters used for generating flight paths. The first four parameters are calculated by manually flying the UAV, wherein Guidance provided the dimension data, and the UAV heading was derived from IMU. The UAV was flown such that it pitched and rolled along the scan area's length and width, respectively. During the entire manual flight, the heading of the UAV was not changed and was oriented along the length. Consequently, measuring the pitched and rolled distance provided the length and width information of the covered area, and since the UAV heading was always fixed along the length, averaging yaw across the entire flight gave the heading direction information. The scan width and overlap percentage are necessary to determine the number of turns that UAV needs to perform while scanning the area, which primarily depends on the user's point cloud density requirement. Smaller scan width is desirable for higher accuracy; however, it is addressed by decreasing distance between adjacent flight paths and increasing flight trips needed to scan the same area. Similar to scan width, the higher overlap is essential for stitching adjacent scans, which allows a higher number of features for matching. With increasing overlap, the number of flight trips increases as well. Figure 18 shows the

58

removal of takeoff and landing sections followed by extraction of pitched and rolled portions of the flight. Averaging the blue path and green path (Figure 18(b)) gives the estimated length and width.

Table 4. Greenhouse parameters needed for generating flight path.

Parameter	Value	Unit
Length	Average distance of pitched portions	m
Width	Average distance of rolled portions	m
Altitude	Average height of each portion	m
Heading	Average yaw of each portion	radians
Scan width	User input, desired LiDAR scan width	m
Maximum speed	User input, desired UAV speed	m/s
Flight Pattern	User input, Figure 7 or Figure 8	
Overlapping percentage	User input	percent

```
                          ┌─────────┐
                          │  Start  │
                          └────┬────┘
                               │
                               ▼
              ┌──────────────────────────────────┐
              │  Initiate recording sensor data   │
              │       from IMU and Guidance       │
              └────────────────┬──────────────────┘
                               │
                               ▼
              ┌──────────────────────────────────┐
              │  Takeoff and manually fly the     │
              │  drone multiple time along the    │
              │          scan boundary            │
              └────────────────┬──────────────────┘
                               │
                               ▼
              ┌──────────────────────────────────┐
              │  After landing stop recording and │
              │   send the raw sensor data to GCS │
              └────────────────┬──────────────────┘
                               │
                               ▼
              ┌──────────────────────────────────┐
              │  Synchronize IMU and Guidance     │
              │   data based on global timestamp  │
              └────────────────┬──────────────────┘
                               │
                               ▼
              ┌──────────────────────────────────┐
              │    Filter data from takeoff to    │
              │             landing               │
              └────────────────┬──────────────────┘
                               │
                               ▼
              ┌──────────────────────────────────┐
              │  Identify and extract pitched and │
              │       rolled portion of flight    │
              └────────────────┬──────────────────┘
                               │
                               ▼
              ┌──────────────────────────────────┐
              │  Calculate length, width, average │
              │  heading of greenhouse, and       │
              │           flight altitude         │
              └────────────────┬──────────────────┘
                               │
                               ▼
              ┌──────────────────────────────────┐
              │  Combine it with user inputs and  │
              │  export the dataset for           │
              │       generating flight plan      │
              └────────────────┬──────────────────┘
                               │
                               ▼
                          ┌─────────┐
                          │   Stop  │
                          └─────────┘
```

Figure 6. Flowchart for extracting greenhouse dimension, orientation, and other related variables for generating flight path.

60

3.2.2 Automated flight route planning

Previous study (Christiansen et al., 2017) has shown that flight path pattern affects the point cloud density, thereby affecting the estimated object volumes. Additionally, a review of past works has shown that flight altitude (Anthony, 2017; García-Quijano et al., 2008; Sofonia et al., 2019) and travel speed (Addis et al., 2018; Yan et al., 2018; L. Zhang and Grift, 2012) have a significant impact on point cloud quality. Consequently, these parameters were pre-defined, and a flight plan was generated accordingly. Once these parameters are defined, the UAV is expected to precisely achieve, maintain and repeat these flight variables in every run, which could be challenging for a manual pilot. Moreover, variation (fluctuation) in these parameters during data extraction (aerial scanning) can affect the data quality of the scan, thereby necessitating the requirement of automating UAV navigation.

The current study considered four flight patterns, as illustrated in Figure 7 and Figure 8. In pattern A (Figure 7(a)) and B (Figure 7(b)), the UAV moved along the greenhouse length and width, respectively. Since both patterns provide a different perspective of the scanning area and have varying battery consumption, it is necessary to assess flight parameters. The pattern C (Figure 8(a)), D (Figure 8(b)) is similar to patterns A, B, respectively, except that UAV makes 180˚ turn before the start of each pitch path. The reason for choosing patterns C and D is the off-nadir scanning. Although patterns C and D will consume extra battery compared to A and D, respectively, due to 180˚ yaw rotation, it will also capture the different viewing geometries of the object. However, for

61

this study, only single path travel was considered. The rolling distance and the total

number of turns were calculated based on equations ((2) and (3)).

$$shift = \left(1 - \frac{overlap}{100}\right) * width_{LiDAR} \qquad (2)$$

Where, $'shift'$ is the distance between two adjacent flight paths

$'overlap'$ is the percent overlap requirement

$'width_{LiDAR}'$ is the total scan width of the LiDAR

$$turns = round\left(\frac{width_{greenhouse} - width_{LiDAR}}{shift} + 1\right) \qquad (3)$$

Where, $'turns'$ is the total number of turns that UAV needs to make

$'width_{greenhouse}'$ is the total width of the scanning area

$'width_{LiDAR}'$ is the total scan width of the LiDAR

$'shift'$ is the distance between adjacent flight paths
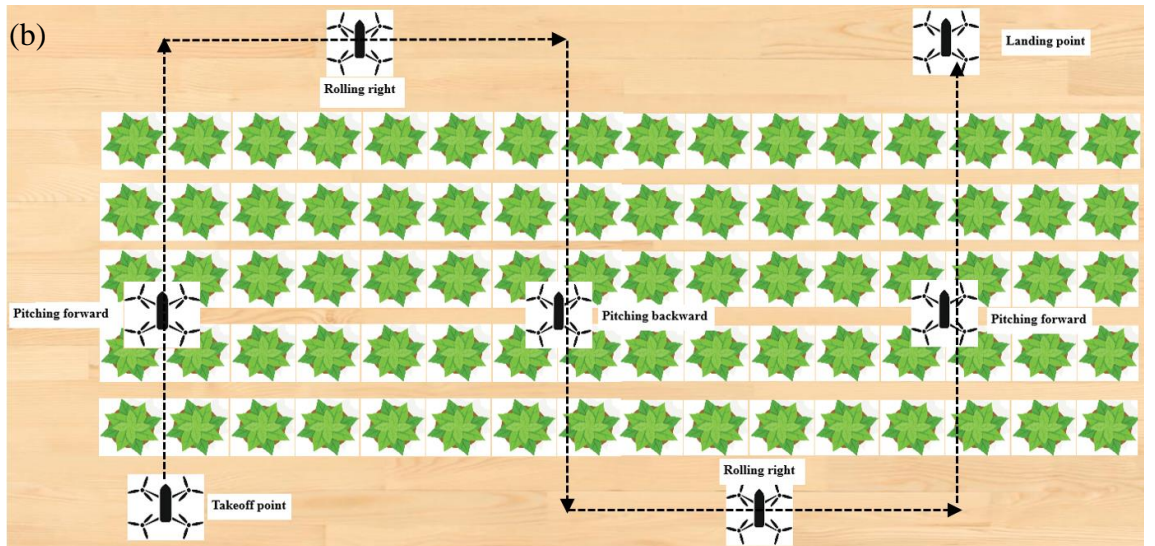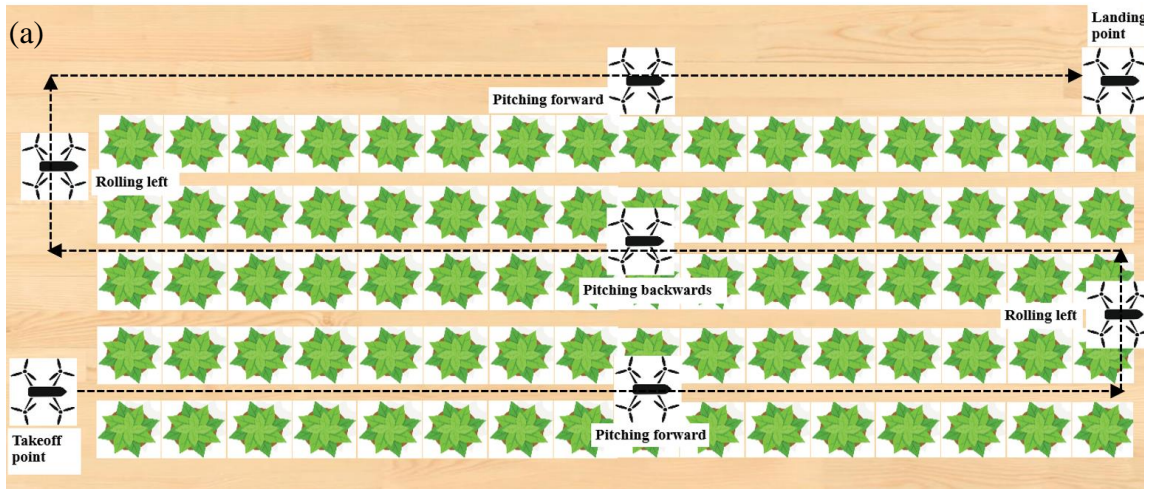
Figure 7. (a),(b) illustrates the Flight pattern A, B in which the UAV pitches along the length, the width of the scan area, respectively, without changing its heading (always facing along takeoff direction), and adjacent path pitch in the opposite direction.
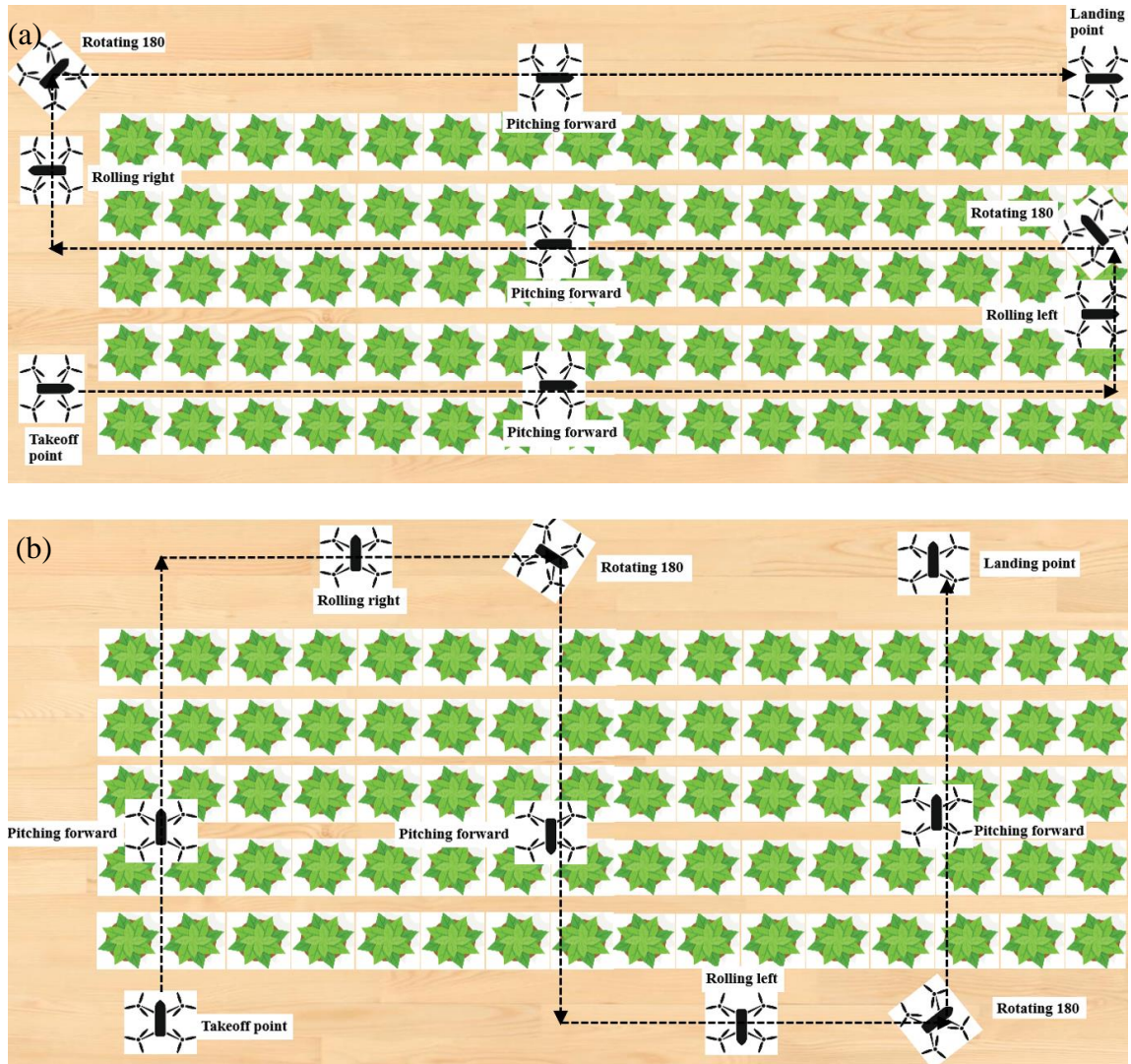
Figure 8. (a), (b) illustrates the Flight pattern C, D in which the UAV pitches along the length and width of the scan area, respectively, changing its heading by 180˚ between adjacent pitching paths such that pitch direction is always positive.

3.2.3 Onboard flight control

A custom ROS-based C++ program acquired flight commands from GCS and sequentially executed them to navigate the UAV along a pre-defined path autonomously on the onboard computer. Figure 9 illustrates the algorithm for autonomous flight control. The most common navigation methodology is to define waypoints (points of interest) on the map. However, the UAV is operating in a GPS denied environment, so neither global

64

coordinates were available to define the waypoints, nor any indoor maps were available/generated. Consequently, it was infeasible to implement position-based control, wherein UAV navigates to a pre-defined position based on 3D coordinates. As a result, flight attitude-based control was implemented wherein pitch and roll angle parameters were used to control the translation and yaw angle to maintain the UAV heading. A positive and negative pitch angle moved the UAV forward and backward, whereas a positive and negative roll angle moved it right and left, respectively. The algorithm measured the difference between the desired value and current value, and the control signal was sent to minimize that difference. For instance, to navigate the UAV along the longitudinal axis of the scan area, it was pitched continuously at a fixed angle, altitude, and heading. The algorithm used each path's start point as the origin, and in each iteration, it calculated the current distance of the UAV from the origin. From this information, the remaining distance (desired length – current distance) was calculated, and the target pitch signal was sent until this value reached below the threshold (30 cm). The algorithm employs a simple on-off control methodology with an operating frequency around 38 Hz, which is limited by LiDAR operating frequency (since the algorithm waits for LiDAR-derived height, which is running at around 40 Hz.). The pitch angles were used to set the travel speeds of the UAV, which were experimentally determined by manually flying it at fixed velocities (real-time velocity from Guidance) and recording the corresponding pitch angles (from IMU). Table 5 shows the threshold parameters used in this control. The decision of sending commands was sequential, i.e., after takeoff, (1) orientation command is sent, (2) non-orientation (pitch) commands, (3) orientation

command, (4) non-orientation (roll) command, and then sequence is repeated depending on the number of turns, and after the end of the flight, UAV will land. If the path has no turns, UAV will (1) set orientation, (2) pitch, and (3) land.

Table 5. Threshold parameters for the on-off proportional control of flight variables

Parameter	Dead band
Distance	30 cm
Heading	2°
Altitude	20 cm
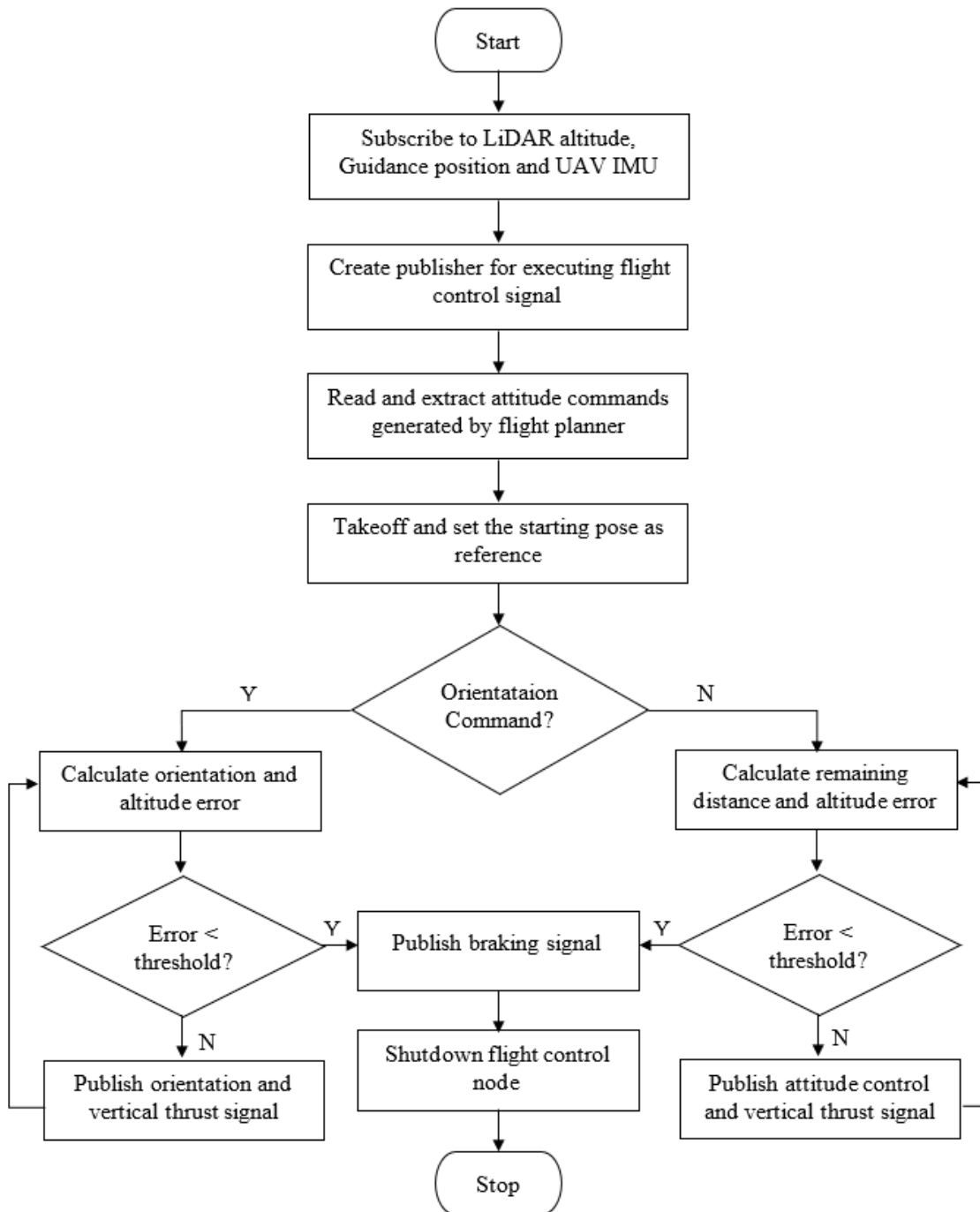
Figure 9. Flowchart of autonomous flight control program written C++ in ROS environment compiled by the onboard computer.

3.3 Autonomous Flight Evaluation

3.3.1 Path tracking

The accuracy of autonomous flights was evaluated by testing the UAV's ability to fly along a straight line. Consequently, a set of wooden logs placed on the floor served as a straight reference line against which UAV's drift was measured. The test was conducted in Student Activities Center, Agricultural Technical Institute, Wooster, Ohio, USA. The venue was chosen due to the enclosed environment and unavailability of GPS signal, allowing to test vision-based local navigation. Two sets of experiments were conducted, wherein the UAV was pitched forward along the test area's length (Figure 11(a)) and width (Figure 11(b)). In both cases, a set of wooden logs was placed on inverted grow pots elevating them to a height of 0.19 m from the ground extracted using LiDAR. This study evaluated navigational accuracy while traveling along a single path; testing the entire flight plan will be part of future efforts. As explained in the flight control algorithm (Figure 9), the UAV was continuously pitched at a fixed angle (based on target velocity) until the target distance was within the threshold resulting in an open-loop operation. To extract the UAV position in flight, the location of wooden logs was used as a reference. Once the flight plan was available from manual flight data, corresponding commands were generated to navigate the UAV autonomously along the wooden logs for a fixed distance (29 m and 22 m along length and width, respectively), at a fixed altitude (2.0 m) and four travel speeds (0.6, 0.8, 1.0, and 1.2 m/s). This resulted in 4 sets of flights along length and width; 6 replications of each set were taken, resulting in 48 datasets (24

along each direction). To compare autonomous and manual flights, similar 48 datasets

were collected but using the manual remote control (RC) (Model GL658C C1, DJI). A

cellphone device with flight software (DJI Assistant, version 2) was connected to the RC,

displaying the UAV's real-time velocity (horizontal and vertical) and altitude from

Guidance. This information was used to fly the UAV at set velocities (0.6, 0.8, 1.0, and

1.2 m/s) and altitude (2.0 m). However, no information regarding horizontal position was

available, which was estimated by visual observation.

During each replication, the sensor data (IMU, Guidance, and LiDAR) was recorded and

saved on the OCS. Post-flight completion, the sensor data was sent to GCS for offline

analysis using a MATLAB-based program. For each dataset following operations were

performed. (1) Extract the location of logs from point cloud data by filtering scan data

that lay between .015 m and 0.30 m from the ground and limiting the LiDAR range

within 6 m (Figure 10-section (c)). (2) Extract the UAV arm's location from the point

cloud by selecting scan data that lay in the angular range of 35˚ to 45˚ (position of the left

arm of UAV with respect to LiDAR angular span 0˚-270˚) and within a radial distance of

0.19 m from LiDAR (Figure 10-section (c)). (3) Both datasets were separately saved and

evaluated.

Two sets of analyses were performed – (a) evaluation of UAV drift, stability and pattern

and (b) variation of flight parameters. In an ideal condition, wherein the UAV travels

parallel to logs, the UAV location will lie on the y axis (y = 0 cm for entire flight duration

from x = 0 to target distance). Consequently, UAV drift was evaluated by measuring the

UAV position along the y-axis. For the first analysis, UAV's position relative to the log

was calculated using UAV's arm and log location from point cloud data. To evaluate the drift, the UAV landing spot (y coordinates) location (which is the end of each flight) was recorded and reported. To evaluate the stability and pattern of autonomous UAV flight, the flight data was sampled at 40 Hz along the travel direction (x-axis), and the corresponding y location of the UAV was recorded. The data was then binned every 10 cm for further analysis. Following two evaluations were conducted – (a) UAV location for the entire path represented by the mean and standard deviation (among six replicates, shown by error bars) and (b) second-order regression model of the combined flight path and R^2 value was reported. The evaluation included both the autonomous and manual flights traveling along the length and width of the test area.

 For flight parameter analysis, the following parameters – speed variation, heading variation, distance to set speed, and total traveled distance during UAV pitching were analyzed for their repeatability and variation.
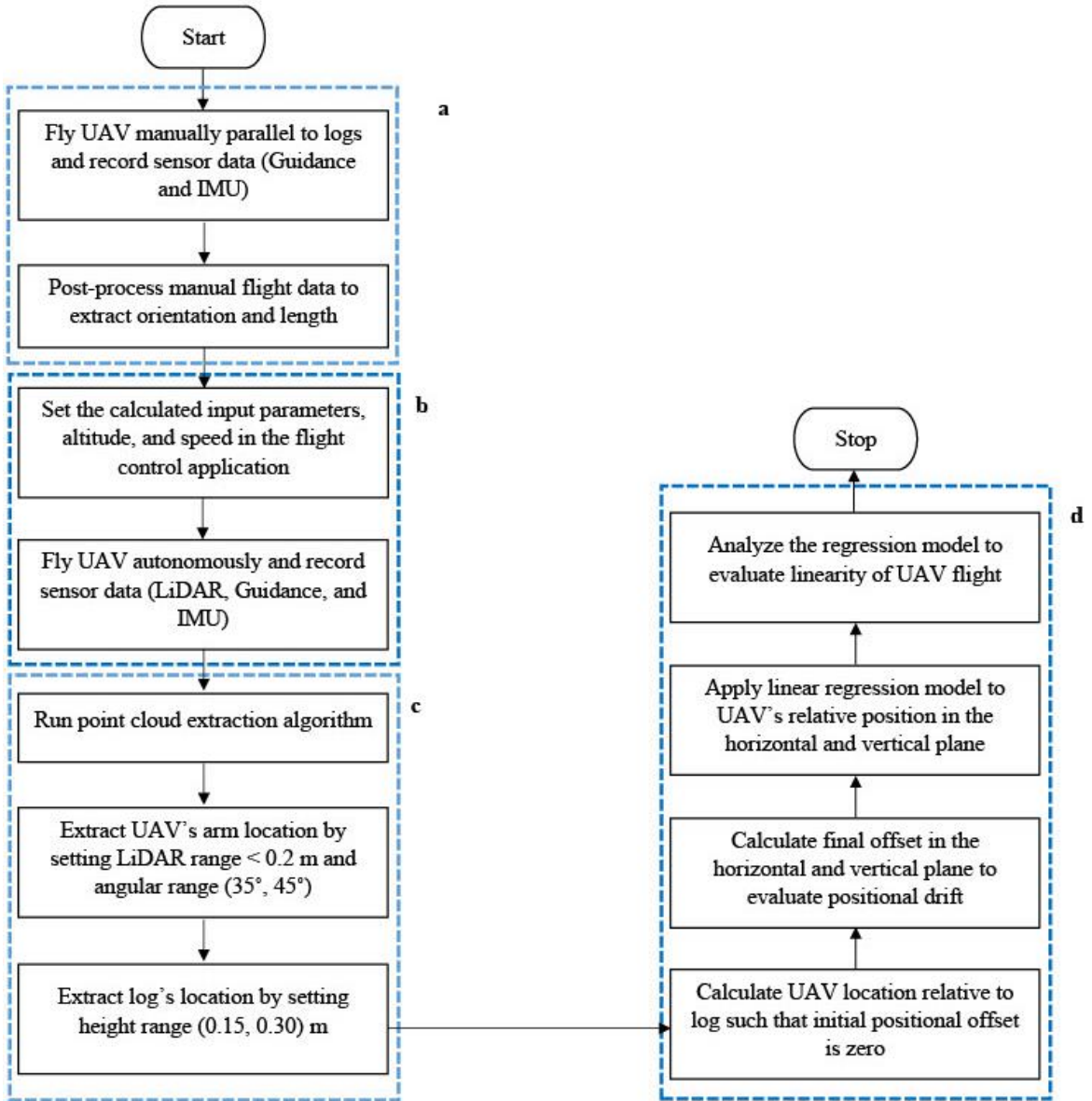
Figure 10. Flowchart of analyzing the accuracy of autonomous flights using wooden logs as a reference to evaluate UAV drift and linearity of the flight path. (a) Process manual flight data, (b) use this information to fly UAV autonomously, (c) extract UAV's arm and log location from point cloud data, and (d) analyze the extracted data.

71

(a)

(b)

Figure 11. Experimental set for evaluating the accuracy of autonomous flights. The wooden logs were placed along a straight line and elevated from the ground by a set of inverted pots. The UAV was placed adjacent to the logs and flown autonomously, and its relative position from logs was evaluated to calculate the drift under varying speeds. Logs were placed along (a) the width and (b) the length of the test area.

3.3.2 Altitude control

3.3.2.1 Baseline for height measurement

LiDAR is expected to be more accurate than Guidance, which calculates UAV height from barometric measurements. Hence, the purpose of this test was to evaluate the accuracy of LiDAR in measuring ground height, and the test was conducted in lab conditions at the Department of Food, Agricultural and Biological Engineering, Wooster, Ohio, USA. The sensing platform was mounted on a constant speed track (Paker Hannifin Corp, USA) at the height of 130 cm (height of LiDAR from the ground), and it traveled 450 cm at three different speeds (0.4, 0.6, and 0.8 m/s). However, the ground was also covered with some artificial plants and standard objects (Figure 12) since the objective also included evaluating the downdraft effect discussed in the later section. To evaluate the performance, height data were binned at every 10 cm for both LiDAR and Guidance. The mean and standard deviation was calculated for both sensors at three different speed.

(a)

(b)
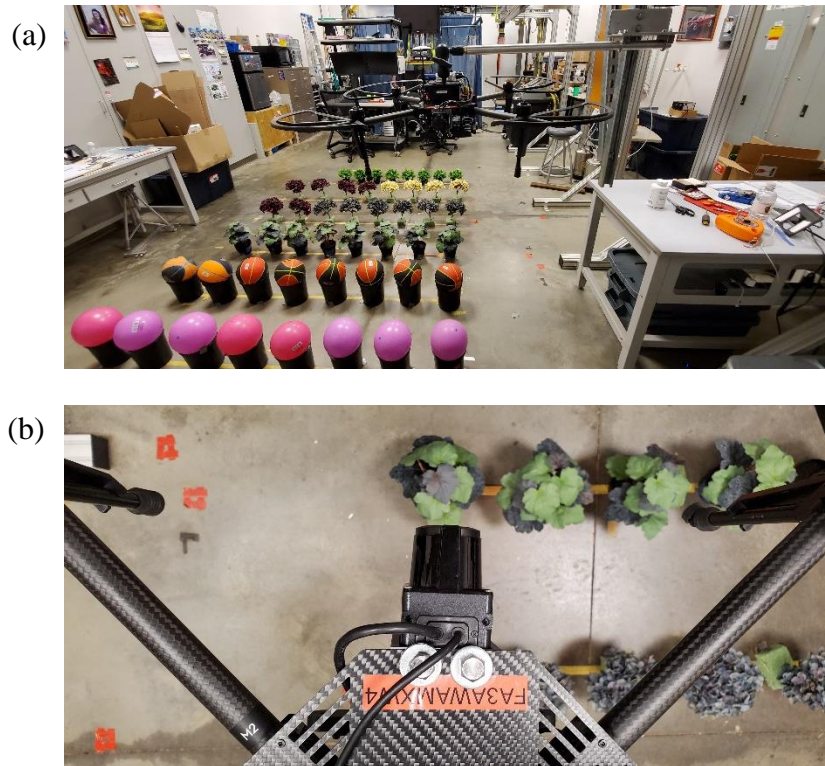
Figure 12. (a) Sensing platform mounted on a constant speed track with test objects on the ground (discussed in downdraft section). (b) View from LiDAR, since the ground was always visible (slightly to the left of LiDAR's center), it was possible to extract LiDAR-derived height.

3.3.2.2 Altitude control performance

Since greenhouses have limited overhead space and UAV has to fly at very low altitudes, it needs to maintain its set altitude to avoid colliding with the ground or overhead structures. Additionally, altitude variation changes the distance of the sensing platform (UAV) to the target canopy, causing variation in LiDAR-derived measurements within the same flight. Hence, it was necessary to evaluate the UAV's performance in reaching and maintaining its height under varying input altitudes.

The current platform had two measurements to determine UAV altitude –height from barometric measurement (from Guidance) and range information from LiDAR. Consequently, the study evaluated the performance of altitude control under both

74

scenarios. Since the LiDAR returns range to the target it hits during a single sweep, it was possible to identify the floor's location in real-time and feed it back to the UAV control system. The test was performed in a lab environment with an empty floor (Student Activities Center, Agricultural Technical Institute, Wooster, Ohio, USA). However, it can be challenging to extract floor location if the ground was covered with plants. Nevertheless, in each LiDAR sweep, the vertical distance between LiDAR and floor is farther than the plants, and the floor can be tracked by observing the z component of LiDAR. Utilizing this concept, LiDAR's z-component was monitored in a 40° angular span (which can be increased), and the minimum among n (= 10) highest values was considered as the distance from the floor. It was assumed that LiDAR would be able to see the ground in each sweep in the given angular span. In contrast, the Guidance-based altitude was directly available based on barometric pressure.

A similar setup as the path tracking experiment was used for evaluating the altitude control performance; however, the setup did not have wooden logs on the floor to allow LiDAR to observe the entire floor without any obstructions. The UAV was flown at three different heights (2.8, 2.3, and 1.8 m) for a fixed speed (0.6 m/s) and a travel distance (20 m). Six replications of each were taken, and both Guidance height and LiDAR-derived height were recorded, resulting in 36 datasets. Two analyses were conducted – (a) comparing Guidance height with LiDAR-derived ground height and (b) comparing the performance of altitude control algorithm using both LiDAR-based and Guidance-based feedback by calculating the UAV altitude variation in LiDAR height and Guidance height, respectively. Although the tests were conducted in an indoor environment, the

75

surrounding environment had open architecture with high ceilings, and the UAV was flying far away from the walls. However, flying the UAV in a greenhouse bay with enclosed architecture (hoop house) can create turbulent air currents after bouncing from nearby walls, ceiling, and floor, affecting surrounding air pressure, resulting in variable altitude measurements from the barometric sensor of Guidance.

3.4 Downdraft Effect on Plant Measurements

As mentioned before, propellers' movement creates a downdraft current of air, affecting plant shape lying underneath the UAV. To measure its impact on measurement accuracy, plants' dimension was measured under propeller running and turned off conditions, respectively. The tests were conducted at the Department of Food, Agricultural and Biological Engineering, Wooster, Ohio, USA. The setup consisted of four sets of artificial plants (P1, P2, P3, and P4) of varying shapes and two sets of balls (B1 and B2) placed on pots. The object dimensions (length, width, and height) were manually measured using a laser measure (GLM40, Bosch, Germany) which served as a baseline. The measurements were taken by considering the distance between the farthest point along the length and width and between the highest point and ground for the height. Three replication of 5 objects from each group were taken (Table 6).
 The plants were chosen based on their varying dimension and stiffness. P1 was relatively denser, compact, and short height; whereas, P4 was tallest and less rigid. P2 and P3 had similar structural characteristics with medium height and most flexibility (P2 was more flexible than P3). The objects with well-defined geometrical shapes (B1 and B2) were

76

chosen for reference as their measurement was expected not to be affected by the downdraft current. Additionally, placing the balls on the pots resembled a plant canopy. Comparatively, the surface of B1 was less reflective than B2; additionally, they had a smaller deviation in their actual diameter (Table 6). Consequently, B1 was chosen as a reference for the standard object.

Eight objects of each kind were selected and placed at an increasing horizontal distance from UAV's center (origin), with the first object placed directly underneath the UAV. Within the row, plants were placed to avoid overlapping with adjacent plants, and spacing between adjacent rows was kept at 0.25 m (Figure 13(a)). The mean intra-row spacing varied for different rows due to varying object dimensions, which were as follows – 0.21, 0.24, 0.24, 0.25, 0.25, and 0.25 m for objects P1, P2, P3, P4, B1, and B2, respectively.

The UAV was mounted on a constant speed track (Parker Hannifin Corp, USA) (Figure 13(b)), allowing it to travel along a straight line at a fixed altitude. Based on the review of past literature, the following parameters were selected for downdraft evaluation – speed (0.4, 0.6, and 0.8 m/s), altitude (1.3 m), and viewing angle (off-nadir about pitching axis, 0°, 20°, and 35°). The downdraft effect was isolated by measuring the plant dimension under propeller turned on and comparing it to propeller turned off measurements. The following plant measurements were calculated – width (along the sensor scanning direction), length (along the travel direction), and height (normal to the ground). However, the movement of propellers and operating motors also create vibration effects

which were considered as an uncontrolled variable. In the future, the effect of vibration can be eliminated (or reduced) by using dampers.

The plant measurements taken under the propeller off condition served as baseline data to compute the relative measurement error under the propeller on condition. Three parameters were calculated and reported – (a) comparing measurement error under propeller running with propeller turned off using root mean squared error (RMSE) as the statistical parameter (equation (4)), (b) evaluating measurement variability in repeated tests using the coefficient of variance (CV(%) using equation (5)) with propeller running and (c) comparing measurement error under propeller turned off with actual object dimension using root mean squared error (RMSE) as the statistical parameter (equation (6)).

Two evaluations were conducted based on these results – (a) identifying the region of influence of propeller downdraft on plant measurements and (b) effect of changing viewing angle on the downdraft measurements.

$$RMSE_{rel} = \sqrt{\frac{\sum_{i=1}^{6}(d_i - d)^2}{6}} \qquad (4)$$

Where, $'RMSE_{rel}'$ is the root mean square error in measurement with

propeller turned on compared to propeller turned off

$\quad 'd_i'$ is the dimension (height, width, length) of the object with

propeller turned on

$\quad 'd'$ is the average dimension (height, width, length) of the

object with propeller turned off

$$CV \ (\%) = \frac{\sigma_i \times 100}{\bar{d}} \qquad (5)$$

Where, $'d_i'$ is the dimension (height, width, length) of the object with

propeller turned on

$\quad 'd'$ is the average dimension of the object with propeller turned

$$RMSE_{true} = \sqrt{\frac{\sum_{i=1}^{6}(d_i - d)^2}{6}} \qquad (6)$$

Where, $'RMSE_{true}'$ is the root mean square error in measurement with propeller turned off compared to their actual measurements

$'d_i'$ is the dimension (height, width, length) of the object with propeller turned off

$'d'$ is the actual dimension (height, width, length) of the object

Table 6. Dimensions of test objects used for evaluating downdraft analysis. Standard deviations are in parenthesis. All the measurements are in mm.

Group	X (Length)	Y (Width)	Z (Height)	Diameter	Image
P1	179 (5)	186 (6)	192 (5)	-	
P2	161 (8)	213 (13)	240 (6)	-	
P3	168 (5)	206 (6)	249 (8)	-	
P4	212 (8)	240 (16)	283 (13)	-	
B1	-	-	296 (2)	176 (1)	
B2	-	-	312 (8)	183 (6)	
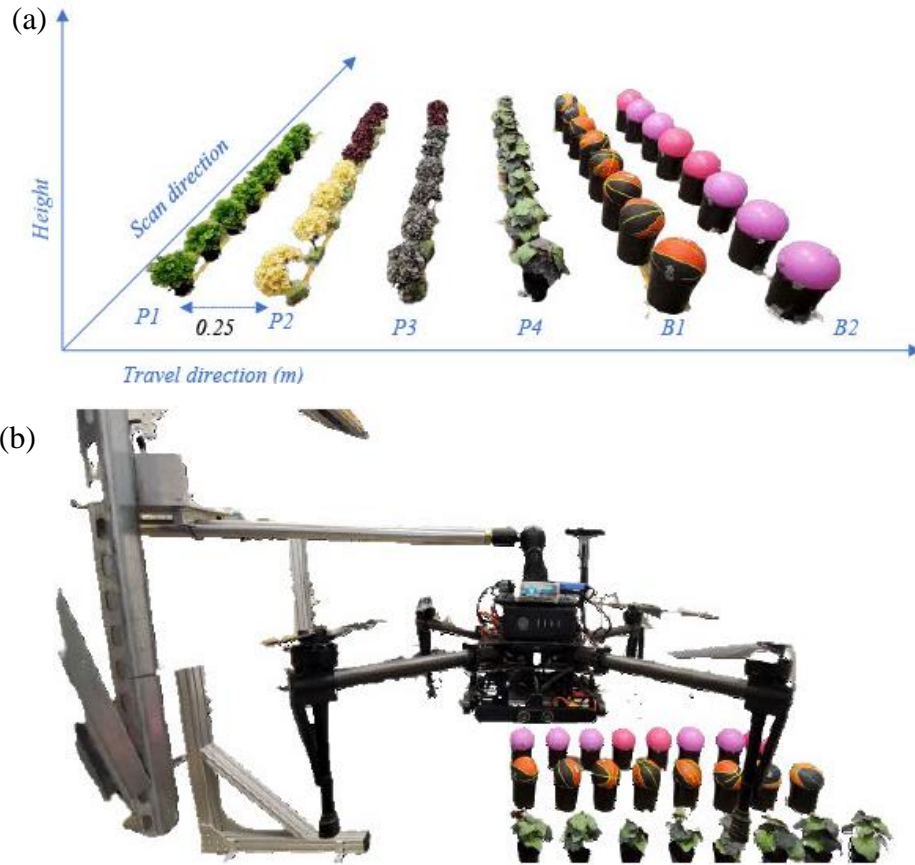
Figure 13. Plant setup for downdraft analysis. (a) Four kinds of artificial plants were selected, and two standard objects of known dimension. Each row was separated by 0.25 m. (b) The plant dimension was recorded at a fixed altitude of 1.5 m by the UAV carrying LiDAR mounted on a constant speed track.

3.5 Plant measurement

The point cloud data was extracted using the methodology explained previously (Figure 5); however, the sensing platform was manually mounted, which could have an alignment error. Consequently, the 0° line of LiDAR (centerline) would not align with the z-axis, resulting in the entire scan being rotated at an angle about the x-axis. However, during the initial portion of the scan (1 m before the plant row P1), the entire floor was visible, which was used to calculate the average inclination of the floor. The entire scan was then

82

rotated by this angle about the x-axis to eliminate this manual error ensuring alignment with the z-axis. Additionally, the floor data was also removed by fitting a plane, and the resulting point cloud was then processed by the Clustering algorithm (developed by Uchit Nair, work is under review). The algorithm generated a convex hull structure enclosing nearby points, and it returned the dimension (length, width, height) of each object.

Chapter 4. Results and Discussion

4.1 Aerial Sensing Platform

4.1.1 Hardware setup

Table 7 illustrates the list of all primary components were used in this platform. The

overall payload was about 908 gm, but this payload also included RAM mounting, which

was used to mount the sensing platform to the constant speed track that weighed around

410 gm. In all the autonomous flight tests conducted in the laboratory, the platform was

carrying this payload. However, the tests conducted in the greenhouse using manual

flights did not have this payload.

Table 7. List of primary hardware components of aerial platform.

Component	Weight (gm)	Dimension (mm)	Power (W)
Matrice-100	2431	650 (Wheelbase)	130 Wh
UST-10LX	130	50 x 50 x 70	3.6
DJI Guidance	325	208 x 208 x 70	12
Odroid-XU4	38	83 x 58 x20	20
Wi-Fi module	5	36 x 19 x 9	-
USB connector (x2)	-	-	-
LiDAR mount (x3)	28, 43, 56	61 x 61 x17	-
UBEC buck converter	-	-	-
RAM mounting	410	120 x 120	-

4.1.2 Software setup

The sensor data were recorded using a custom ROS program run on Odroid XU-4.

Primarily four ROS nodes were used: 1) UAV node to extract IMU (orientation and

acceleration) data and control UAV operations, 2) Guidance node to extract position and

velocity, 3) LiDAR node to extract range data and UAV height and 4) Flight Control

node to execute autonomous flight.

Table 8. List of nodes running in ROS

Sensor/Node	Frequency (Hz)	Output/Input Data
IMU	100	Orientation -Quaternion (w x y z)
		Linear acceleration - (a_x a_y a_z)
Guidance	89	Position (x y z)
		Velocity (v_x v_y v_z)
		Range $[r]_{1x1080}$
LiDAR	40	Intensity $[I]_{1x1080}$
		UAV Height (z)
Flight Control	38	Attitude (r p y)

4.1.3 Generating point cloud data map

To evaluate the working of the established aerial platform, it was manually flown in a commercial greenhouse (Cedar Lane Farms Inc, Wooster, Ohio, USA) which had a closed hoop-house architecture (Figure 14). This test aimed to record scan data and test the working of MATLAB-based algorithm to generate the 3-D model of crops. The algorithm combined LiDAR (range and intensity), Guidance (position and velocity), and IMU (heading) data to create a point cloud object of the entire dataset. It also identified and reduced the error due to UAV drift, heading instability, and altitude variation. To maintain homogeneity across all scans, the x-axis was chosen as travel direction (primary

axis of UAV travel), y-axis as the scanning direction (orientation of LiDAR scan lines), and the ground was maintained at z = 0 m.

Figure 15(a) shows raw point cloud data that transformed LiDAR range data into cartesian coordinates followed by translating each point along the Guidance derived coordinates. In this step, the primary axis of travel was identified, oriented along the x-axis. In the next step (Figure 15(b)), UAV drift was aligned along the y-axis, and each scan point was translated along these coordinates to eliminate the drift error. Its effect is evident in Figure 15(a-b), where the crop rows were curved due to UAV's movement along the scanning (y) axis. However, this caused the entire scan to rotate about the z-axis. Consequently, the entire scan was aligned along the x-axis by calculating flightpath orientation (relative to the x-axis) and rotating the scan by the same angle in the opposite direction (Figure 15(c)).

Figure 16 shows the effect of UAV altitude variation on the scan data quality. To illustrate this effect, only floor data has been shown. In the original scan (Figure 16(a)), the floor location is not aligned with the z = 0 m line. Additionally, when the UAV was at 15 m from the origin, it gained some altitude, increasing the distance between LiDAR (mounted on UAV), which resulted in moving the entire scan away from the UAV. The scan was corrected by keeping the ground at zero levels using Guidance-derived height (Figure 16(b)). However, LiDAR-derived height was also available for correction (Figure 16(c)), which is more accurate than barometric measurement (Guidance height), but it could be a challenge to detect floor in densely packed greenhouse floor. Currently, Guidance derived height has been used for height correction.

Finally, Figure 17 shows the effect of variation (fluctuation) in UAV heading on the data quality of the scan quality. In this particular set (Figure 17(a)), the initial UAV heading (shown in the red box) was incorrect (caused due to manual piloting error) and slightly clockwise along the z-axis, which caused the LiDAR scanning plane to rotate with UAV and to result in inclined crop rows (relative to the y-axis). This was removed by rotating each scan line by heading error (relative to mean heading across the entire flight).

(a)

(b)
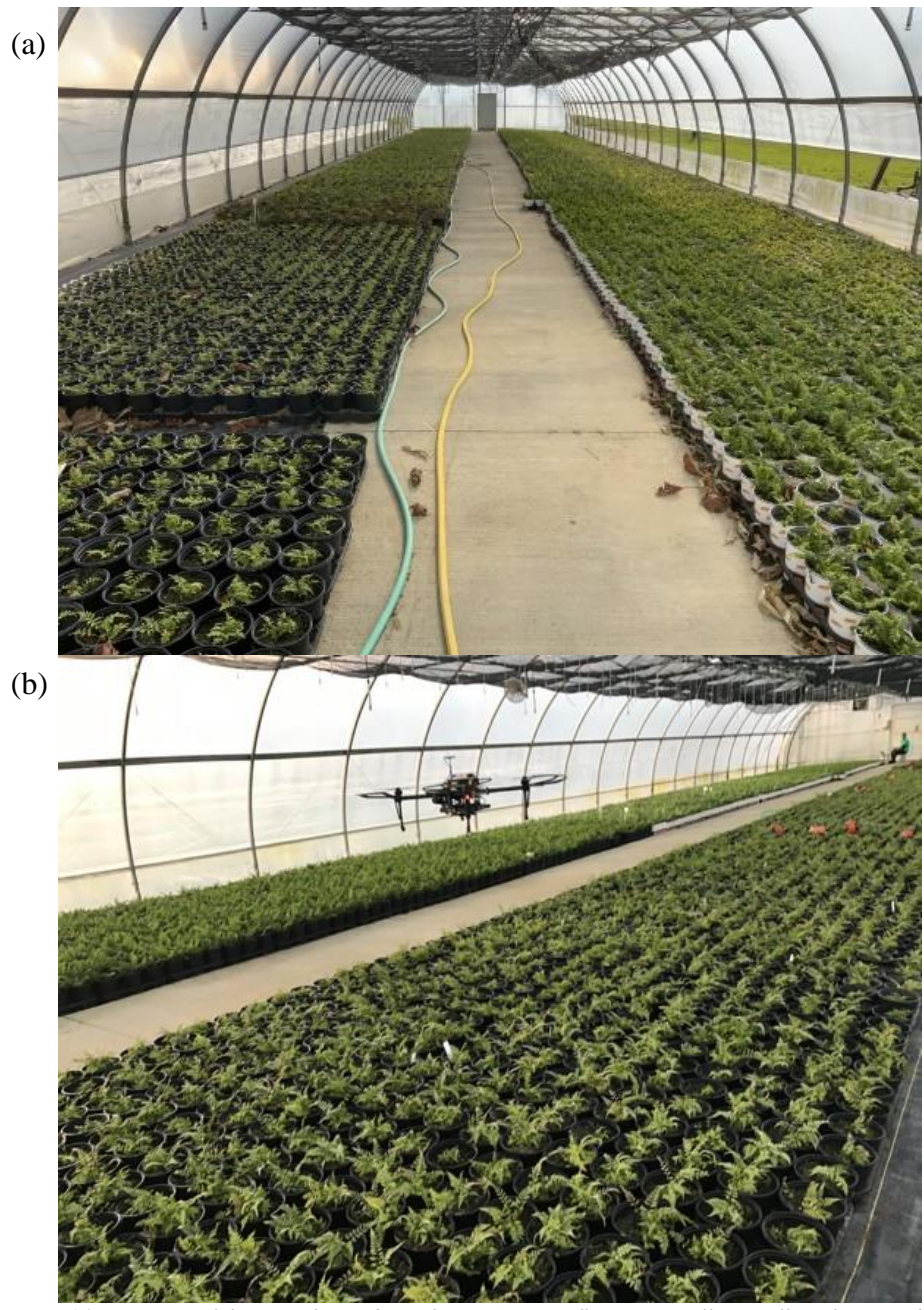
Figure 14. (a)Image of the greenhouse bay where UAV was flown manually to collect the crop data. (b) Image of UAV collecting sensor data.

89
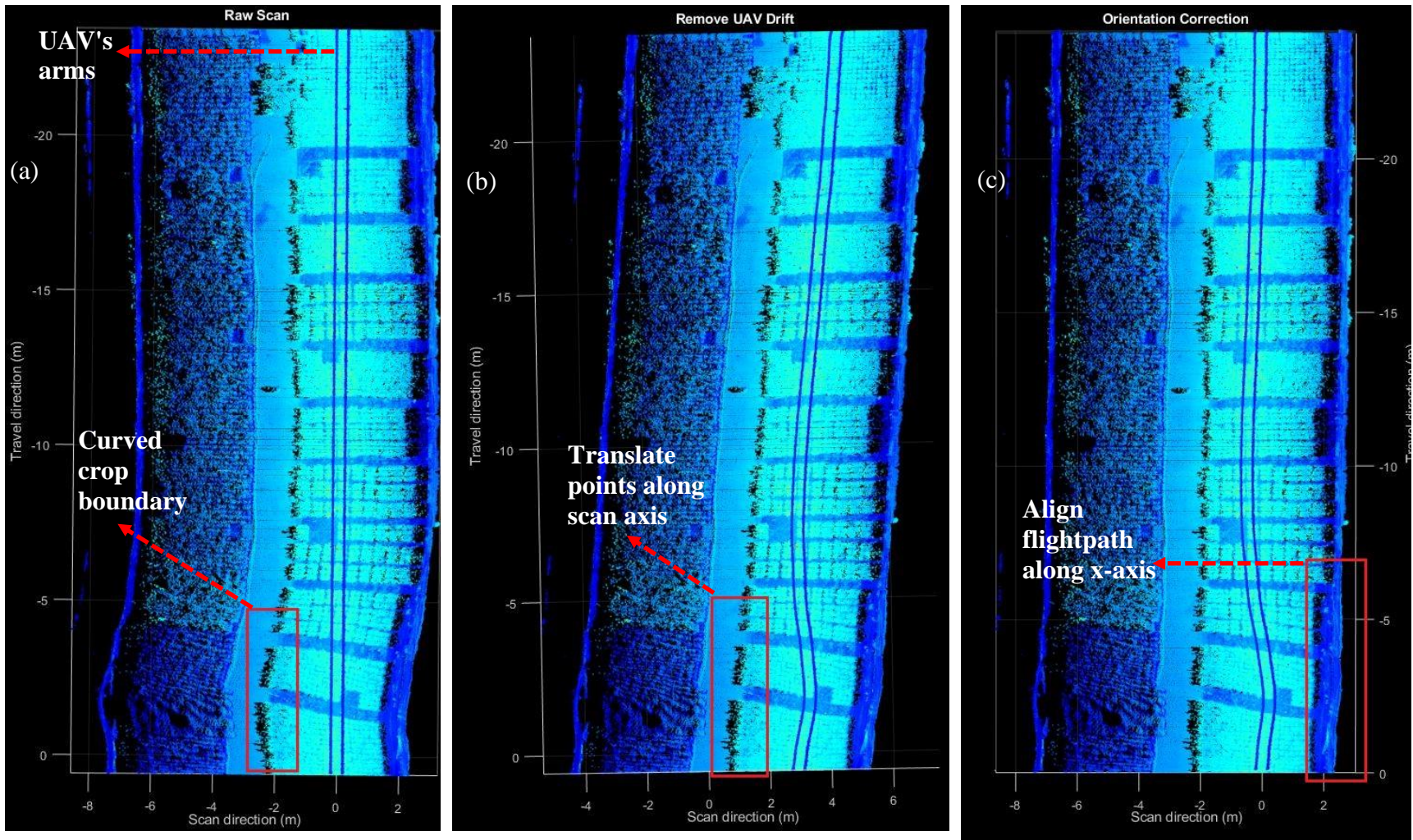
Figure 15. (a) Raw scan generated by converting laser range data to cartesian coordinates and translating each scan line along the Guidance-derived UAV position. The two parallel lines centered around the 0 m line of scanning (y) axis are the UAV arms, indicating the UAV position. The red boxed region shows UAV drift's effect along the scanning axis, which caused the curving of the crop boundary. (b) Translate each point along the scanning axis (y-axis) to compensate for UAV drift. (c)) Reorientation of the flightpath to align it with the travel (x) axis.

90
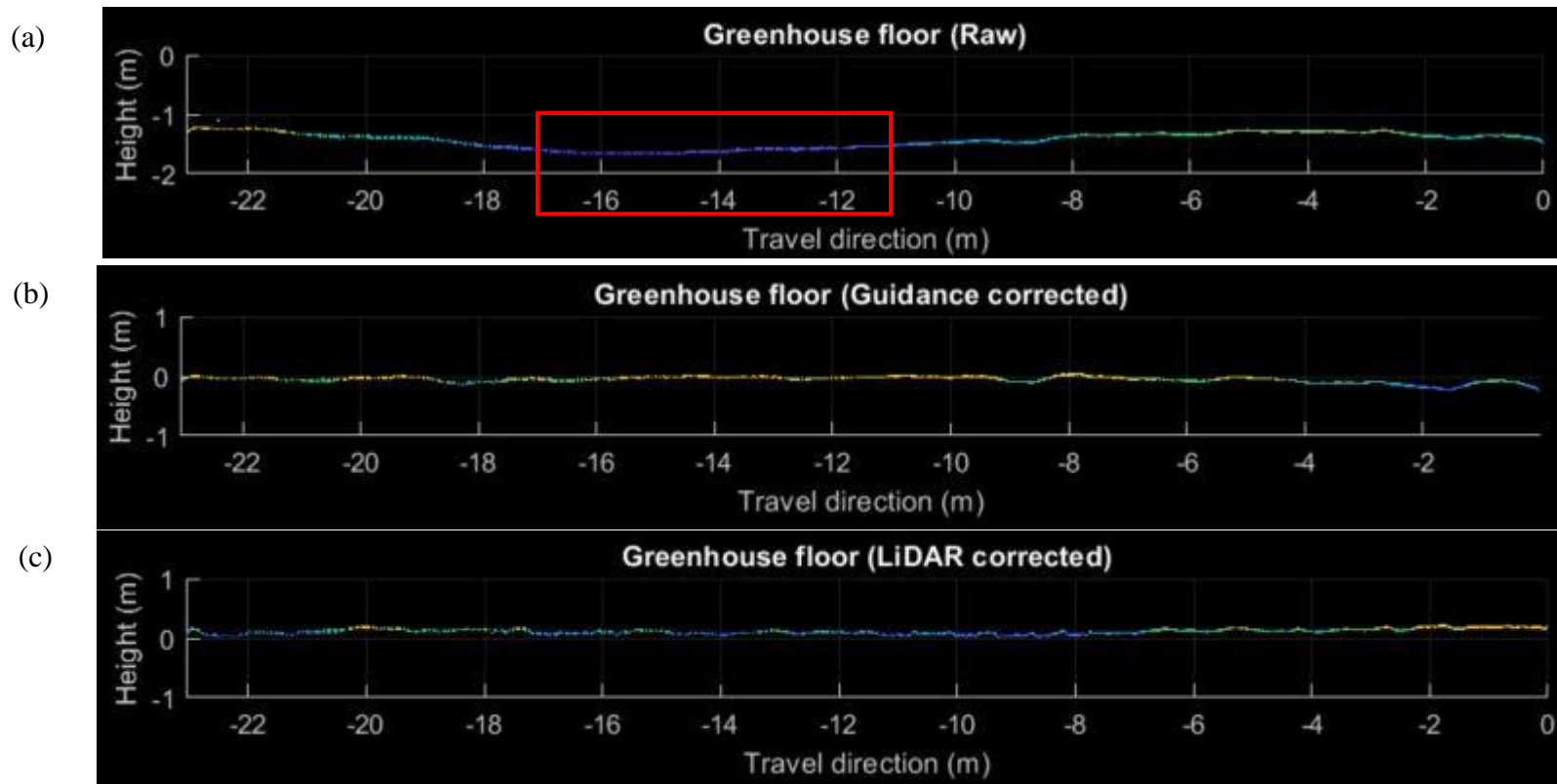
Figure 16. (a) Representation of the height error in scan due variation in UAV altitude. At around 12 m -16 m from the origin (shown in the red box), UAV gained altitude, which pushed the greenhouse floor away along the z-axis. (b) UAV height data was available from Guidance which was used to correct this anomaly. (c)Using LiDAR-derived height to correct the height error.
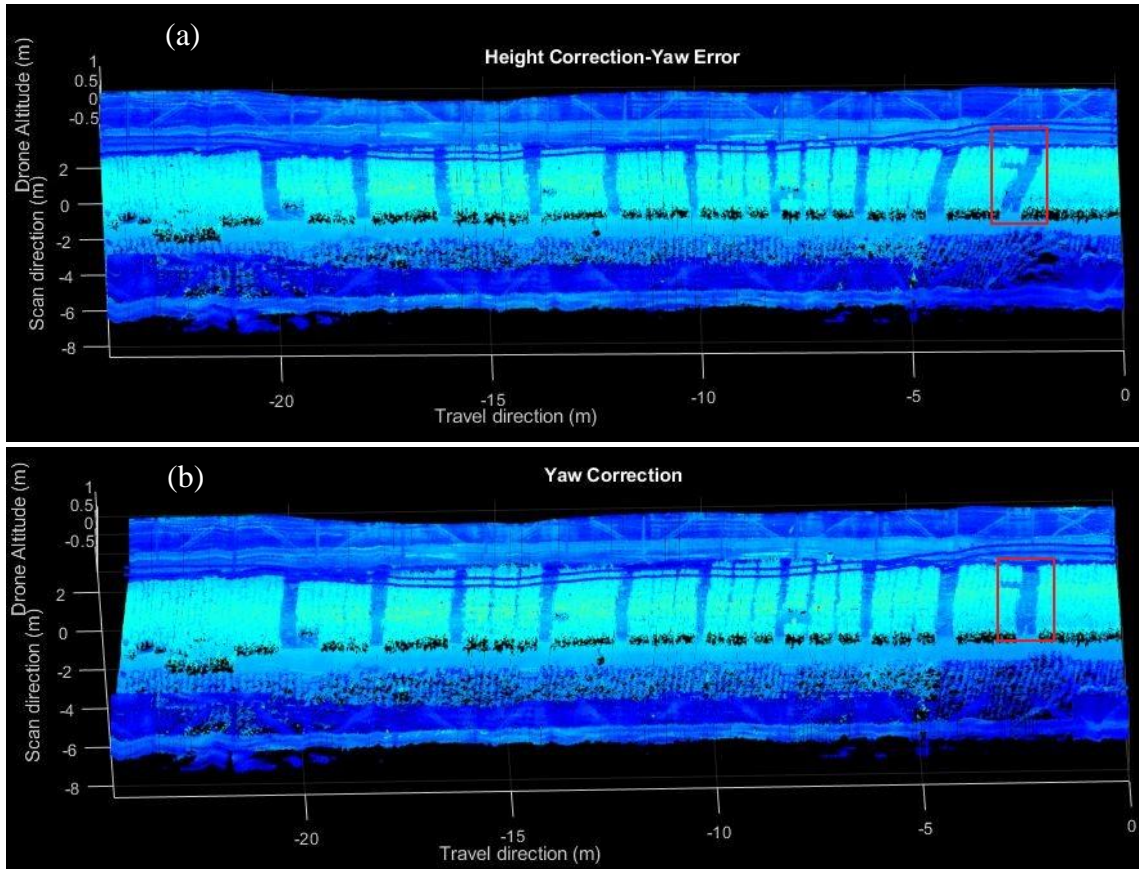
Figure 17. (a) Representation of the effect of varying UAV heading. The figure shows the side view (y-z). The space between crop rows at 2.5 m from the origin (shown in the red box) is not straight due to a sudden UAV heading change. (b) Correction of the error caused to UAV heading variation resulting in crop rows aligned with scanning (y) axis, shown in the red box.

4.2 Autonomous Navigation

4.2.1 User-defined flight area

The purpose of this operation was to define the flight area and extract its dimension and heading. Figure 18Figure 18 illustrates the result of the flightpath extraction algorithm (Figure 6) from manual flights. Post-removal of takeoff (shown by a red diamond-shaped portion of Figure 18(a))and landing portions (shown by a green square-shaped portion of Figure 18(b)), pitched and rolled portions were isolated (Figure 18(b)). Averaging the distance of pitched (shown by orange square shaped segments Figure 18(b)) and rolled

92

portions (green shown by pink circular-shaped segment Figure 18(b)) gave the length and width. Averaging the altitude and yaw angle across the entire flight path (blue Figure 18(a)) gave the UAV height and heading.
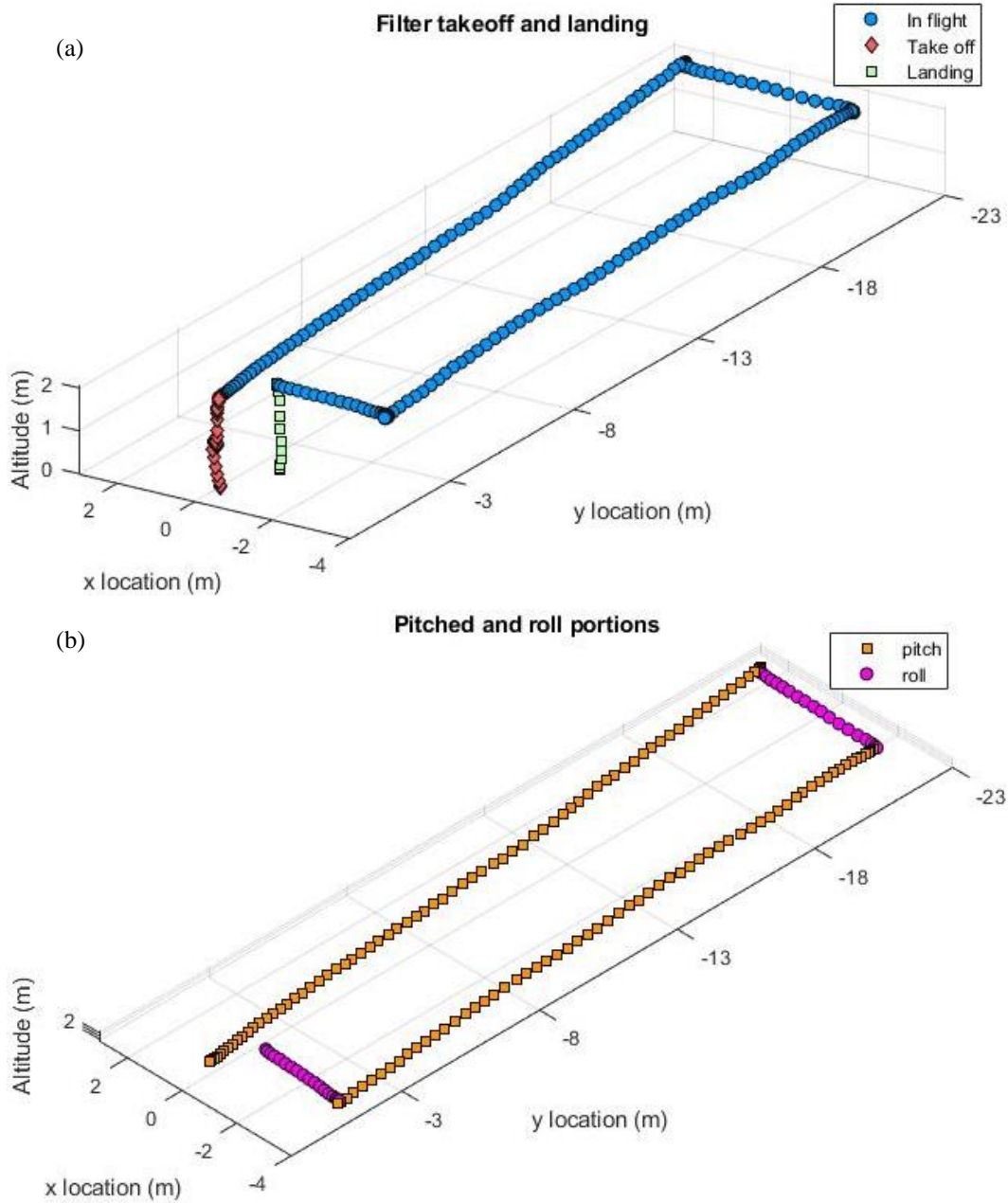
Figure 18. Plot of a manual flight flown across the boundary acquired from Guidance. (a) Identification and removal of takeoff and landing portions, (b) identifying pitched and rolled flight sections. The purpose of this manual flight is to define the flying area and extract dimension and heading information.

94

4.2.2 Automated flight route planning

A graphical user interface (GUI) application was developed using Qt (Qt creator, 4.11.0, community version) to simplify the communication between the ground computer and onboard computer. Secure Shell (SSH) protocol was used to establish communication between the two systems using available WiFi networks in the test region. The OCS was configured to connect to the ground computer's hotspot automatically.

4.2.2.1 GUI flight planner

The Qt application generates flight path patterns using based on the MATLAB computation of the manual flights. Figure 19 shows a snapshot of the flight planner's main window.
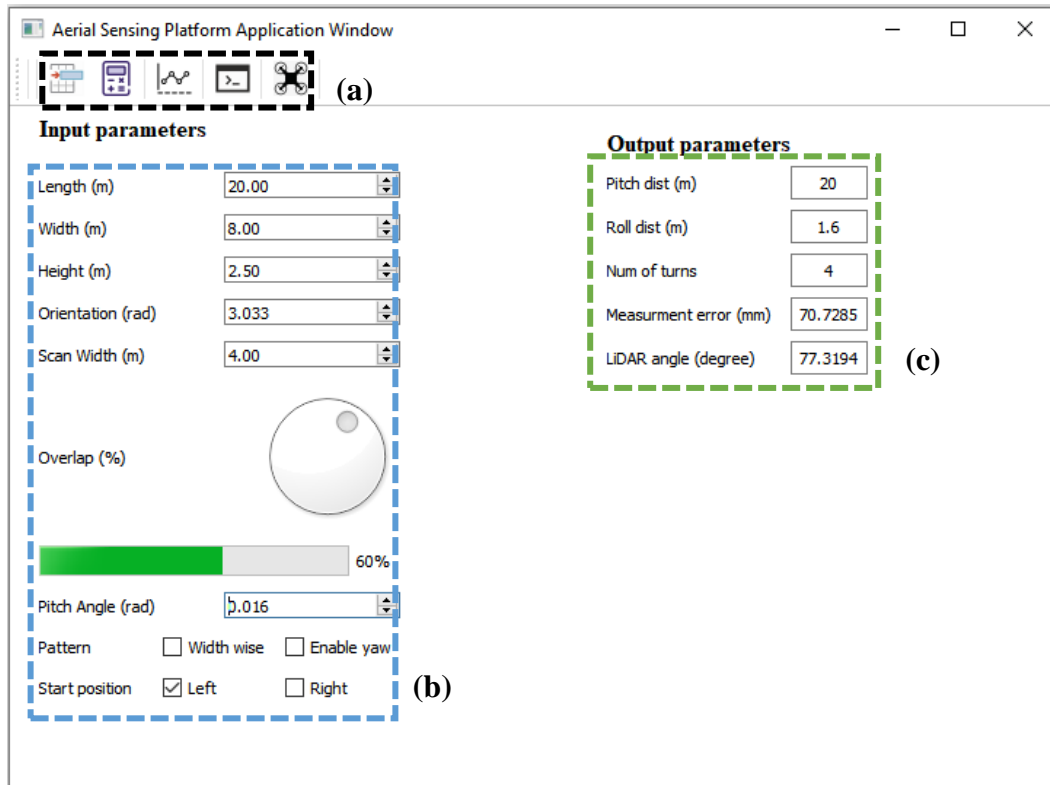
Figure 19. Qt-based GUI console for generating flight plans and commands based on flight area dimensions and scanning parameters. (a) Five input buttons to perform the following operation (left to right) – (1) load greenhouse information and scanning parameters generated by processing the manual flight by MATLAB based program, (2) calculate output parameters based on current input parameters, (3) plot flight path on a 2D graph, (4) generate corresponding flight commands, (5) open UAV control console. (b) Input parameters displayed and editable to test under different conditions. (c) Output parameters.

Section (*a*) *at the top left corner*, marked in the black box, is a collection of clickable

icons that perform a sequential task of extracting a combined dataset from MATLAB

output, generating flight parameters and commands, plotting the flight plan, and

executing the plan. The first icon (*import*) imported the greenhouse structural data

generated from the MATLAB algorithm by extracting manual flight data and displays

them in textboxes of section (b) (blue box) at the bottom left. The second icon (

calculator) calculated flight parameters such as pitching distance, rolling distance, total

number of flight turns, total distance to cover, measurement error along the width, and

96

LiDAR scanning angle. The third icon (plot) plotted the flight path on a 2D plane based on the input variables and allows users to visualize the effect of varying overlap percentages and patterns on the flight path.

The fourth icon (*command*) generated and exported the flight commands based on the flight path. Each flight command comprised roll angle, pitch angle, yaw heading, altitude, and distance data. The command sequence saved in the GCS was sequentially sent to and compiled by the onboard computer. The fifth icon (*launch*) opened a customized flight control console allowing the UAV to compile the flight commands to navigate it in real-time and recording the sensor data for offline analysis.

Section (*b*), marked in the blue box, displayed the input variables as imported by icon 1 of section *a*. The first set of parameters were the greenhouse dimensions and orientation information, including length, width, height, and yaw orientation. The scan accuracy parameters were calculated based on user requirement, which sets the *scan width* and *overlap percentage* between adjacent flight paths. Finally, setting the flight parameters, namely *pitch angle* to control UAV's velocity, and *pattern* which allows scanning along the width (if the checkbox was clicked) and rotated UAV by 180˚(if the checkbox was clicked) after each roll command. Additionally, users can specify the UAV location relative to the test area, whether placed on the left or right corners. The location information was essential since it was used to compute rolling direction; if the UAV was on the left corner, it rolled right and vice versa. These values can be manually edited if the user wanted to test the UAV with different flight parameters.

97

Section (c), marked in the green box, displayed the primary flight information, the pitch

distance, roll distance, number of turns, measurement error along the width, and

minimum LiDAR scan angle to maintain the required overlap. The measurement error

was the maximum width error calculated based on LiDAR's height and scan width.

4.2.2.2 Flight planner's output

The flight planner results were tested with two different overlap scenarios (60% and

40%) and two scanning strategies (along the length and along the width of the scan area),

resulting in four flight patterns (Figure 20). Since the greenhouse dimension was 20 x 8

(L x W) m^2 and LiDAR scan width ($width_{LiDAR}$) was 4 m, the UAV take-off position was

2 m from the boundary and pitch distance (forward travel distance) of 20 m

(=$length_{Greenhouse}$) (Figure 20 (a)). For 60% overlap, the roll distance (sideway travel

distance) was 1.6 m (equation (2)), resulting in 4 flightpaths (equation (3)). However,

with 40% overlap (Figure 20 (b)), the roll distance increased to 2.4 m, allowing a

complete scan in 3 turns rather than 4. Figure 20 ((c) and (d)) generated flight paths along

the width, wherein the pitch distance was relatively smaller (=$width_{Greenhouse}$). However,

the number of turns was significantly higher since the UAV had to roll along the

$length_{Greenhouse}$.
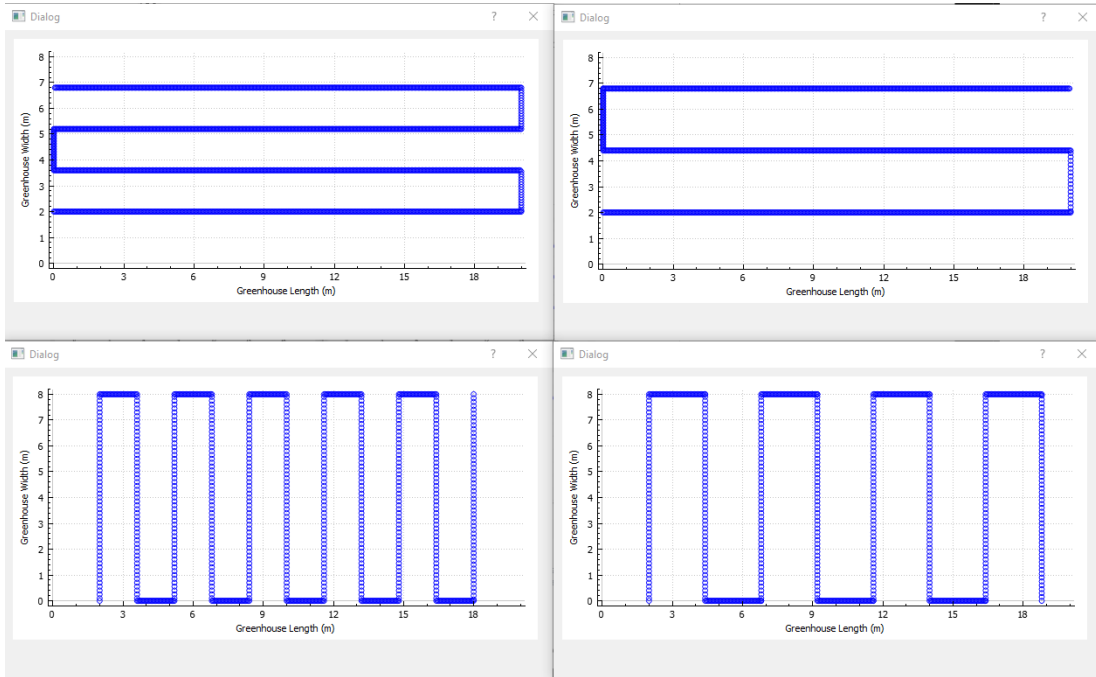
Figure 20. Plot of the flight path with different patterns and overlapping percentages – (a), (b) flying along greenhouse length with 60% and 40% overlap, respectively; (c),(d) flying along greenhouse width with 60% and 40% overlap, respectively.

4.2.3 Onboard flight control application

In order to implement onboard flight control (Figure 9), a Qt-based GUI application was developed and tested. This module allowed users to communicate with the sensors, perform UAV control actions, record data from sensors and export them to GCS by clicking designated icons that execute a set of Linux commands in the background. Figure 21 shows a snapshot of the module, and Table 9 and Table 10 describe the purpose of each icon. The GUI console was divided into four sections based on the operation sequence. Section (a) (Figure 21(a)) starts the sensors (initiates ROS node for each sensor), and once all sensor nodes are ready, the UAV is taken off. Section (b) (Figure 21(b)) starts autonomous UAV navigation (based on the flight plan) either using LiDAR height or Guidance height for altitude control. Section (c) (Figure 21(c))

99

performs post-flight completion operations – land the UAV, stop recording sensor data, terminate all running nodes, and send recorded data to GCS. Section (d) (Figure 21(d)) was created to run tests on the constant speed track. It arms the motors and continuously thrusts the propellers (Hover button) until the UAV is in motion on the speed track. The disarm motors button forcefully stops the propellers, and it was used only for testing and safety reasons. Section (e) (Figure 21(e)) was used for setting parameters – (1) Hover time, which sets the duration (seconds) for which UAV will hover before executing the next command (pitch, roll, or orientation) and (2) Number of replicates, which sets the number replications taken in a given experiment and the OCS processes the set number of recorded sensor datasets and sends it to GCS.
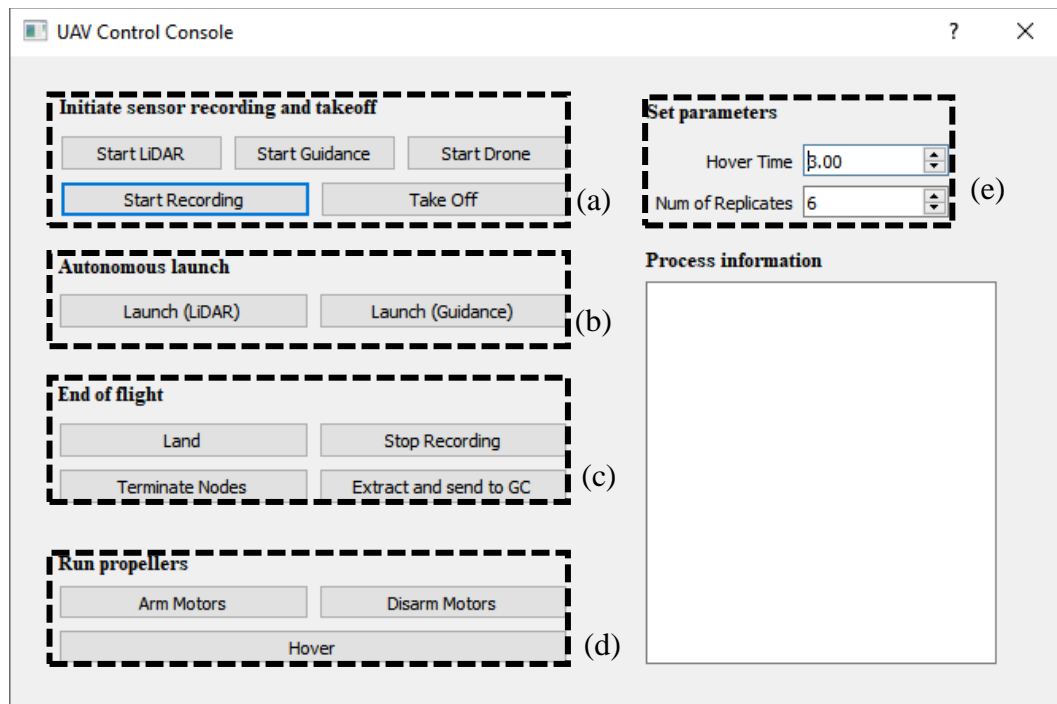
Figure 21. Flight control GUI application - (a) Sensor initialization and takeoff, (b) start autonomous flight either using LiDAR or Guidance sensor for altitude control, (c) end of flight operations (d) run propellers for downdraft tests, and (e) Parameter for hover time and number of replicates taken in the experiment.

Table 9. Operation performed by individual push buttons (1-9). The sequence of operations was based on the Id discussed in the appendix.

Id	Icon	Purpose
1	Start LiDAR	Initiates LiDAR node to extract range and intensity data at 40 Hz
2	Start Guidance	Initiates Guidance node to extract position and velocity data at 85 Hz
3	Start Drone	Initiates UAV node
		Extract IMU data (100 Hz)
		Control UAV motors to follow flight commands
4	Start Recording	Start saving the data published by the three nodes
5	Take Off	To lift and hover the UAV at an altitude of 1.2 m from the ground.
6	Launch (LiDAR)	Execute algorithm for sequentially sending and compiling flight commands to the onboard computer for navigating UAV along a pre-planned path. LiDAR height used for altitude control
7	Launch (Guidance)	Similar to the above step, using Guidance height for altitude control instead of LiDAR height.
8	Land	Land the UAV at the current spot.
9	Stop Recording	Stop saving the sensor data and export it as a timestamped file (.bag format) to a fixed location on the onboard computer.

Table 10. Operation performed by individual push buttons (10-16). The sequence of operations was based on the Id discussed in the appendix.

Id	Icon	Purpose
10	Terminate Nodes	Stop the running nodes (LiDAR, Guidance, and Drone).
11	Extract and send to GC	Select the latest saved dataset based on the timestamp
		Extract individual sensor data.
		Convert to .txt format.
		Send it to GC.
		Delete the latest dataset and repeat the steps mentioned above until all the datasets are processed.
12	Arm motors	Arm the UAV motors.
13	Disarm motors	Disable the motor control.
14	Hover	Algorithm for running propellers on constant speed track by sending thrust commands.
15	Hover Time	Hover time (seconds) between subsequent UAV commands
16	Num of files	Number individual flight datasets.

4.2.4 Evaluation of autonomous flights

4.2.4.1 UAV drift

Figure 22 shows the variation in flightpath pattern, which was determined using only two UAV positions, takeoff, and landing, and landing point variation (Δy when UAV landed) along the y-axis under varying input conditions was reported. While flying along the length (Figure 22(a)), the magnitude of drift (Δy) was greater in autonomous mode than manual mode, which was consistent at around 200 cm. However, the deviations (represented by error bars) were relatively higher at the lowest speed (0.6 m/s), and higher speeds had lower and similar deviations. Additionally, under the autonomous mode, the offset was always negative (in the graph, y = 0 represents the location of reference, and the positive (y > 0) and negative region (y <0) represent the right and left of reference), indicating that UAV always drifted toward left and away from the reference. Compared to autonomous flight, manual flights had relatively smaller drift and were positive, resulting in a drift along the right of the reference. Whereas, offset along the width (Figure 22(b)) was relatively smaller than the length, excluding the case of the lowest speed (0.6 m/s), where the offset was considerably greater.
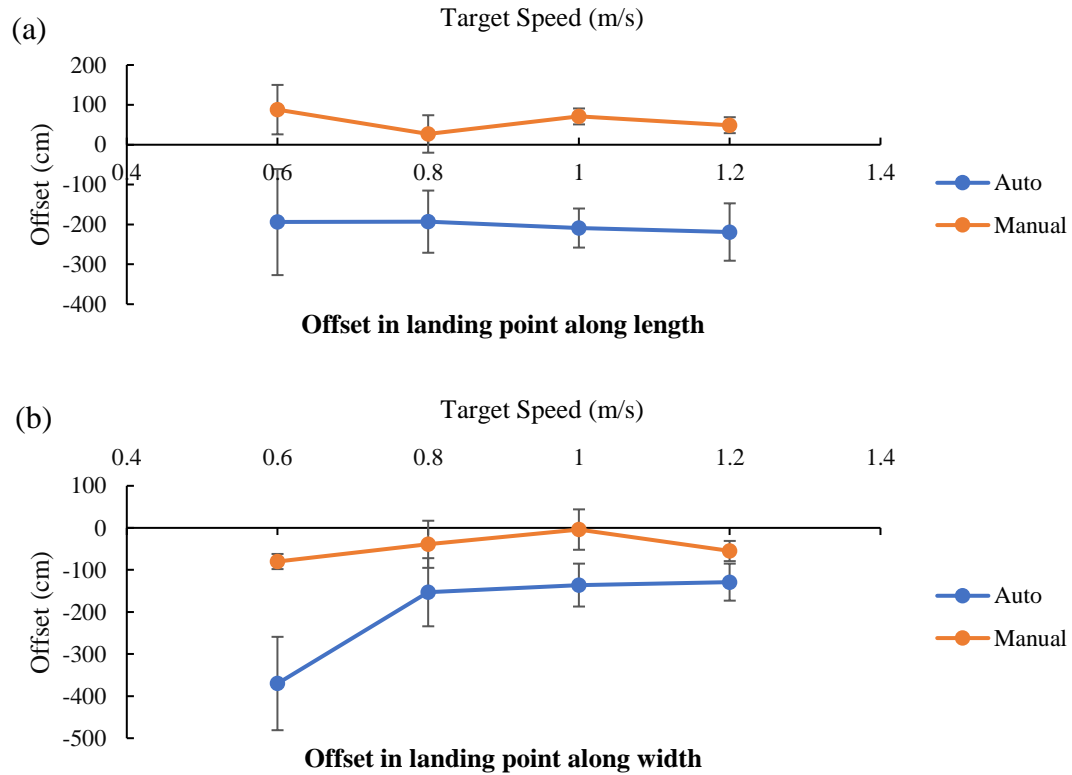
Figure 22. Offset in UAV's landing point along y-axis while flying along (a) length and (b) width at 4 different speeds in autonomous and manual mode.

4.2.4.2 Stability and pattern

Figure 23 shows the flight pattern (blue curve) under 4 different speeds while traveling along the length. The $y = 0$ line represents the log position, the negative region ($y < 0$) and positive region ($y > 0$) represent the left and right of the log. The effect of UAV speed is evident from the plots, which show that increasing speeds resulted in reduced deviations. Additionally, for a given speed, the deviation increased with travel distance. For manually flown flights (Figure 24), for a given speed, the UAV location was closer to the reference (blue line), and also the deviation relatively smaller compared to autonomous flights.

Figure 23. Effect of increasing UAV speed on autonomous navigation performance, while travelling for a fixed distance (2800 cm) along length at four different speeds - (a) 0.6 m/s, (b) 0.8 m/s, (c) 1.0 m/s, and (d) 1.2 m/s.
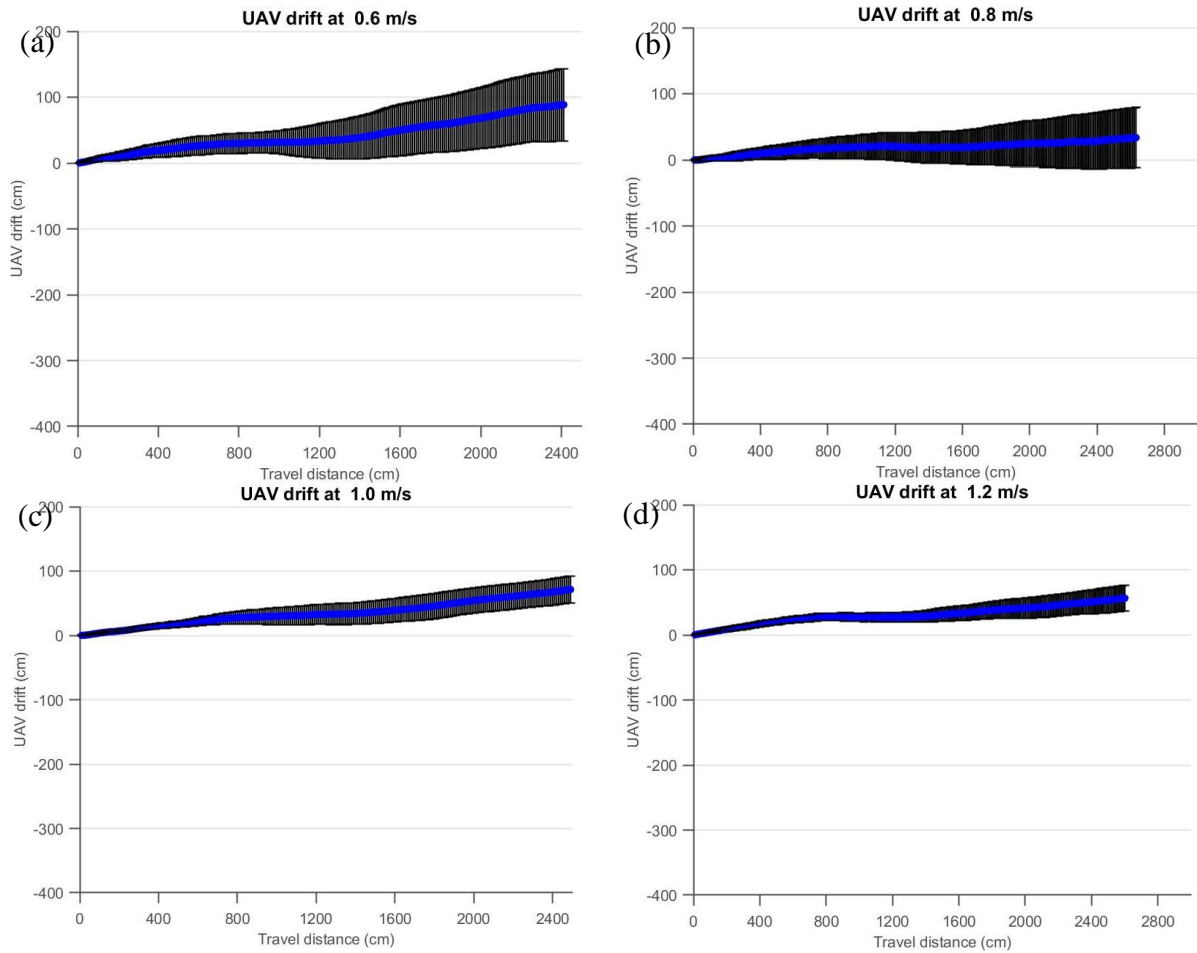
Figure 24. Effect of increasing UAV speed on manual flight performance, while travelling for a fixed distance (2800 cm) along length at four different speeds - (a) 0.6 m/s, (b) 0.8 m/s, (c) 1.0 m/s, and (d) 1.2 m/s.

Similar results were obtained while flying along the width (Figure 25), wherein UAV always drifted left ($y < 0$) of the reference position ($y = 0$), the overall drift was smaller at higher speeds, and deviation also reduced with increasing speed. For manually flown flights (Figure 26), the deviation in flight pattern depended on the agility of the manual pilot. Specifically, for speed 0.8 m/s (Figure 26 (b)) and 1.0 m/s (Figure 26 (c)), due to initial heading error in some replicates, the UAV experienced comparatively higher deviation than the other two speeds. Although overall drift (from reference position) was smaller along the width, this can be attributed to the fact that UAV covered a smaller

106

distance along the width (2200 cm) than length (2800 cm). Consequently, operation time was higher, resulting in a higher error.
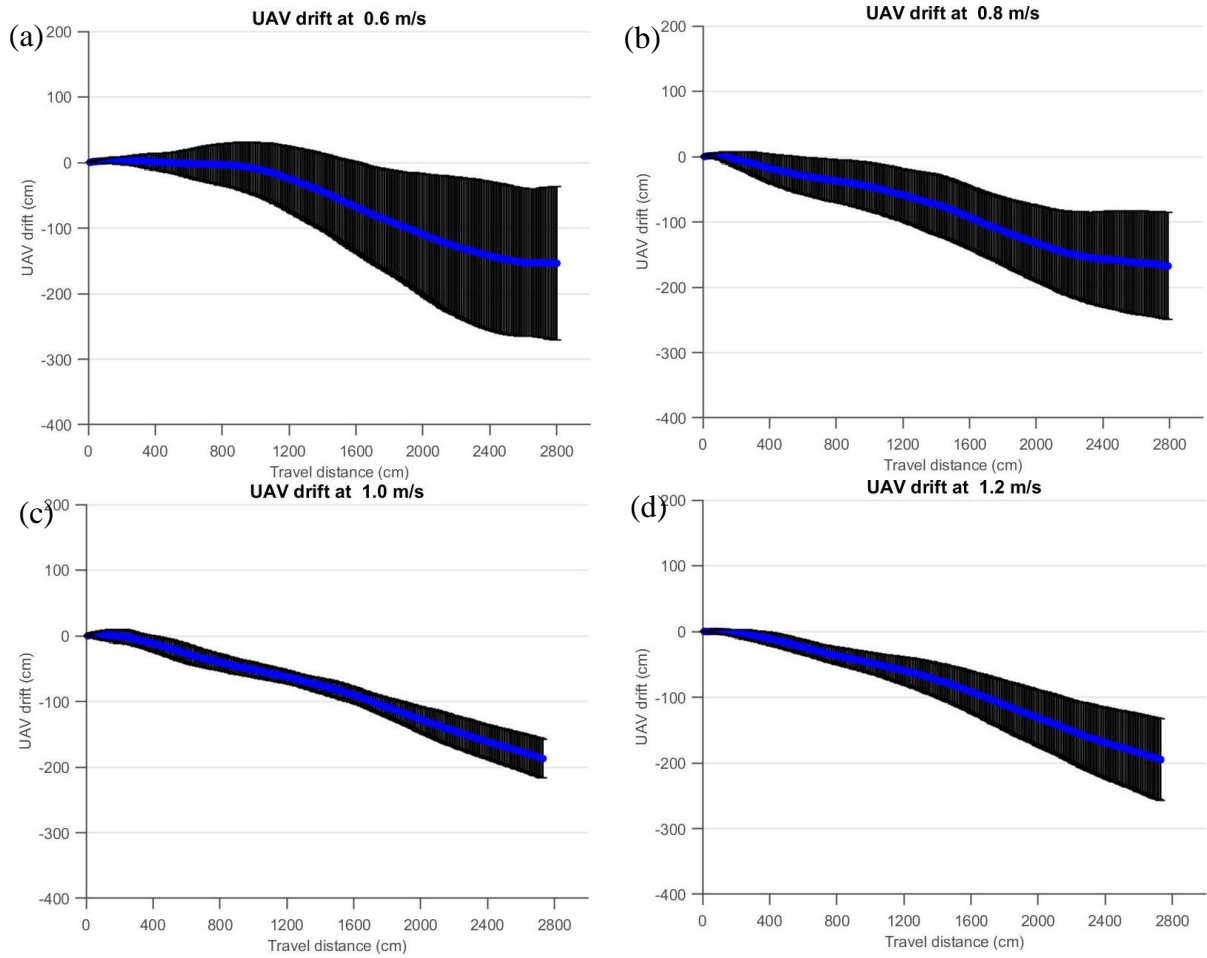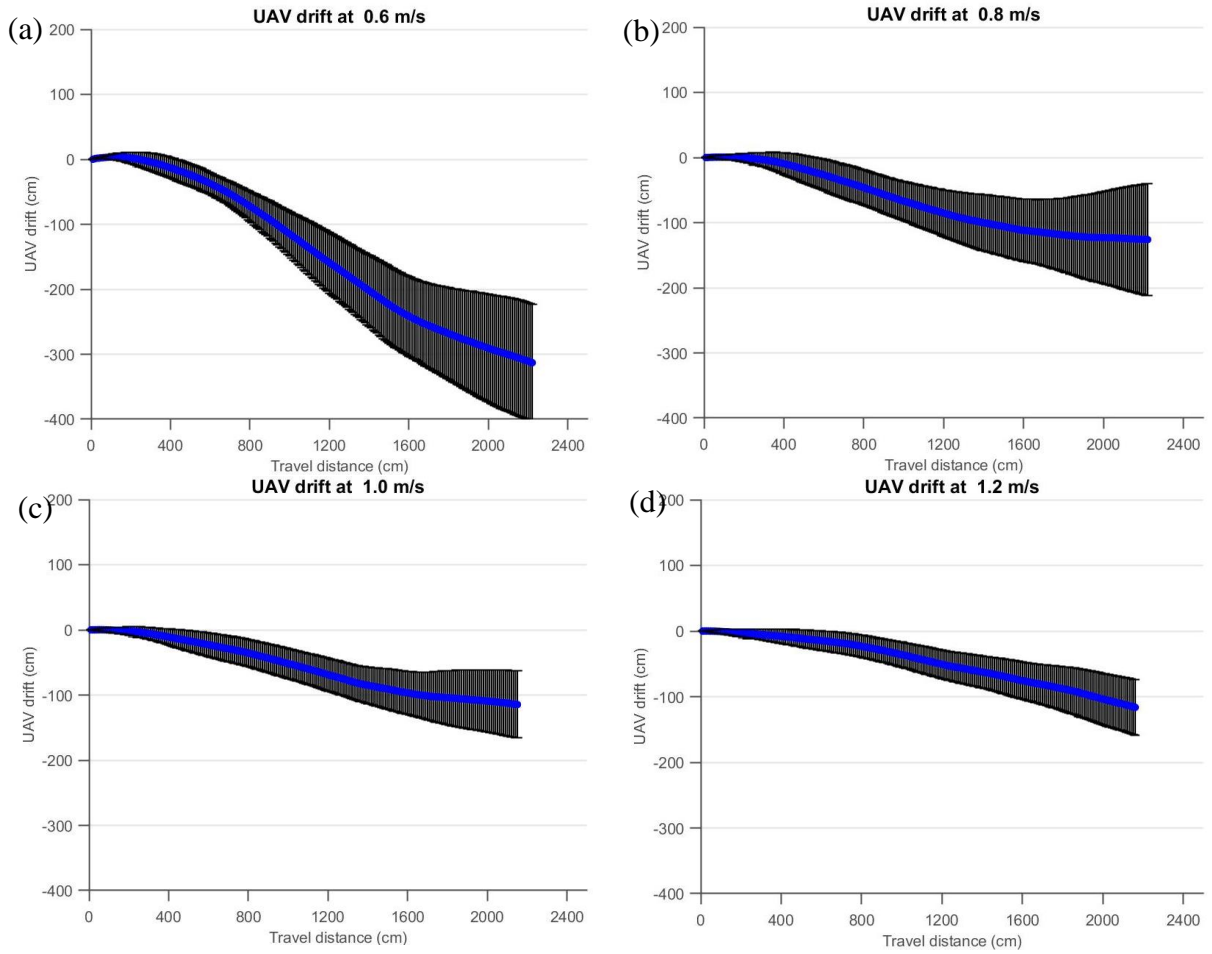

Figure 25. Effect of increasing UAV speed on autonomous navigation performance, while travelling for a fixed distance (2200 cm) along width at four different speeds - (a) 0.6 m/s, (b) 0.8 m/s, (c) 1.0 m/s, and (d) 1.2 m/s
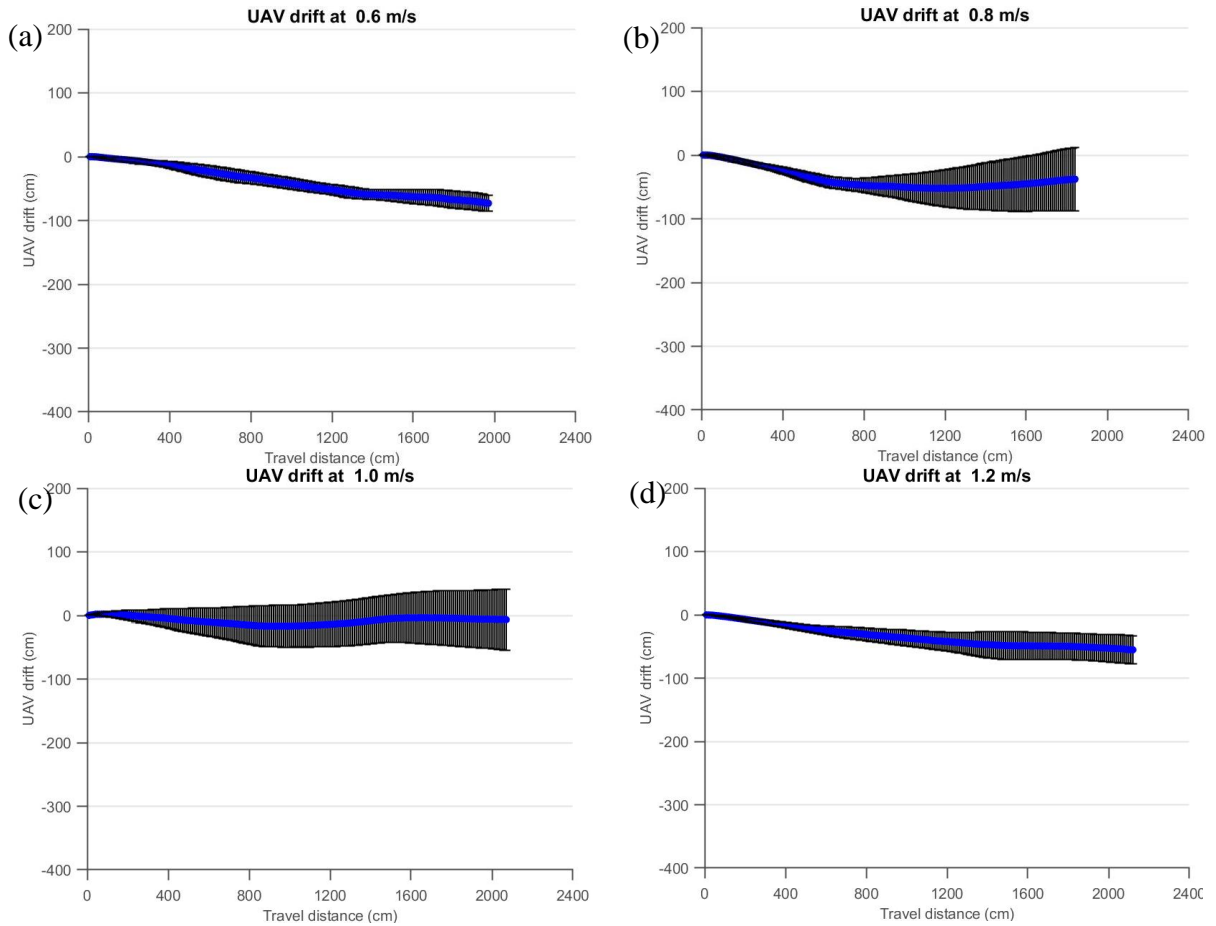
Figure 26. Effect of increasing UAV speed on manual flight performance, while travelling for a fixed distance (2800 cm) along width at four different speeds - (a) 0.6 m/s, (b) 0.8 m/s, (c) 1.0 m/s, and (d) 1.2 m/s.

To further evaluate the flight pattern, a second-order regression was performed on the flight path. The results of which are shown in Figure 27 (while flying along the length) and Figure 28 (while flying along the width). For lengthwise flights, the R^2 was 0.971, 0.986, 0.998, and 0.998 for four respective speeds. Similar results were found while flying along the width with an R^2 of 0.985, 0.981, 0.985, and 0.997 for the four different speeds.
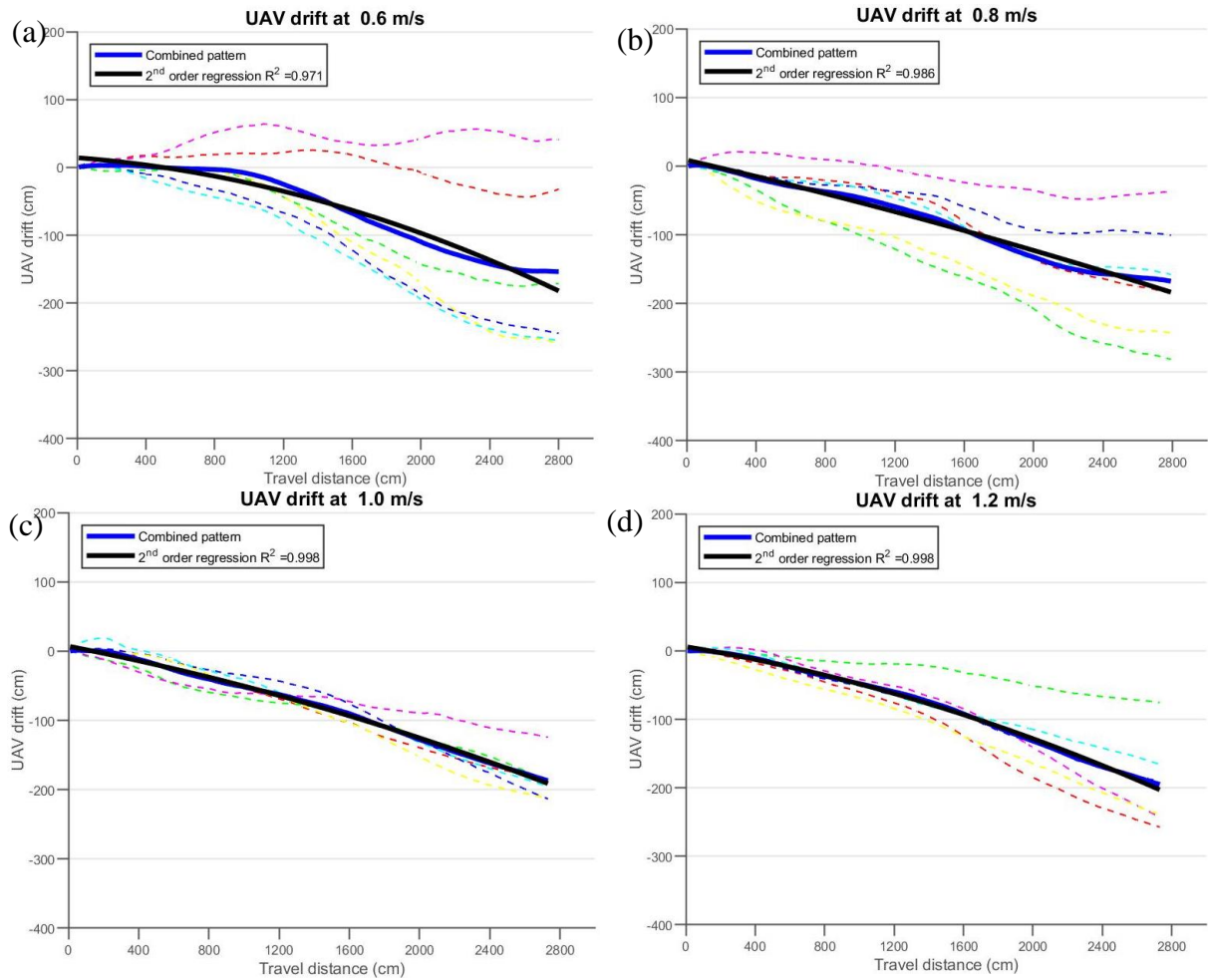
Figure 27. Second order regression model of the autonomous UAV flightpath under different speeds - (a) 0.6 m/s, (b) 0.8 m/s, (c) 1.0 m/s, and (d) 1.2 m/s travelling for a fixed distance (2800 cm) along length.R^2 coefficient of determination the model mentioned in the legend.
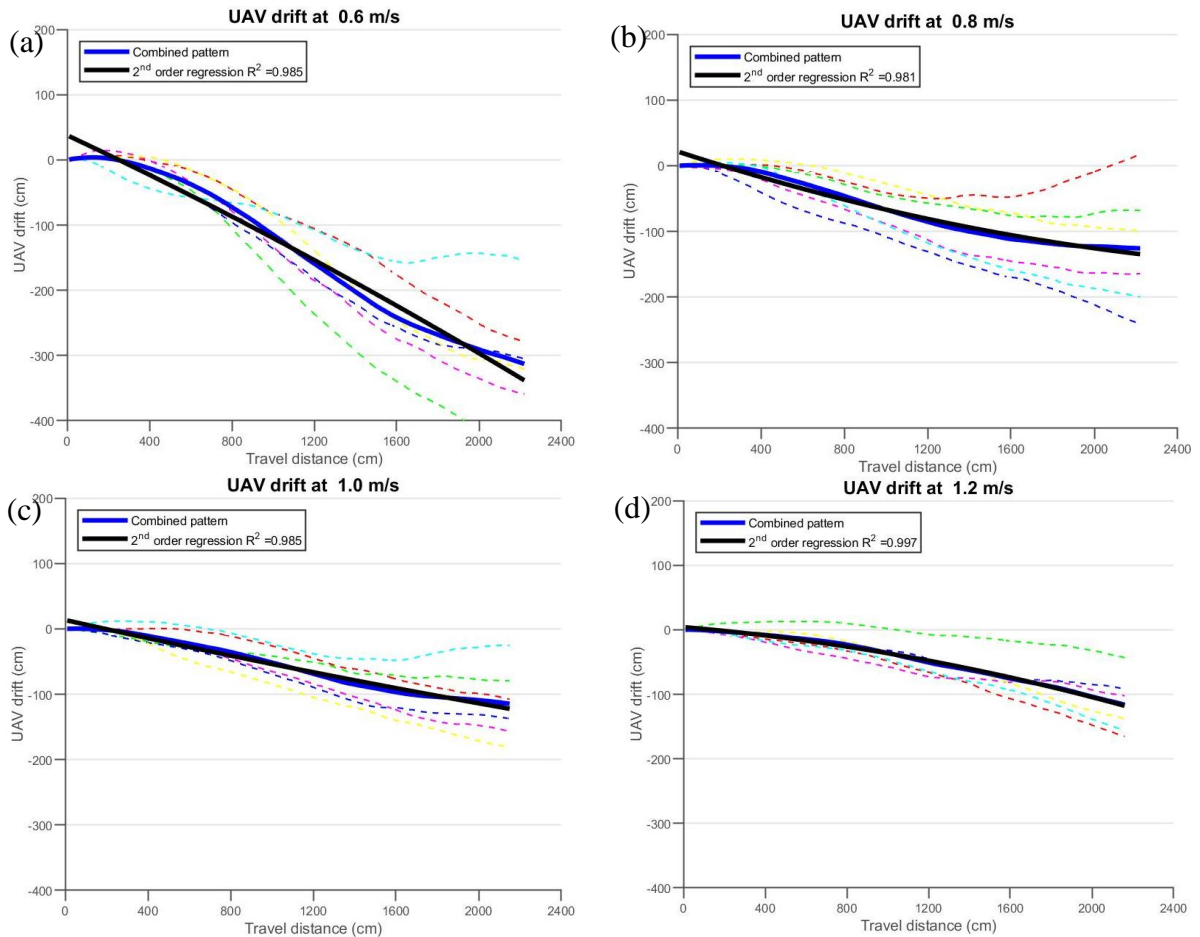
Figure 28. Second order regression model of the autonomous UAV flightpath under different speeds - (a) 0.6 m/s, (b) 0.8 m/s, (c) 1.0 m/s, and (d) 1.2 m/s travelling for a fixed distance (2400 cm) along width.R^2 coefficient of determination the model mentioned in the legend.

4.2.4.3 Flight parameters

Since LiDAR accuracy is affected by platform stability, characterized by variation in speed, UAV orientation, and distance covered, this study analyzed the following flight parameters – (1) distance traveled by the UAV; (2) pitching speed, which is the average speed over the entire distance; (3) yaw orientation; (4) distance covered before reaching the pitching (stable) velocity called accelerated region; (5) variation of UAV heading and velocity within the flight (intra-flight parameters).

110

From Figure 29, it can be observed that for target distance of 2800 cm (along the length) and 2200 cm (along the width), the error in distance traveled was very small for autonomous mode, under 60 cm for both directions. However, deviation increased slightly with increasing speed. For manually controlled flight, since the end of the flight was determined by visual observation and since no real-time feedback for the horizontal distance, the variation in the traveled distance was greater than autonomous flights. Similar to travel distance, error in pitching speed was minimal for manual flights and autonomous flights under all the conditions (Figure 30).

(a)

Deviation in travelled distance along length

(b)

Deviation in travelled distance along width
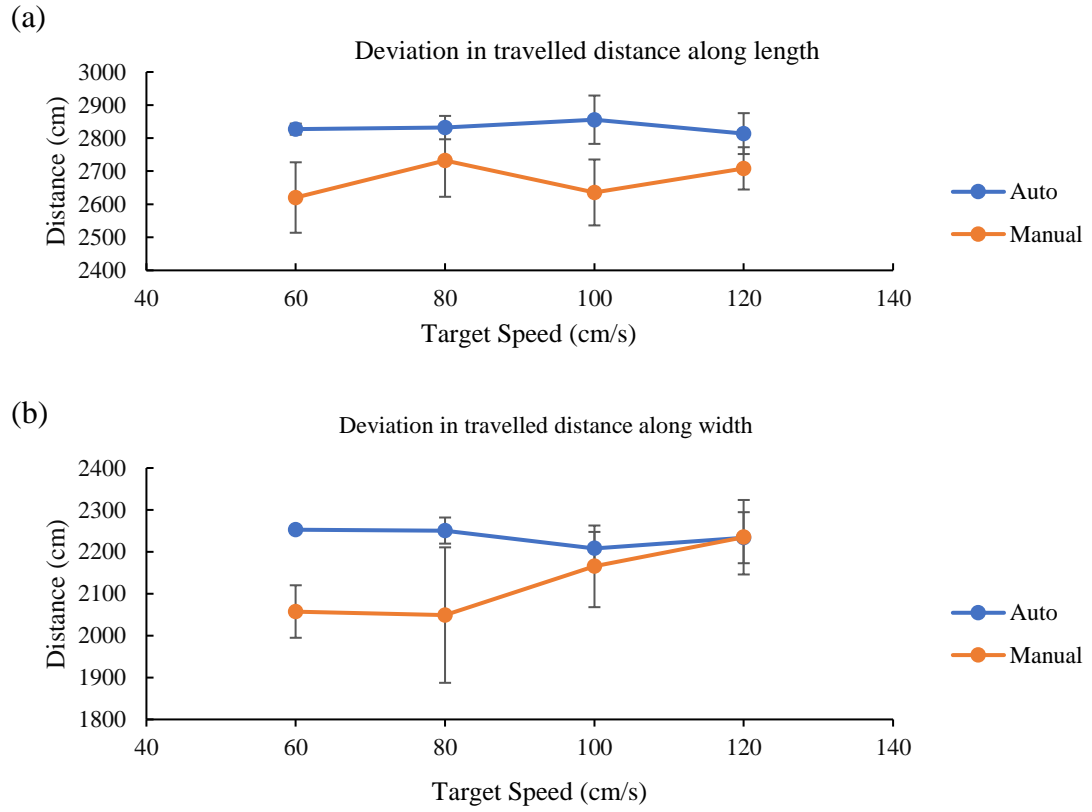
Figure 29. Variation in total distance traveled under different speeds, flight mode, and directions.

(a)

(b)
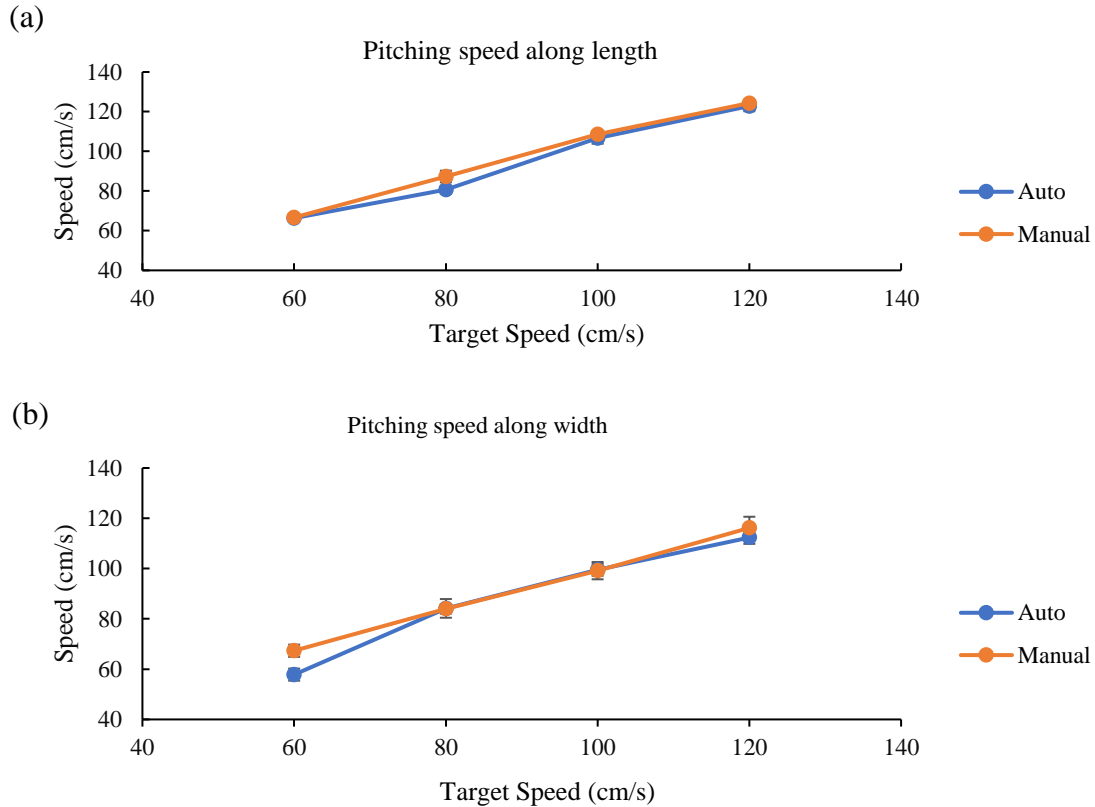
Figure 30. Variation in pitching speed under different speeds, flight mode, and directions.

Figure 31 shows the variation in the accelerated region. For the given target speed, the trend was similar along both directions (length and width) for the autonomous mode, which increased with higher target speeds. Since the UAV required higher time to achieve a higher set speed and the UAV was pitched at a fixed angle (for a given speed), the accelerated region increased with target speeds. However, for manual mode, variation of this parameter depended on the pilot's ability to pitch the UAV to reach the target speed, which can vary from one replication to another; thus, this parameter had greater variation than autonomous mode.

113

(a)

Distance to set velocity along length

(b)

Distance to set velocity along width
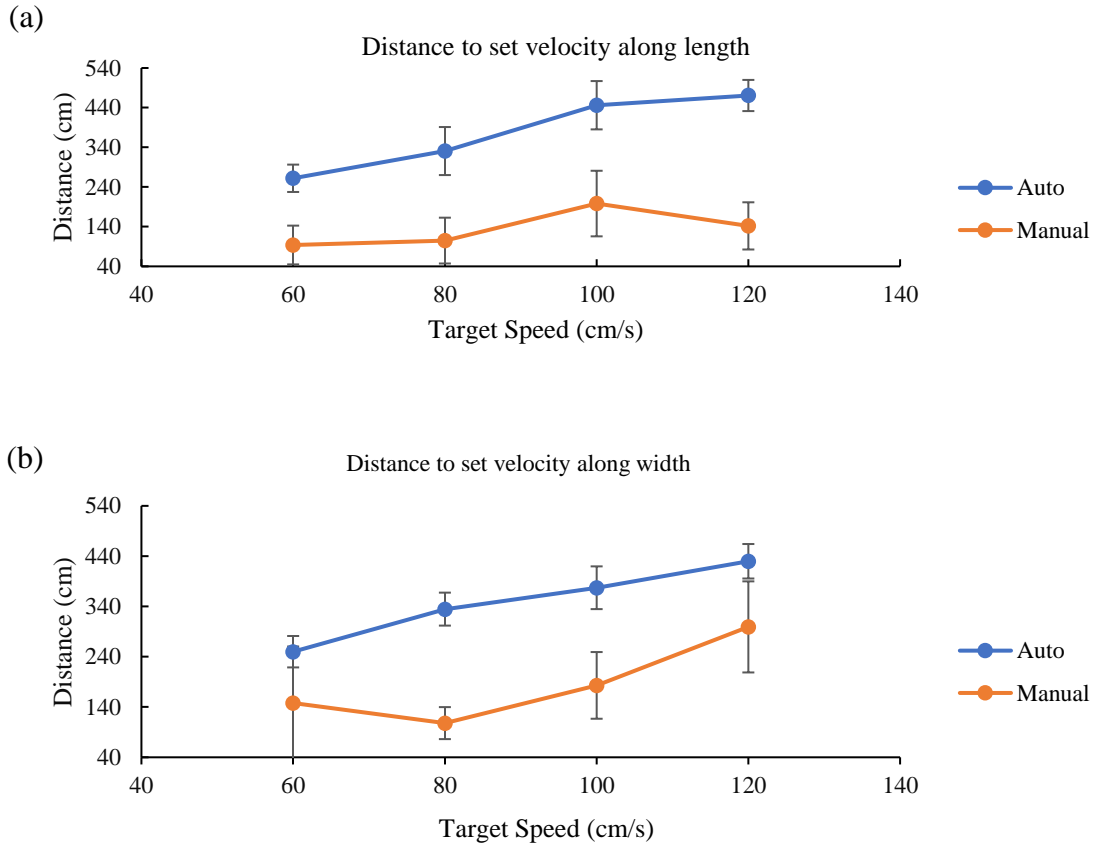
Figure 31. Variation in the distance to set velocity (Dₛ) under different speeds, flight mode, and directions.

As mentioned previously, LiDAR measurement accuracy is affected by its travel speed, and it is desirable to maintain a constant speed while scan data is collected since speed variation can result in variable spacing between adjacent scan lines, reducing the quality of scanned data. Figure 32 shows the variation of speed while the UAV was pitching. The autonomous mode showed a similar decreasing trend in speed variation with increasing target speed, indicating that higher speed resulted in more stable performance. However, the variation was slightly higher along length than width since the UAV traveled a larger distance in the former case, increasing the sample size, which indicates that traveling longer distances can lead to greater speed variation. Even though the speed performance

of manual mode was better in few cases than autonomous mode, it depended on the pilot's skill that can vary from one test to another, which is evident in the results. Additionally, it can have sudden speed variation due to the pilot's negligence. Similar to in-flight speed variation, heading variation also affects the LiDAR performance, and fluctuations in the heading can cause the scan lines to rotate along the z-axis, deteriorating the point cloud quality. Figure 33 shows the variation in UAV heading during travel. For autonomous flight, the variation was negligibly small, which was not affected by travel speed. However, similar to speed performance, the manual mode trend depended on the pilot. In few cases, when the initial heading had an error, it was manually adjusted during the flight resulting in higher error compared to autonomous flights.

(a)

(b)
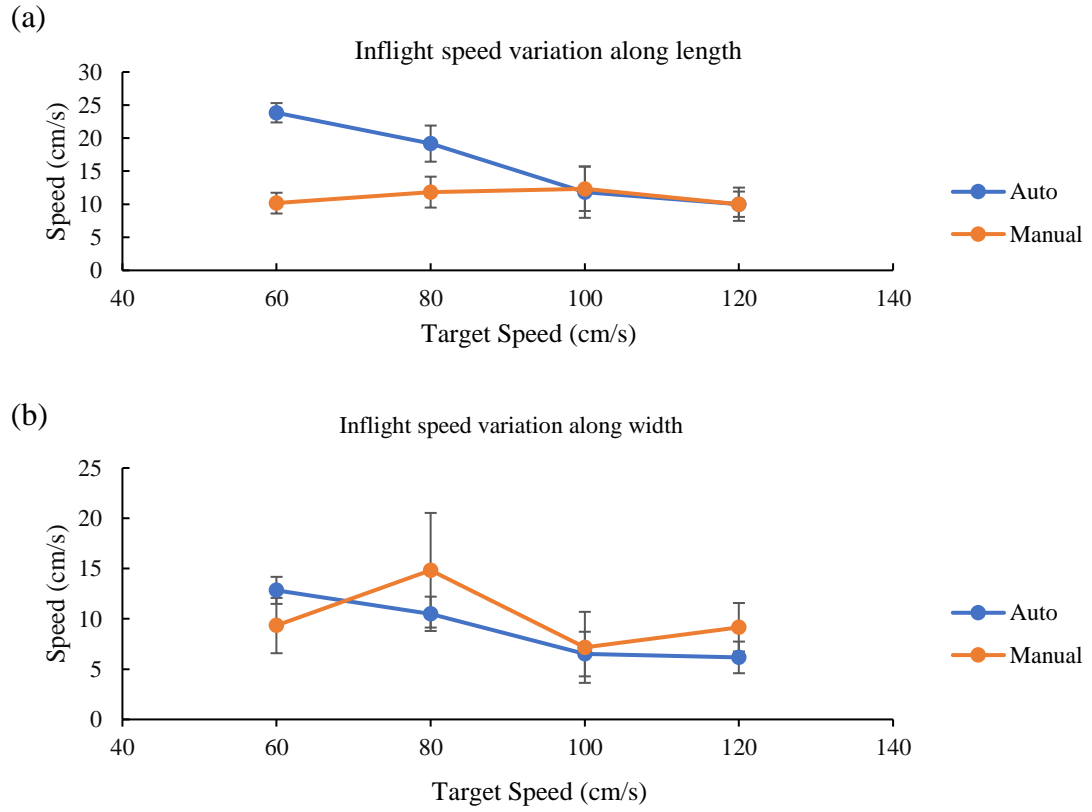
Figure 32. Variation in the pitching speed during flight under different speeds, flight mode, and directions.

(a)

(b)
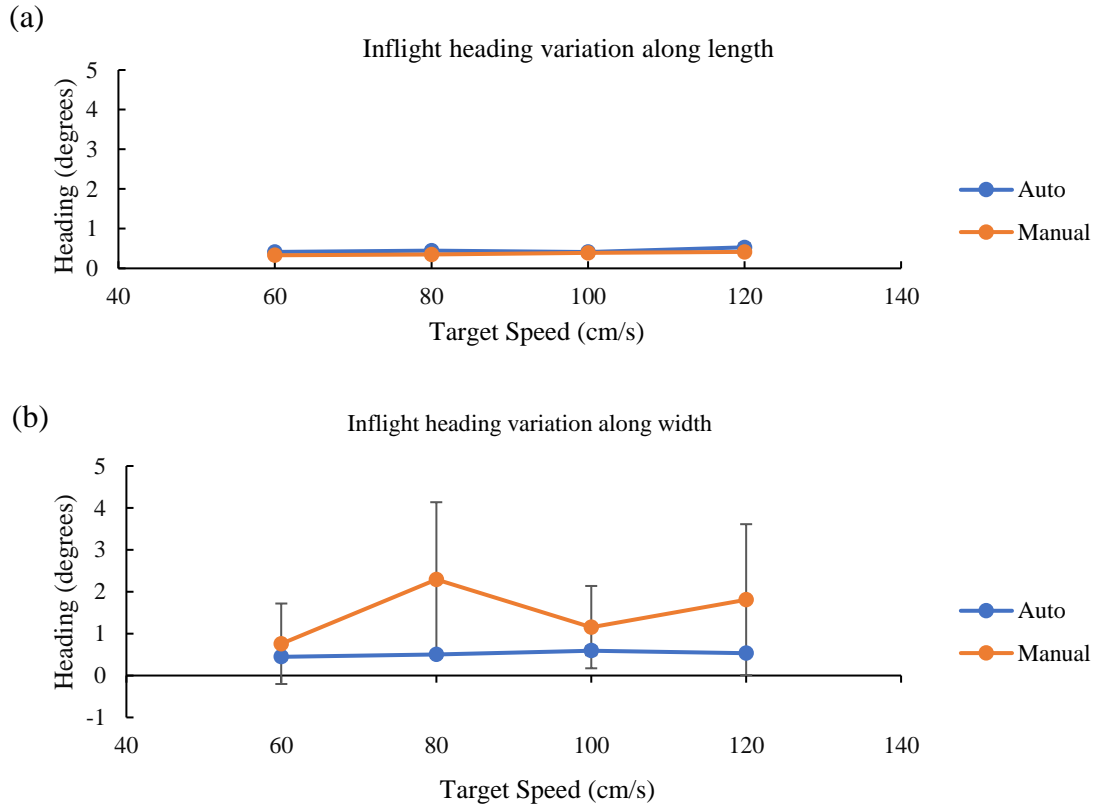
Figure 33. Variation in the UAV heading during flight under different speeds, flight mode, and directions

4.2.5 LiDAR-derived ground height

Figure 34, Figure 35, and Figure 36 show the results of ground height estimation using LiDAR and Guidance. The scales are different for both the senors, which is explained in the next paragraph. As evident from the results, the LiDAR-derived height was accurate, and measurements were not affected by increasing speeds. However, in all three cases, the LiDAR height was slightly (< 1cm) lower from 400 cm to 450 cm (along the travel direction). It was the region where the speed track was decelerating to stop; consequently, the platform was slightly unstable, and LiDAR recorded those heights. Table 11 shows the combined mean and standard deviation over the entire travel distance. This indicates

that LiDAR-derived ground height was reliable as a reference for evaluating the altitude control of the UAV.

The Guidance uses barometric data for height calculation, and every time the system is started, it takes the current height as a reference to calculate height variation. According to the supplier (DJI), the reference height is always set to zero. Since the sensing platform carrying the Guidance was mounted at a fixed height of 130 cm, which was never changed, the output height varied near zero. Consequently, the scales were different from LiDAR measurements. However, the variation in Guidance-derived height was relatively greater, ranging from 7 cm to 9 cm (Table 11). Further tests were conducted to evaluate the performance of Guidance-based and LiDAR-based altitude controls. This experiment suggested that LiDAR height could be considered as a reference for performance evaluation of Guidance's altitude control. Additionally, the height of the speed track was manually measured using a laser tape measure (GLM40, Bosch, Germany) at five different locations along the length, and it was found that the height of the last segment was beginning to drop slightly (1.772, 1.770, 1.772, 1.772, 1.769 m – they are not LiDAR mounting heights). Consequently, LiDAR also showed a drop in height in the last segment.
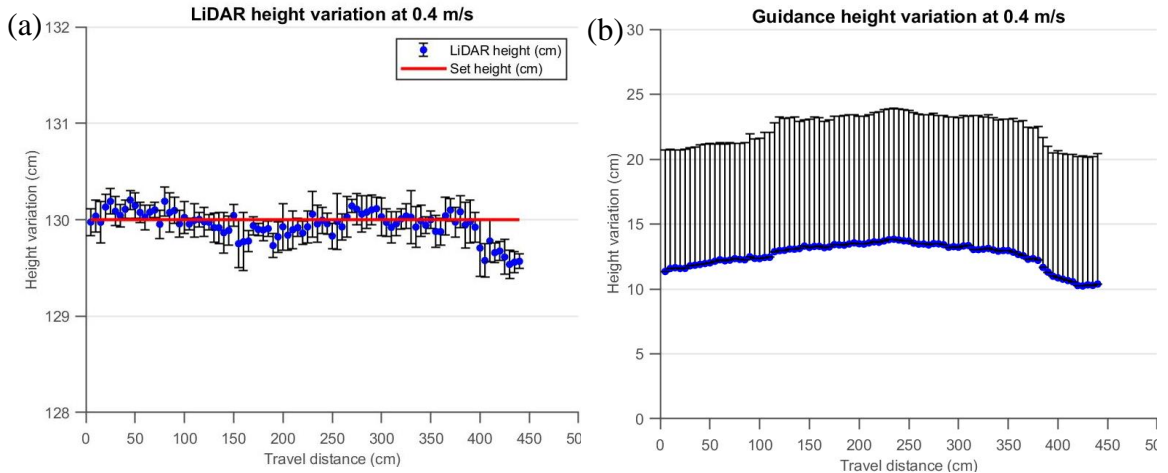
Figure 34. Variation of (a) LiDAR height and (b) Guidance height while traveling at 0.4 m/s.
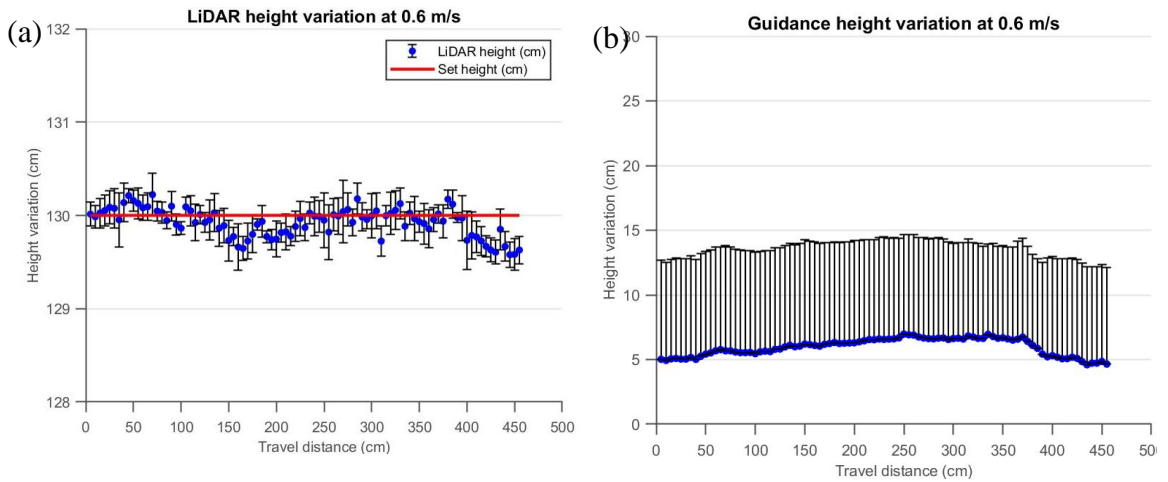
Figure 35. Variation of (a) LiDAR height and (b) Guidance height while traveling at 0.6 m/s.
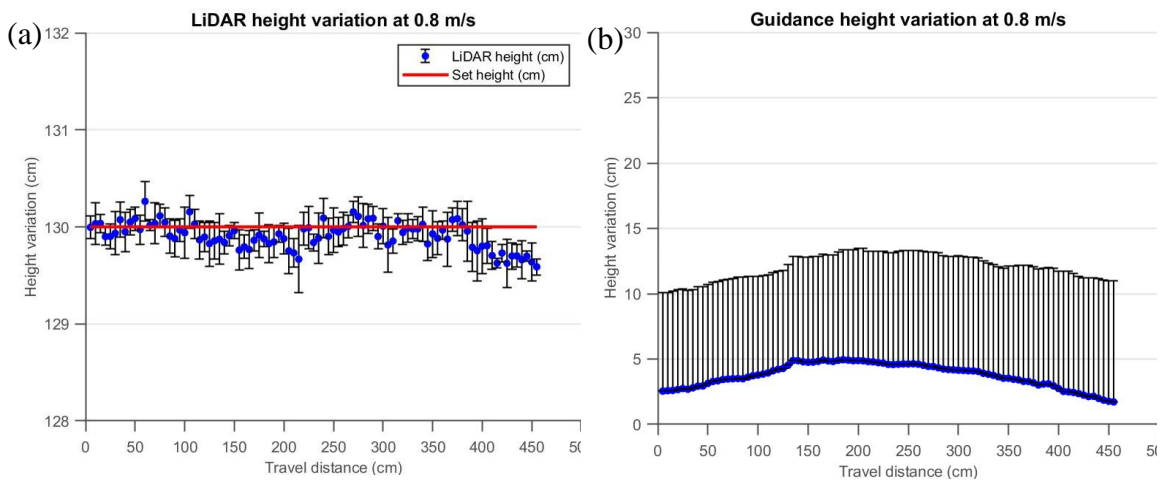
Figure 36. Variation of (a) LiDAR height and (b) Guidance height while traveling at 0.8 m/s.

119

Table 11. Variation in measurements of ground height using LiDAR (L) and Guidance (G) while traveling at
the height of 130 cm and three different speeds.

Speed (m/s)	Source	Mean (SD) (cm)
0.4	L	130 (0.2)
	G	13 (9.0)
0.6	L	130 (0.2)
	G	6 (7.1)
0.8	L	130 (0.2)
	G	4 (7.7)

4.2.6 Altitude control

The UAV was flown at three different heights (2.8, 2.3, and 1.8 m) for a fixed speed (0.6

m/s) and a travel distance (20 m). Six replications of each were taken, and Guidance

height and LiDAR-derived height were recorded, resulting in 36 datasets. Two

parameters were analyzed: (a) initial and final offset and (b) the variation in altitude

during the flight to determine which sensor had better performance for UAV altitude

control. The initial and final offsets, the difference in initial corresponding measured

UAV altitudes (Guidance derived altitude for Guidance-based control and LiDAR-

derived altitude for LiDAR-based control), and target height weres calculated at the

takeoff point and landing point, respectively. Four parameters were reported for both

offsets: maximum, mean, standard deviation (SD), and coefficient of variance (CV) in

percent. All measurements were recorded in centimeters (cm).

From Table 12, it is evident that the maximum initial offset for LiDAR-based control was

lower than that of Guidance-based control in all three flight altitudes. However, looking

at the CV (%), Guidance-based control performance was better at high altitudes (280 cm) than that of LiDAR-based control. Its performance deteriorated at lower altitudes. In other words, LiDAR's performance improved with decreasing altitude, which is more desirable since greenhouses have limited overhead space requiring UAV to fly low. For the final offset, both systems performed best in the case of medium height (230 cm), with the least CV compared to other heights. For low altitude flight, Guidance based control performed better, whereas, for high altitude flight, LiDAR-based control was better.

Table 12. Effect of varying target altitude and input source on the initial and final offset

Input		Initial offset (cm)			Final offset (cm)		
Target height	Input Source	Max	Mean (SD)	CV (%)	Max	Mean (SD)	CV (%)
280	L	7	4 (3)	64	7	3 (2)	77
	G	10	7 (2)	27	35	7 (11)	161
230	L	8	4 (2)	58	6	3 (2)	50
	G	21	10 (7)	74	9	7 (2)	30
180	L	8	6 (2)	33	18	8 (8)	102
	G	14	5 (5)	85	12	7 (3)	37

To evaluate variation during entire flight, flight data were binned at every 50 cm, and height from both sensors was recorded. The mean and standard deviation among the replicates were reported for three different target altitudes for both the control modes. Table 13 shows the overall mean and standard deviation while flying for 2000 cm at three mentioned heights. The table also includes the mean offset in Guidance height

121

measurement compared to LiDAR. For evaluation of LiDAR-based control, LiDAR height was considered, and for Guidance-based control, Guidance height was considered. Comparing the results for target height of 280 cm for LiDAR-based and Guidance-based control (Figure 37 (a) and (b)) show that for deviation for LiDAR-based control (error bars shown in black) was very low throughout the entire flight. Although for Guidance-based control, the deviations were low before 1400 cm (error bars shown in black), the deviations and offset from set height were relatively greater beyond 1400 cm. The UAV height stayed above the set height in both the cases and overall height and deviation for both systems were comparable, which were 283(2) cm and 285(5) cm for LiDAR-based and Guidance-based control, respectively. Similarly, for the 230 cm target height (Figure 38 (a) and (b)), the UAV height was always above the set height, and Guidance-based control had a slightly higher offset and deviation (237 (5) cm) than LiDAR-based control (233 (2) cm). The results of altitude control at 180 cm had a similar performance for both systems (Figure 39 (a) and (b)), wherein the UAV remained above the set altitude with small deviations; overall UAV altitudes were 186(5) cm and 185(4) cm for LiDAR-based and Guidance-based control, respectively. The deviations in UAV altitude were due to a high threshold (20 cm); consequently, whenever the UAV lost the altitude below the threshold, it was given an upthrust (0.1 m/s). Reducing this threshold can reduce the altitude variation during flight. Performance of both the controls was comparable with the overall offset under 6 cm and 7 cm with LiDAR-based and Guidance-based control, respectively.

Figure 37. Variation of UAV altitude flying at 280 cm using (a) LiDAR feedback and (b) Guidance feedback. The figure shows the mean height and deviation among 6 replicates extracted at every 10 cm, and both Guidance height and LiDAR measured heights are reported with their deviations (error bars).
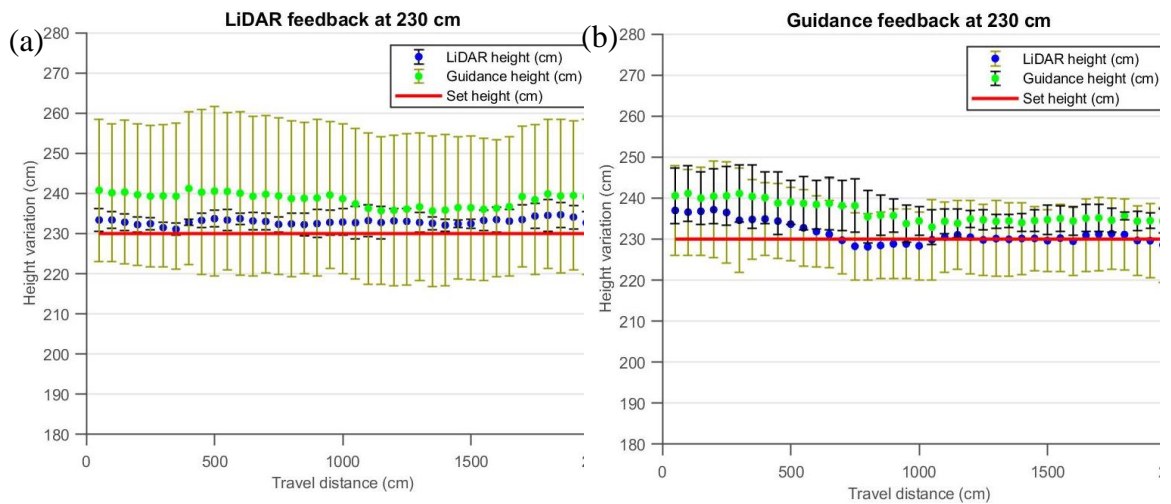
Figure 38. Variation of UAV altitude flying at 230 cm using (a) LiDAR feedback and (b) Guidance feedback. The figure shows the mean height and deviation among 6 replicates extracted at every 10 cm, and both Guidance height and LiDAR measured heights are reported with their deviations (error bars).
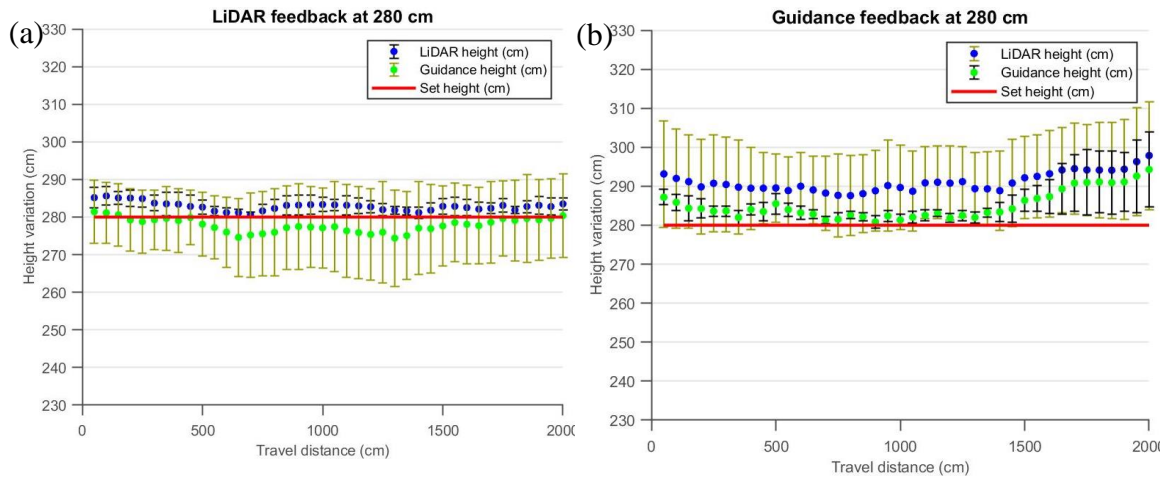
123
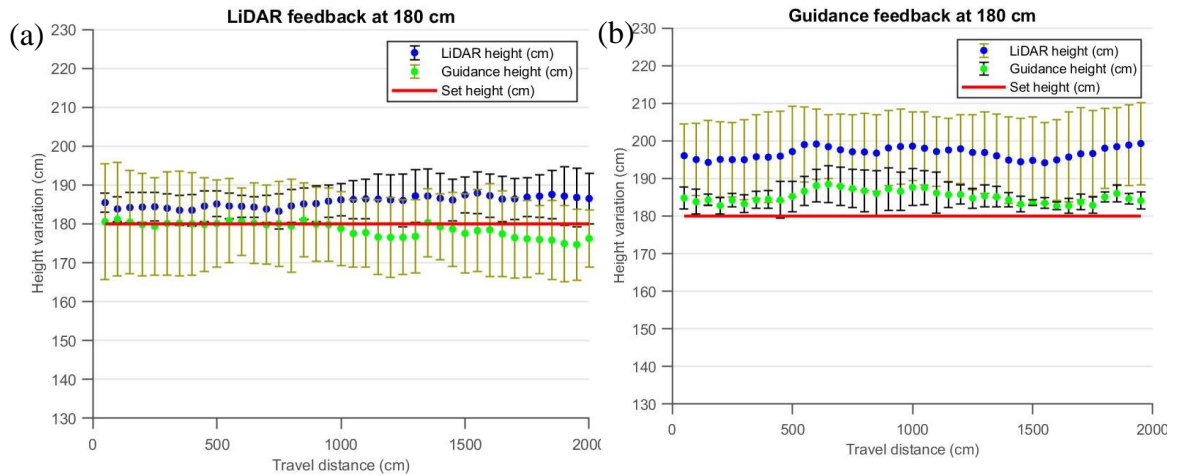
Figure 39. Variation of UAV altitude flying at 180 cm using (a) LiDAR feedback and (b) Guidance feedback. The figure shows the mean height and deviation among 6 replicates extracted at every 10 cm, and both Guidance height and LiDAR measured heights are reported with their deviations (error bars).

Table 13. Comparison of LiDAR (L) and Guidance (G) based altitude control at three target heights (280, 230, and 180 cm). The Guidance derived height was also reported along with LiDAR. The deviations are mentioned in the parenthesis. The range represents the range of height variation of the combined dataset. All measurements are in cm.

Set Height	Control mode	LiDAR height		Guidance height	
		Mean (SD)	Range	Mean (SD)	Range
280	L	283 (2)	5	278 (10)	7
	G	291 (10)	10	285 (5)	13
230	L	233 (2)	4	239 (17)	6
	G	231 (9)	9	237 (5)	8
180	L	186 (5)	5	179 (10)	6
	G	197 (10)	5	185 (4)	6

124

4.3 Downdraft Effect On Plant Measurement

For analysis, plant P2 was selected, and RMSE and variability analysis was conducted for single speed (0.4 m/s) under varying viewing angles (A1 = 0˚, A2 = 20˚, and A3 = 35˚). P2 was chosen because it resulted in more stable results, and the plant shape was more flexible than others (which were more rigid). B2 was chosen for analysis among standard objects because of its rough surface texture than B1, which was more reflective and could deflect the laser beams. With 0˚ mount, the error in height and length measurement of the plant was very small, under 12 mm (excluding the first plant for length). For length measurement, the error was not affected by increasing horizontal distance. However, error in height measurement increased slightly with increasing horizontal distance. Width measurement experienced the highest error reaching 25 mm, and it increased with increasing horizontal distance.

Furthermore, it was expected that standard objects would not get affected by the downdraft. However, measurement error in the width increased with increasing horizontal distance, which was slightly smaller for higher viewing angles; the reason can be attributed to occlusion from the adjacent object along the scanning axis. With a 0º viewing angle, measurement error in height and length was very low and not affected by the horizontal distance. Even so, with higher viewing angles about the pitching axis, the error increased for both height and length.

Using a higher viewing angle decreased the error in width measurement for nearby plants. However, length measurement error increased considerably with a higher viewing

125

angle. Whereas height measurement had a similar error pattern; however, farther plants had slightly less error than nadir scans. The increased error in length with a higher viewing angle can be attributed to a decreased probability of LiDAR hitting the trailing end of the plants (along travel direction); consequently, affecting measurement accuracy along the length. Nevertheless, with the width measurement, the number of LiDAR hits is higher in the first half (along travel direction); consequently, width estimation is better than the 0º angle. Although increasing the viewing angle moved the scanning plane away from the UAV's center, it affected the scanning performance of LiDAR

Figure 40, Figure 41, and Figure 42 show the point cloud data of the same objects under three different viewing angles. The purpose of showing the front and rear view of the same scan is to explain the effect of higher viewing angles on the scan quality. For 0º viewing angle (Figure 40), since the LiDAR scanning plane is vertically downward, both views are symmetrical in terms of the number of points that LiDAR hits in the front and rear of the object. However, with a 20º viewing angle, the scanning plane is inclined forward; consequently, the number of hits on the trailing end of the objects is lower compared to the front end. This effect is more substantial with a 35º viewing angle. This disparity can cause the LiDAR to miss the object trailing end, resulting in higher error.

(a)

Zero Degree Viewing Angle

Plant Height (m)

0.3
0.2
0.1

2

1.5

1

0.5

Scan direction (m)

0

0

0.5

1.5

2

1.5

2.5

Travel direction (m)

Both sides get equal LiDAR hits

(b)

Zero Degree Viewing Angle

Plant Height (m)

0.3
0.2
0.1

0

0.5

1

1.5

2

2.5

Travel direction (m)

0

0.5

1

1.5

2

Scan direction (m)

Figure 40. (a) Front and (b) rear view of the point cloud with 0º viewing angle. The UAV traveled from 0 m to 2.5 m with propellers turned on. The front and rear view of 3rd plant in 3rd row (at 1 m), indicated by red arrows, gets an equal number of hits due to vertically down-looking LiDAR.

(a)

20 Degrees Viewing Angle

Plant Height (m)

Scan direction (m)

Travel direction (m)

Front gets higher number of LiDAR hits

(b)

20 Degrees Viewing Angle

Plant Height (m)

Travel direction (m)

Scan direction (m)

Figure 41. (a) Front and (b) rear view of the point cloud with 20º viewing angle. The UAV traveled from 0 m to 2.5 m with propellers turned on. The front section of 3ʳᵈ plant in 3ʳᵈ row (at 1 m), indicated by red arrows, gets a relatively higher number of hits than the rear section.

128

(a)

35 Degrees Viewing Angle

Plant Height (m)

Scan direction (m)

Travel direction (m)

Front gets much higher LiDAR hits

(b)

35 Degrees Viewing Angle

Plant Height (m)
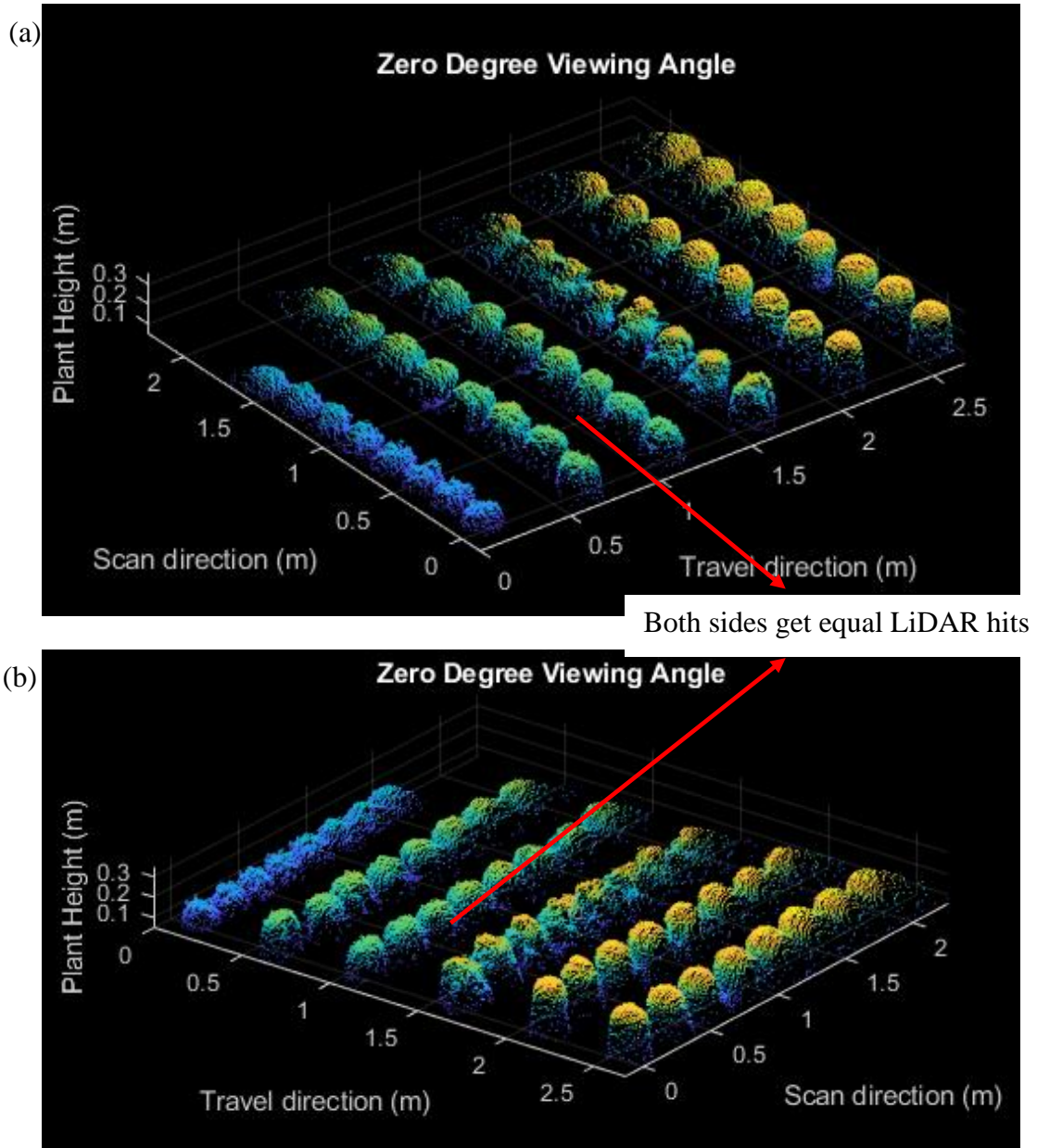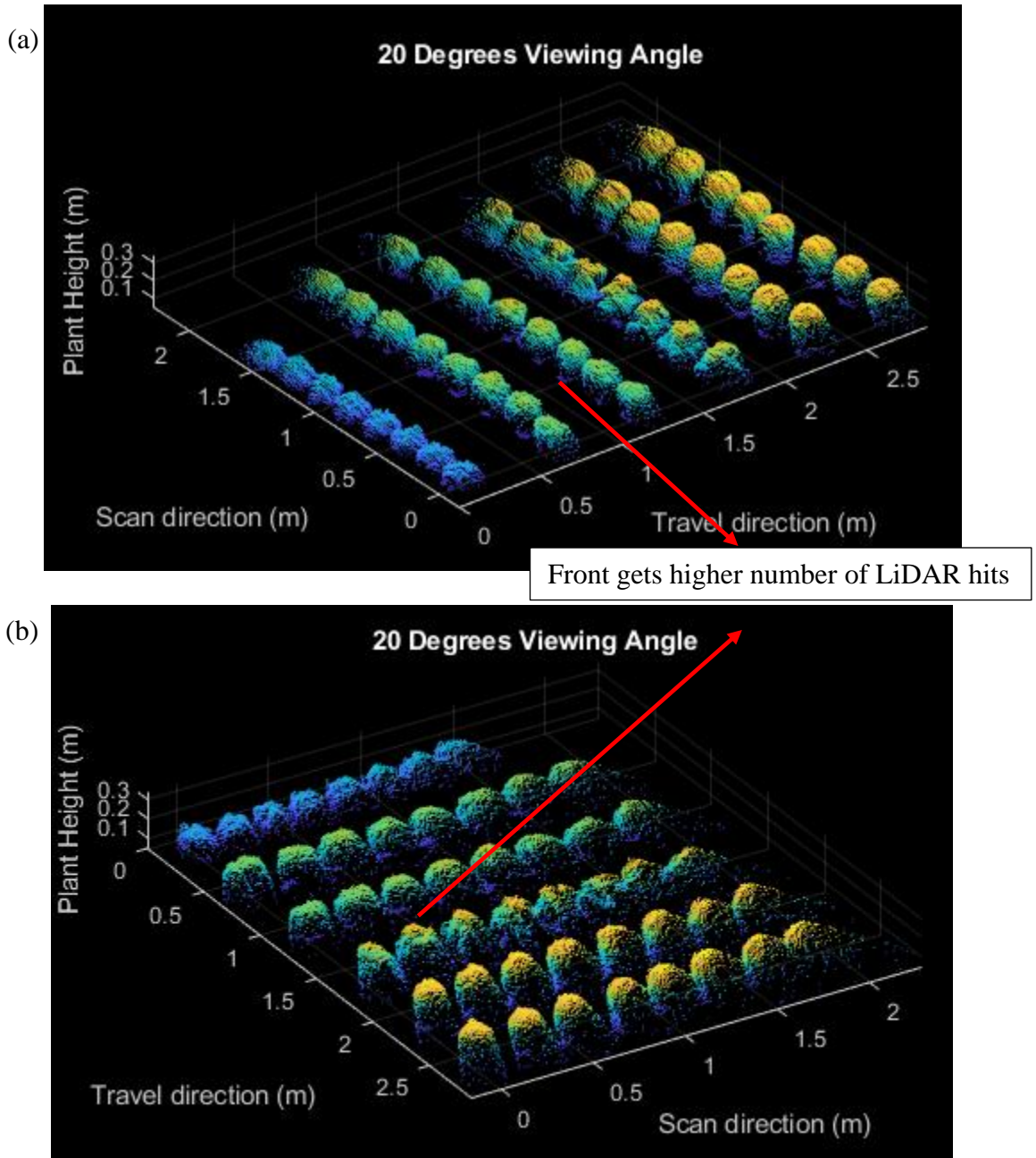
Travel direction (m)

Scan direction (m)

Figure 42. (a) Front and (b) rear view of the point cloud with 35° viewing angle. The UAV traveled from 0 m to 2.5 m with propellers turned on. The front section of 3rd plant in 3rd row (at 1 m), indicated by red arrows, gets a relatively higher number of hits than the rear section.
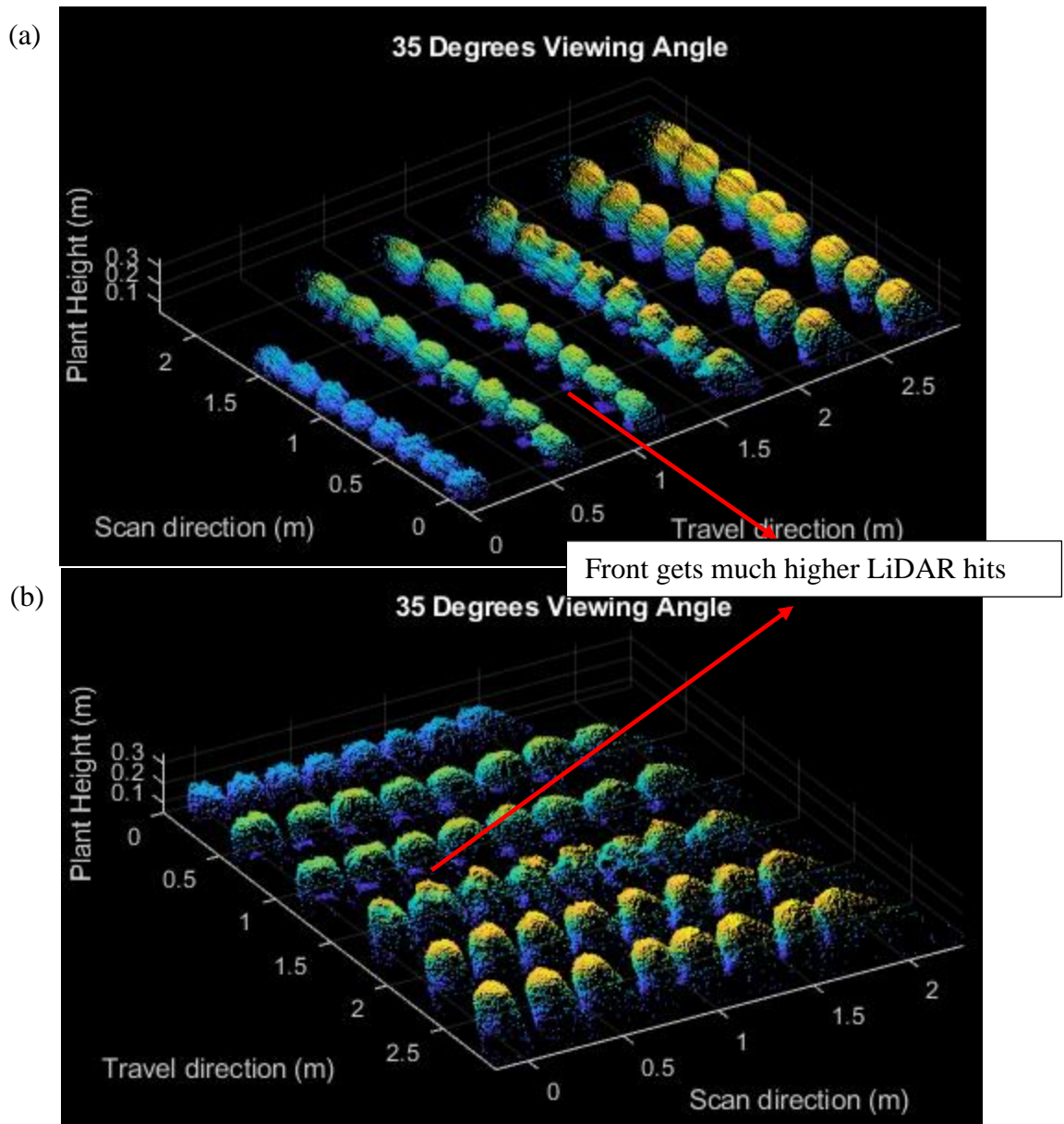
4.3.1 Baseline evaluation

The study used the clustering algorithm (developed by Uchit Nair, work under review) to

extract the plant dimension information. However, it was necessary to evaluate the

performance of the algorithm, which was done by comparing the measurement obtained with the propeller turned to the actual dimensions (manually measured).

From the results of height measurement error (Figure 43), all plants had a similar trend; however, the error magnitude was comparatively higher for plant P1 due to its smaller structure. For the standard objects, B1 had more stable measurements, which could be due to its comparatively less shiny and reflective surface than B2 (Figure 43(b)). However, results of width measurements show that the RMSE in width increased as the horizontal distance from LiDAR increased (Figure 44(a)), reaching a maximum value of 57 mm. In contrast, the pattern was relatively stable for both the standard objects (Figure 44(b)).

Finally, from length measurements (Figure 45), all the plants had similar trends, which were not affected by the horizontal distance; however, they had slightly different magnitudes. P2 and P3, which had a similar structure and relatively lower error due to their broader and homogenous structures, which had a dense distribution of leaves along the boundary, resulted in a lesser chance of LiDAR missing to hit the plant edges. However, P4, which had a tower-like structure with sharp-edged leaves present at the plant boundary, had a greater chance that LiDAR could fail to hit these edges. These errors can reduce if travel speed is low, ensuring denser and closely spaced scan lines. Both the standard objects had a similar error pattern (Figure 45(b)). The experiment showed that the current clustering methodology had stable LiDAR-derived length and height measurements; however, errors in width measurements can be expected due to occlusion, which prevents the LiDAR from viewing the entire plant.
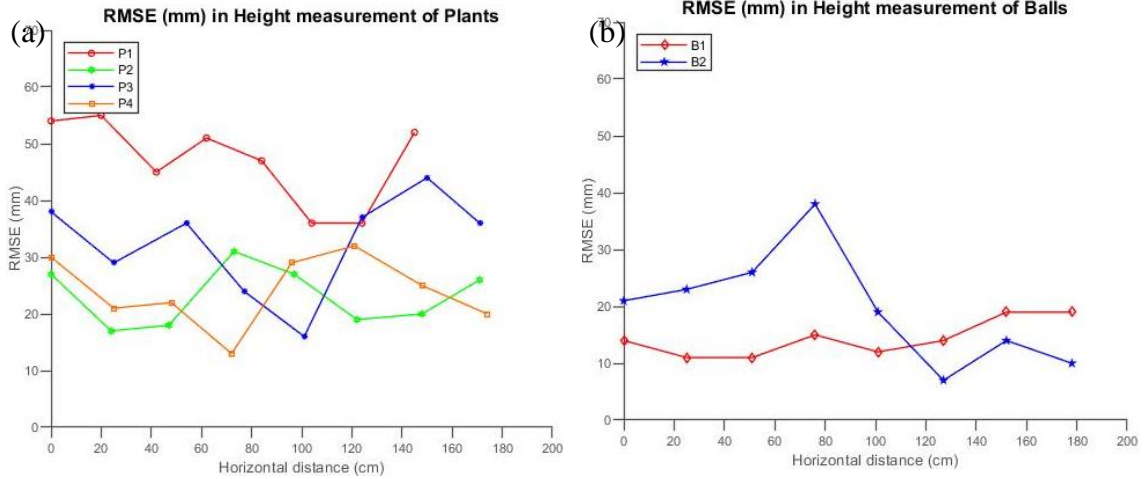
130

Figure 43. Measurement error (RMSE (mm)) in LiDAR-derived heights compared to manual measurements in (a) plants and (b) standard objects.
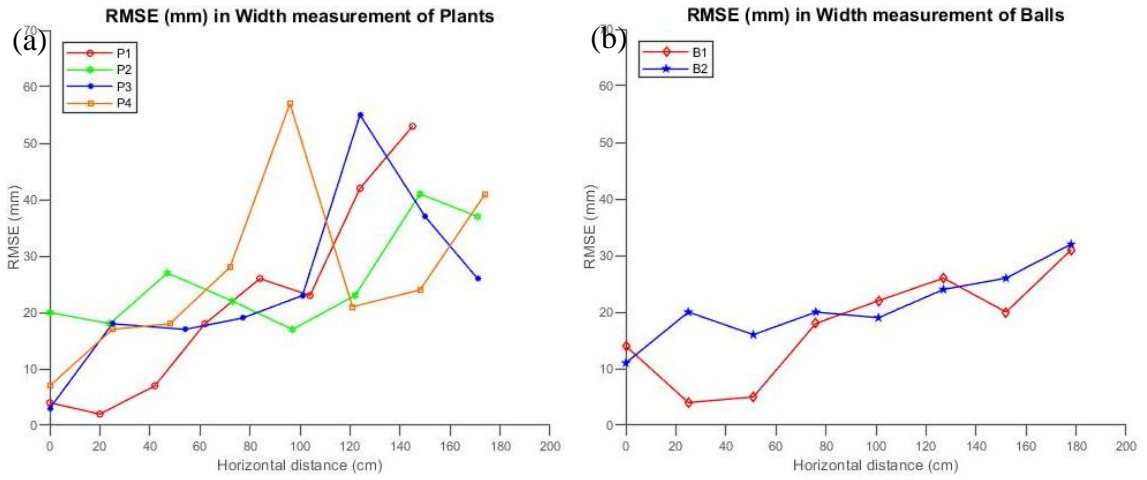

Figure 44. Measurement error (RMSE (mm)) in LiDAR-derived widths compared to manual measurements in (a) plants and (b) standard objects.
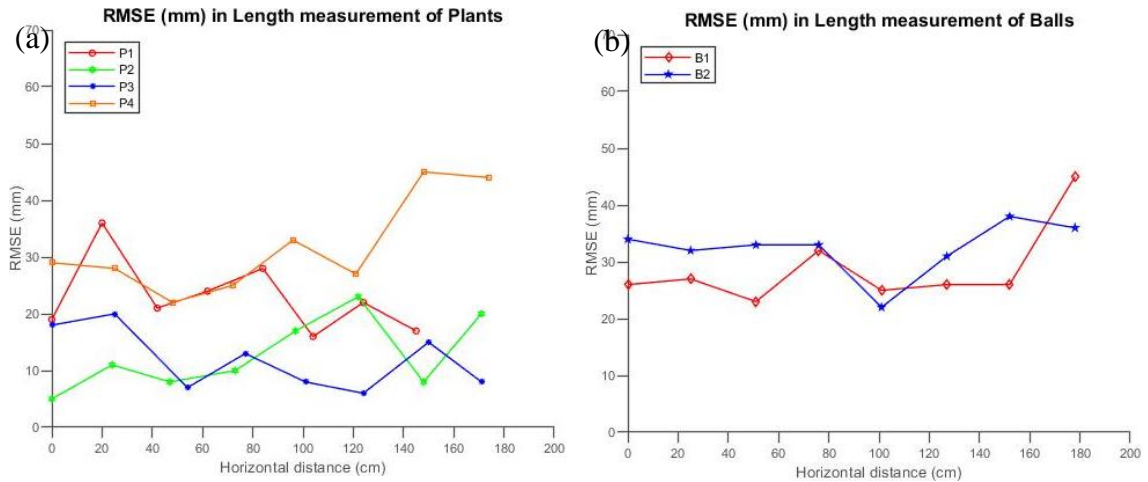
131

Figure 45. Measurement error (RMSE (mm)) in LiDAR-derived lengths compared to manual measurements in (a) plants and (b) standard objects.

4.3.2 Region affected by the downdraft

4.3.2.1 Height

The results of RMSE (Figure 46) in height measurement suggest that the region closer to the UAV (< 40 cm) had a higher error magnitude. Whereas plants farther away (> 50 cm) from UAV's center experienced a lower error. Measurement variation also resulted in similar trends wherein distant plants had a relatively smaller variation than plants closer to the UAV's center. However, P1 (red) showed a sudden rise in error at 120 cm from UAV, which can be explained by its shape and presence of multiple twigs at the top of the canopy, and the clustering algorithm used in this study relies on ordering scanned points from the highest to the lowest point. Due to the presence of multiple high points, the estimation could have varied among the replicates leading to an unexpected error. Both P2 (green) and P3 (blue) had very similar structures, resulting in comparable patterns. Both P2 and P3 were relatively less stiff and compact than the other two plants, and consequently, their shape was expected to be most affected under the downdraft,

132

which was evident from their pattern at 20 cm from UAV. P4 (orange) had a hierarchical

structure with a single leaf at the highest point, and its structure was more rigid than

others; thereby, the algorithm could reproduce a similar structure in each iteration.

Figure 46. (a), (b) Measurement error (RMSE (mm)) and (b), (d) measurement variability (CV (%)) in the height of all plants and standard objects while scanning at a fixed height (1.3 m), speed (0.4 m/s) and viewing angle (0˚).

4.3.2.2 Width

Error in width measurements (Figure 47) for plants showed an increasing trend with

horizontal distance from UAV, and a similar trend was observed for standard objects.

The results did not reflect any particular region affected and the error was more

133

homogeneous (except for the plant P2 and P4 at the end of the row). The P4 (orange) had comparatively higher error than the rest of the plants due to its height and tower-like shape, unlike other plants with a wider top surface area. Specifically, for taller structures, the LiDAR can capture one-half (visible portion) of the canopy (along the width); however, the other half is occluded, leading to poorer width estimations. Moreover, taller plants have a higher probability of getting delinated from there rest state structure than shorter and broader plants, such as P1(red). P2 and P3 also had broader structures; however, as mentioned before, due to their tangible structure, they experience slightly higher errors than P1.
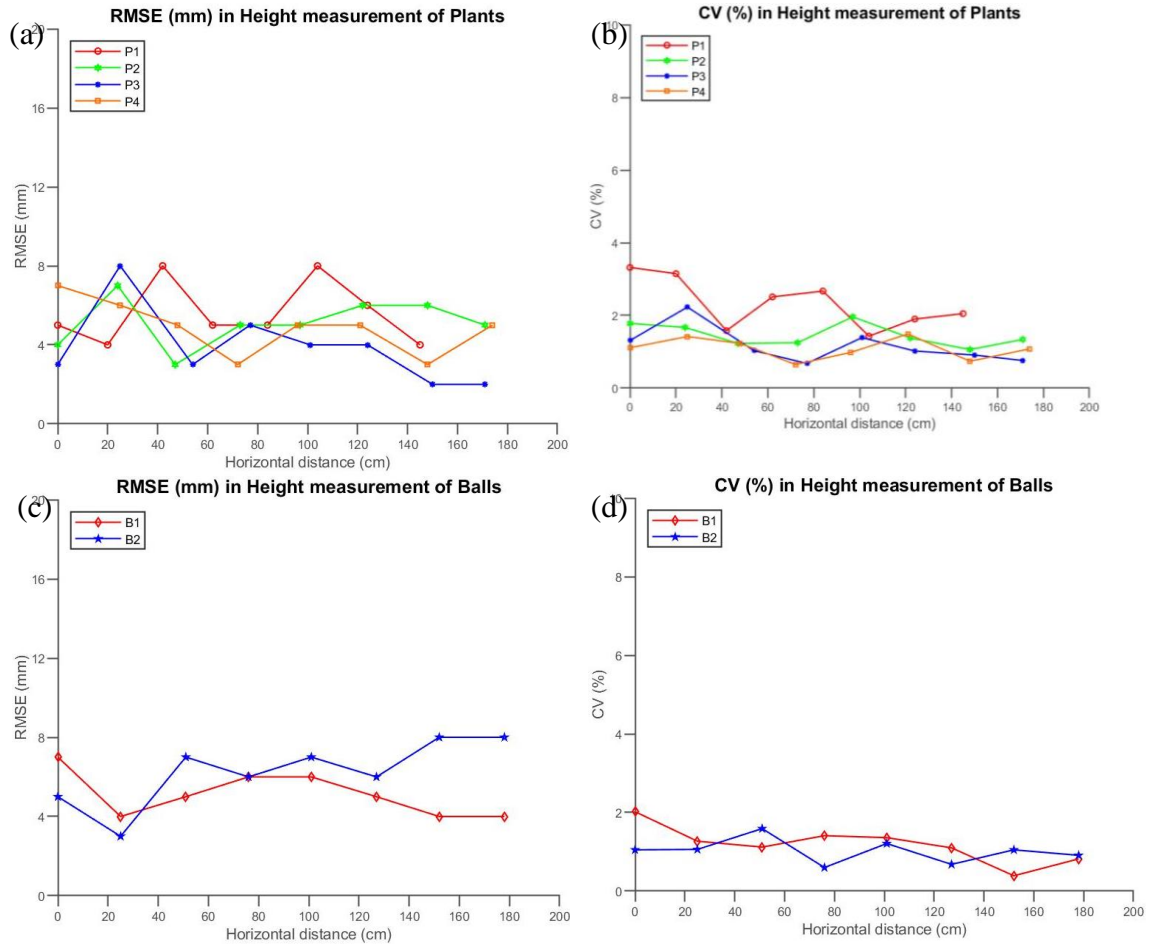
Figure 47. (a), (b) Measurement error (RMSE (mm)) and (b), (d) measurement variability (CV (%)) in the width of all plants and standard objects while scanning at a fixed height (1.3 m), speed (0.4 m/s) and viewing angle (0˚).

4.3.2.3 Length

From the results of length measurement (Figure 48), it can be observed that measurements were stable (RMSE < 24 mm) throughout the entire distance from the UAV, excluding P1 at 120 cm, which experienced a sudden rise in error. The results suggested that length measurements were not greatly affected by the downdraft.
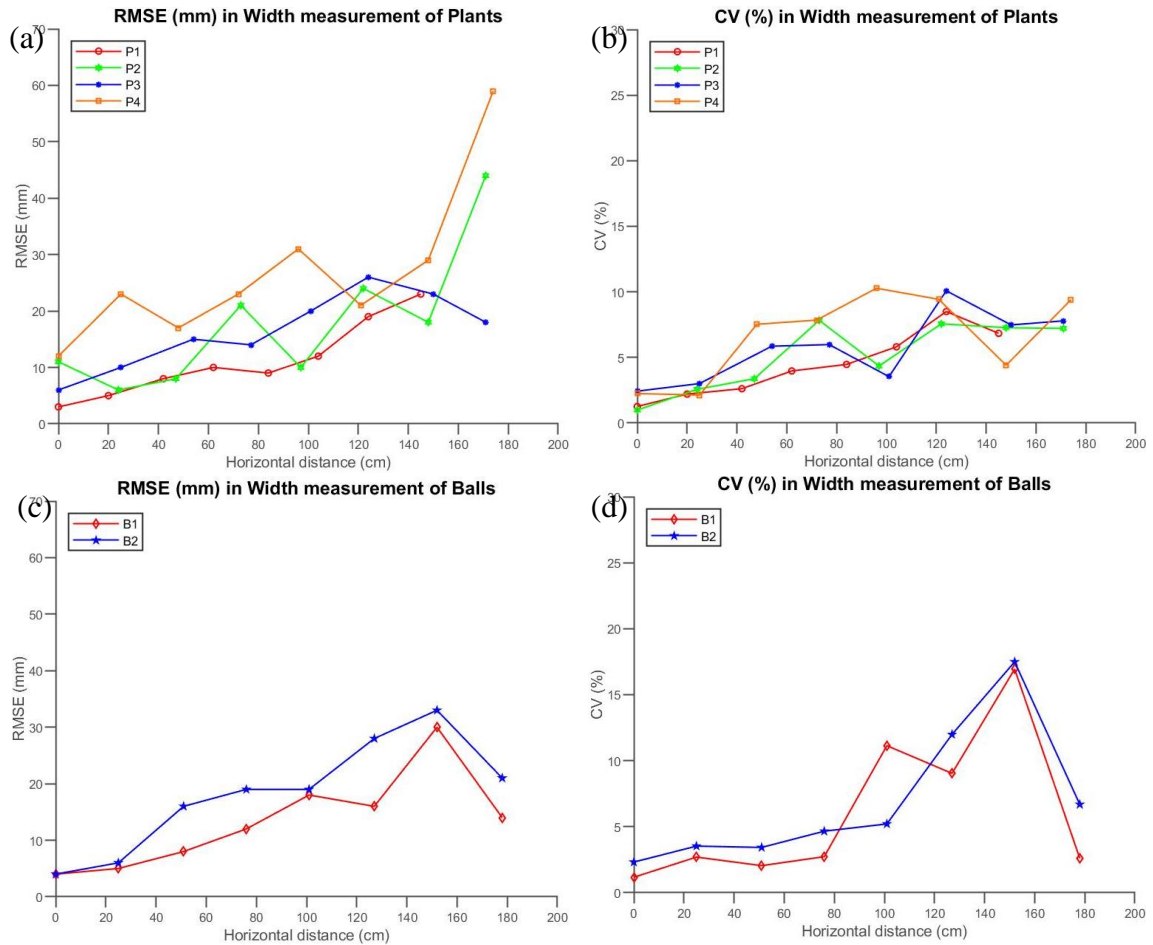
135

Figure 48. (a), (b) Measurement error (RMSE (mm)) and (b), (d) measurement variability (CV (%)) in the length of all plants and standard objects while scanning at a fixed height (1.3 m), speed (0.4 m/s) and viewing angle (0˚).

From the above results of height and length measurements, it can be concluded that the region with 40 cm of the UAV center was affected by the downdraft, and the region beyond 50 cm had stable measurements. Consequently, excluding this region from measurements can reduce the effect of downdraft on measurement. However, the next section evaluates the effect of different viewing angles on the measurement of plant P2, and its purpose was to identify whether higher viewing angles could reduce the downdraft impact.

136

4.3.3 Effect of viewing angle

4.3.3.1 Plant height

The effect of downdraft on the plant height measurement (Figure 49(a)) was very low with the 0º viewing angle, and error was relatively stable beyond 50 cm. Increased viewing angle resulted in slightly higher errors, and it also increased with increasing horizontal distance. The measurement variation (Figure 49 (b)) in plant height was very stable with 0º angle (under 2%) and was not affected by increasing horizontal distance. Furthermore, higher viewing angles did not reduce the variability in measurements. The error was slightly higher for the standard object (Figure 49 (c)) than in the plant and within 8 mm, which was not affected by increasing horizontal distance. However, higher viewing angles resulted in increasing error with increasing horizontal distance. Nevertheless, the variability in measurement Figure 49(d)) was very low with 0º viewing angle (under 1.5%). Similar to the plant measurements, variability increased slightly with higher viewing angles.
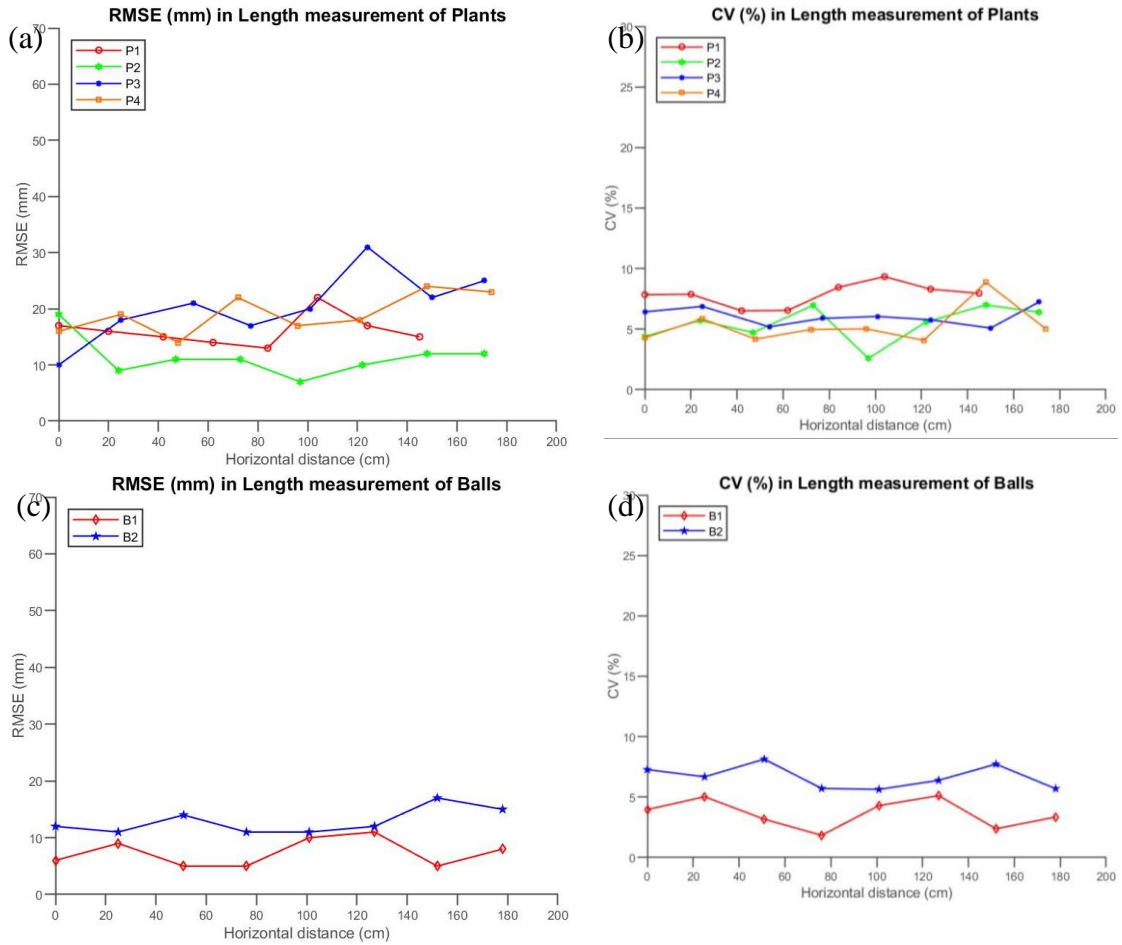
Figure 49. (a), (c) Measurement error (RMSE (mm)) and (b), (d) measurement variability (CV (%)) in the height of plant and ball while scanning at a fixed height (1.3 m), speed (0.4 m/s) and three different viewing angles (0˚, 20˚, and 35˚).

4.3.3.2 Plant width

For 0˚ viewing angle, the error in measuring plant width (Figure 50(a)) was low within 50 cm of the UAV (under 10 mm); however, it showed a sudden increase in error in the range of 70-100 cm from the UAV. The findings indicate that downdraft impact was relatively greater in this range. Using a higher viewing angle (35º) resulted in the least error for nearby plants (within 100 cm of the UAV). Moreover, the measurement variability (Figure 50 (b)) was also minimum and stable with the 35º viewing angle

138

(under 4.2%) excluding the last plant. The last object in the row can result in unexpected high errors since the clustering algorithm is susceptible to picking sparse points. This effect is even greater with a higher viewing angle (as shown in the point cloud data) However, the error in the standard object (Figure 50(c)) showed an increasing pattern with horizontal distance from UAV with 0° angle. The measurement variation (Figure 50 (c)) had a similar pattern as plants, which was most stable with a 35° angle (under 7%).

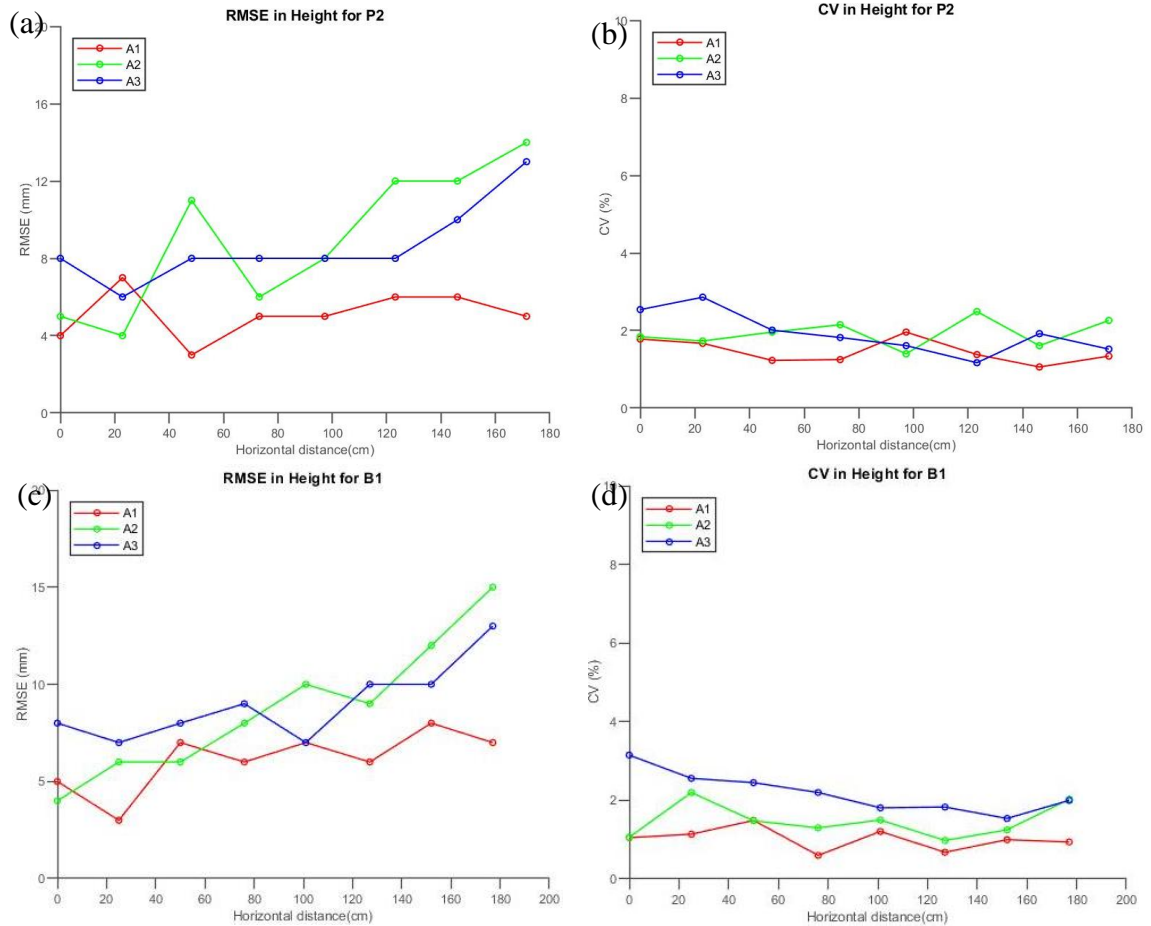*Figure 50. (a), (c) Measurement error (RMSE (mm)) and (b), (d) measurement variability (CV (%)) in the width of plant and ball while scanning at a fixed height (1.3 m), speed (0.4 m/s) and three different viewing angles (0˚, 20˚, and 35˚).*

4.3.3.3 Plant length

Beyond 20 cm from the UAV with 0° viewing angle, the plant experienced a minimal

error (under 12 mm) and did not vary with increasing horizontal distance (Figure 51(a)).

However, with the same viewing angle, the plant underneath the UAV experienced the

highest error (19 mm). The error increased considerably with increasing viewing angle,

as the inclined scanning plane might have missed hitting the trailing edge of the plant row

(along the travel direction, x-axis). The measurement variation Figure 51 (b)) also

140

showed a similar pattern as RMSE, wherein the variability increased with increasing viewing angle.

For the standard object, the error due to downdraft was minimal with a 0º viewing angle, which stayed within 14 mm (Figure 51 (c)). Similar to the plant, higher viewing angles increased the error. The measurement variation (Figure 51 (d)) was stable with 0º viewing angle with maximum variation under 5%, and higher viewing angles led to increased variations in measurement.
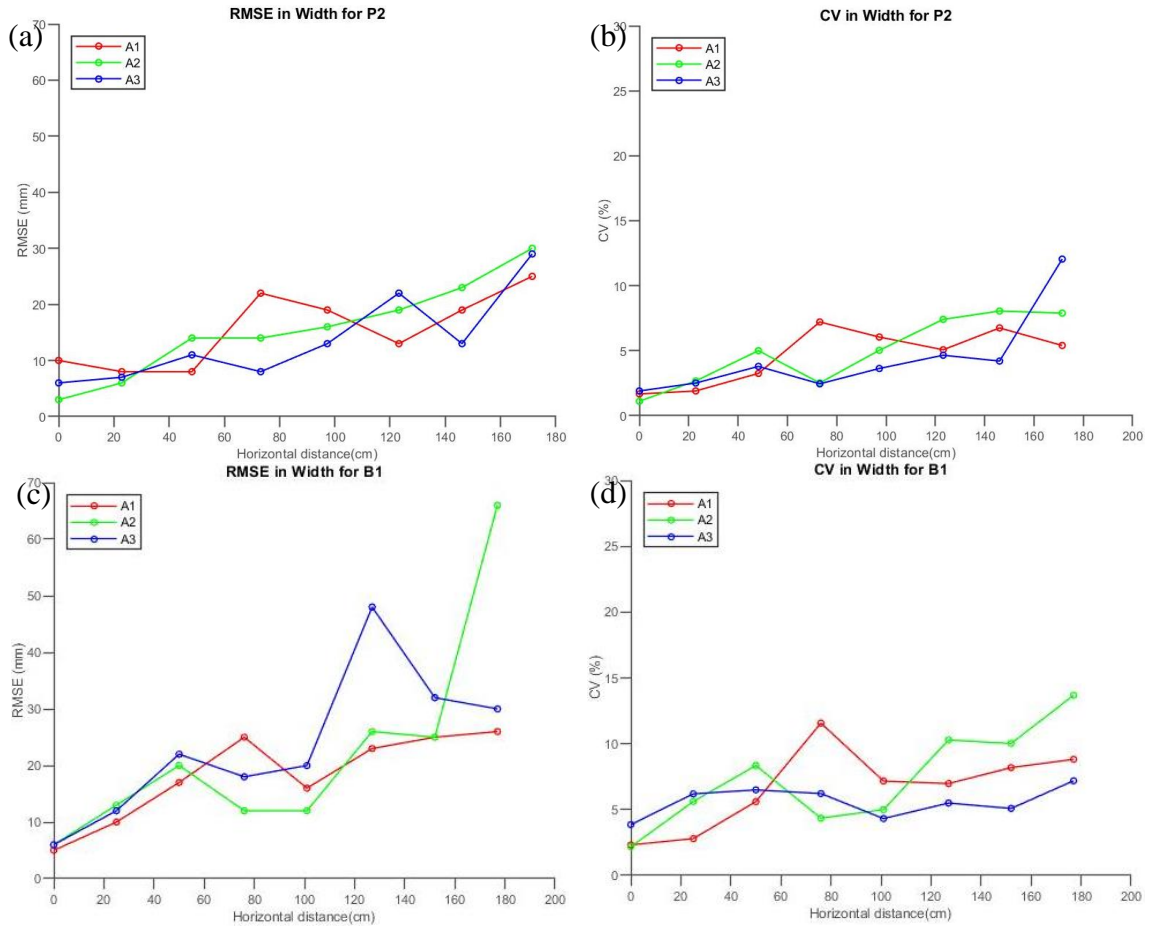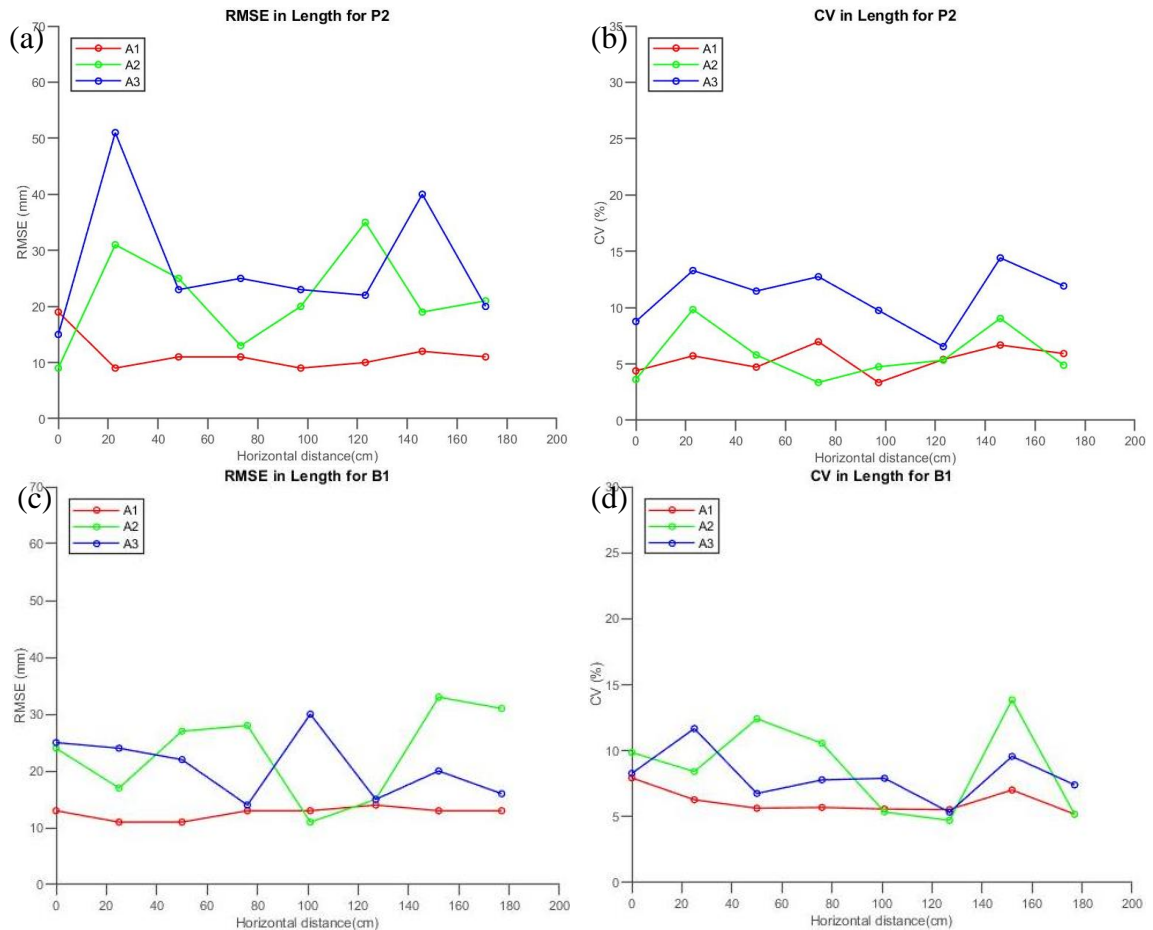
Figure 51. (a), (c) Measurement error (RMSE (mm)) and (b), (d) measurement variability (CV (%)) in the length of plant and ball while scanning at a fixed height (1.3 m), speed (0.4 m/s) and three different viewing angles (0˚, 20˚, and 35˚).

It can be concluded from the findings that both length and height measurements were stable with 0º viewing angle beyond 40 cm of the UAV, and higher viewing angles did not reduce the effect of downdraft on these measurements. However, using a higher viewing angle (35º) resulted in more stable measurements within 100 cm of the UAV in measuring the width. From the evaluation above two results, it can be concluded that the optimal way of scanning plants under downdraft is to exclude the 40 cm region while measuring length and height and use a higher viewing angle (35°) to calculate the width.

142

Chapter 5. Conclusion and Recommendation for Future Study

An aerial sensing platform was established for characterizing plants in a greenhouse environment. The reason for choosing a UAV platform over UGV or boom-based scanner was to reduce the effect of occlusion and overcome limited ground space for navigation in a greenhouse environment by extracting plant data from multiple views and reaching any point in three-dimensional space. This was achieved by integrating a 2D laser range sensor and a vision-based positioning system to a mini-UAV platform capable of generating a 3D map of an indoor environment. The study also developed a flight control system for generating flight plans and autonomous navigation of the sensing platform. A simplified GUI was developed to achieve this process and to suffice communication between the UAV onboard computer and ground computer. The performance of autonomous navigation was evaluated along a single path, including determination of UAV drift and pattern under different speeds and performance of altitude control under different flight altitudes. The study also aimed to evaluate the effect of propeller downdraft on the measurement accuracy of underlying plants under different sensor viewing angles. The study also conducted a review of existing mobile sensing systems to narrow the selection criterion of UAV, explored prevalent indoor positioning systems to overcome the limited availability of GPS signal in an indoor environment, and

obtain precise UAV location. The factors affecting the data quality of LiDAR-derived measurement on an aerial platform were investigated.

A set of scans were recorded by manually flying the aerial platform in a commercial greenhouse to test its feasibility to generate the 3D map of the scanned region. A customized offline algorithm detected and eliminated the errors generated from flight instability due to loss or gain in altitude, drift along the scanning axis, variation in the heading, and geometrical distortion in the flight path. A set of experiments were conducted in a lab environment to evaluate the performance of autonomous flight along a single path against manual flights by measuring the UAV location relative to a linear array of wooden logs placed on inverted grow pots. The results indicated that deviation from the intended flight path reduced with increasing speed, and the coefficient of determination (R^2) for the second-order model improved 0.971, 0.986, 0.998 and, 0.998 and 0.985, 0.981, 0.985, and 0.997 along the length and width, respectively, as travel speed increased 0.6, 0.8, 1.0 and 1.2 m/s.

The UAV was flown at different heights in a lab set up to assess the accuracy of Guidance-based (barometric height) altitude control, and LiDAR height was recorded. The results were compared to LiDAR-based altitude control as a baseline metric, which showed that Guidance had a greater positive offset (< 10 cm) and deviation (< 15 cm) than baseline offset (< 6 cm) and deviation (<6 cm).

The effect of propeller downdraft on plant measurement was evaluated by scanning a set of artificial plants and standard objects with the sensing platform mounted on a constant speed track at three different LiDAR viewing angles (0˚, 20˚, and 35˚). The results

144

indicated that measurement error due to the downdraft effect was very low in height (< 6 mm) and length (< 12 mm) beyond 50 cm and 20 cm from the UAV center, respectively, and nadir view resulted in the least error. However, downdraft effect on width measurement was least (< 10 mm) within 50 cm of the UAV with nadir view, and off-nadir view (35˚) had better performance, resulting in stable measurements (< 13 mm) up to 100 cm from the UAV center.

The current navigation algorithm is based on an on-off control strategy which can be improved by implementing a higher-order control system to reduce offset in altitude control. The altitude control tests using LiDAR were conducted in a lab environment with an empty floor. Real-time extraction of LiDAR-derived ground height can be tested to detect ground in a greenhouse environment, where the ground is mostly covered with plants. Thereby, Guidance based altitude control can be replaced by LiDAR-based control resulting in stable altitude performance. Improving the navigation accuracy for long-duration flights is desirable to scan larger areas at lower speeds to generate denser point clouds.

Bibliography

Aasen, H., Burkart, A., Bolten, A., Bareth, G. (2015). Generating 3D hyperspectral information with lightweight UAV snapshot cameras for vegetation monitoring: From camera calibration to quality assurance. *ISPRS Journal of Photogrammetry and Remote Sensing*, *108*, 245–259. https://doi.org/10.1016/j.isprsjprs.2015.08.002

Abhilash, P. C., Singh, N. (2009). Pesticide use and application: An Indian scenario. *Journal of Hazardous Materials*, *165*(1–3), 1–12. https://doi.org/10.1016/j.jhazmat.2008.10.061

Achtelik, M., Bachrach, A., He, R., Prentice, S., Roy, N. (2009). Stereo vision and laser odometry for autonomous helicopters in GPS-denied indoor environments. In *Unmanned Systems Technology XI* (Vol. 7332, p. 733219). SPIE. https://doi.org/10.1117/12.819082

Addis, D., Shen, Y., Liu, H., Hussain, F. (2018). *A Lidar-Based Tree Canopy Detection System Development*.

Akyildiz, I. F., Su, W., Sankarasubramaniam, Y., Cayirci, E. (2001). *Wireless sensor networks: a survey*. Retrieved from www.elsevier.com/locate/comnet

Al Habsi, S., Shehada, M., Abdoon, M., Mashood, A., Noura, H. (2016). Integration of a Vicon camera system for indoor flight of a Parrot AR Drone. *ISMA 2015 - 10th International Symposium on Mechatronics and Its Applications*. https://doi.org/10.1109/ISMA.2015.7373476

Anderson, K., Hancock, S., Disney, M., Gaston, K. J. (2016). Is waveform worth it? A comparison of LiDAR approaches for vegetation and landscape characterization. *Remote Sensing in Ecology and Conservation*, *2*(1), 5–15. https://doi.org/10.1002/rse2.8

Anthony, D. (2017). UAV Localization in Row Crops *, *34*(7), 1275–1296. https://doi.org/10.1002/rob.21706

Anthony, D., Elbaum, S., Lorenz, A., Detweiler, C. (2014). On crop height estimation with UAVs. In *IEEE International Conference on Intelligent Robots and Systems* (pp. 4805–4812). Institute of Electrical and Electronics Engineers Inc. https://doi.org/10.1109/IROS.2014.6943245

Archibald, B. A., Solomon, K. R., Stephenson, G. R. (1995). Estimation of pesticide exposure to greenhouse applicators using video imaging and other assessment techniques. *American Industrial Hygiene Association Journal*, *56*(3), 226–235.

https://doi.org/10.1080/15428119591017051

Arnó, J., Escolà, A., Vallès, J. M., Llorens, J., Sanz, R., Masip, J., … Rosell-Polo, J. R. (2013). Leaf area index estimation in vineyards using a ground-based LiDAR scanner. *Precision Agriculture*, *14*(3), 290–306. https://doi.org/10.1007/s11119-012-9295-0

Bachrach, A. G., Roy, N., Orlando, T. (2009). *Autonomous Flight in Unstructured and Unknown Indoor Environments Abraham Galton Bachrach*. *Learning*.

Barber, D., Mills, J., Smith-Voysey, S. (2008). Geometric validation of a ground-based mobile laser scanning system. *ISPRS Journal of Photogrammetry and Remote Sensing*, *63*(1), 128–141. https://doi.org/10.1016/j.isprsjprs.2007.07.005

Bareth, G., Bendig, J., Tilly, N., Hoffmeister, D., Aasen, H., Bolten, A. (2016). A comparison of UAV- and TLS-derived plant height for crop monitoring: Using polygon grids for the analysis of crop surface models (CSMs). *Photogrammetrie, Fernerkundung, Geoinformation*, *2016*(2), 85–94. https://doi.org/10.1127/pfg/2016/0289

Barnard, H. R., Findley, M. C., Csavina, J. (2014). PARduino: A simple and inexpensive device for logging photosynthetically active radiation. *Tree Physiology*, *34*(6), 640–645. https://doi.org/10.1093/treephys/tpu044

Bortoff, S. A. (2000). Path planning for UAVs. *Proceedings of the American Control Conference*, *1*(October 2000), 364–368. https://doi.org/10.1109/acc.2000.878915

Cabrera, F. J., Baille, A., López, J. C., González-Real, M. M., Pérez-Parra, J. (2009). Effects of cover diffusive properties on the components of greenhouse solar radiation. *Biosystems Engineering*, *103*(3), 344–356. https://doi.org/10.1016/j.biosystemseng.2009.03.008

Campos, J., Llop, J., Gallart, M., García-Ruiz, F., Gras, A., Salcedo, R., Gil, E. (2019). Development of canopy vigour maps using UAV for site-specific management during vineyard spraying process. *Precision Agriculture*, *20*(6), 1136–1156. https://doi.org/10.1007/s11119-019-09643-z

Cantón Paterna, V., Calveras Augé, A., Paradells Aspas, J., Pérez Bullones, M. A. (2017). A Bluetooth Low Energy Indoor Positioning System with Channel Diversity, Weighted Trilateration and Kalman Filtering. *Sensors (Basel, Switzerland)*, *17*(12). https://doi.org/10.3390/s17122927

Caturegli, L., Corniglia, M., Gaetani, M., Grossi, N., Magni, S., Migliazzi, M., … Volterrani, M. (2016). Unmanned aerial vehicle to estimate nitrogen status of turfgrasses. *PLoS ONE*, *11*(6). https://doi.org/10.1371/journal.pone.0158268

Changshuai, Y., Haitao, L., Siwei, G. (2019). Vibration test and vibration reduction design of UAV load radar. In *ACM International Conference Proceeding Series*. Association for Computing Machinery. https://doi.org/10.1145/3351917.3351980

Chawathe, S. S. (2009). Low-latency indoor localization using Bluetooth beacons. In *IEEE Conference on Intelligent Transportation Systems, Proceedings, ITSC* (pp. 467–473). https://doi.org/10.1109/ITSC.2009.5309711

Chen, Y., Baek, D., Bocca, A., Macii, A., Macii, E., Poncino, M. (2019). A case for a battery-aware model of drone energy consumption. In *INTELEC, International Telecommunications Energy Conference (Proceedings)* (Vol. 2018-Octob). Institute of Electrical and Electronics Engineers Inc. https://doi.org/10.1109/INTLEC.2018.8612333

Chen, Y., Ozkan, H. E., Zhu, H., Derksen, R. C., Krause, C. R. (2013). Spray deposition inside tree canopies from a newly developed variable-rate air-assisted sprayer. *Transactions of the ASABE*, *56*(6), 1263–1272. https://doi.org/10.13031/trans.56.9839

Chen, Y., Zhu, H., Ozkan, H. E. (2012). Development of a variable-rate sprayer with laser scanning sensor to synchronize spray outputs to tree structures. *Transactions of the ASABE*, *55*(3), 773–781. https://doi.org/10.13031/2013.41509

Chisholm, R. A., Cui, J., Lum, S. K. Y., Chen, B. M. (2013). UAV LiDAR for below-canopy forest surveys. *Journal of Unmanned Vehicle Systems*, *01*(01), 61–68. https://doi.org/10.1139/juvs-2013-0017

Christiansen, M. P., Laursen, M. S., Jørgensen, R. N., Skovsen, S., Gislum, R. (2017). Designing and testing a UAV mapping system for agricultural field surveying. *Sensors (Switzerland)*, *17*(12), 1–19. https://doi.org/10.3390/s17122703

Comba, L., Gay, P., Primicerio, J., Ricauda Aimonino, D. (2015). Vineyard detection from unmanned aerial systems images. *Computers and Electronics in Agriculture*, *114*, 78–87. https://doi.org/10.1016/j.compag.2015.03.011

Dabove, P., Di Pietra, V., Piras, M., Jabbar, A. A., Kazim, S. A. (2018). Indoor positioning using Ultra-wide band (UWB) technologies: Positioning accuracies and sensors' performances. *2018 IEEE/ION Position, Location and Navigation Symposium, PLANS 2018 - Proceedings*, 175–184. https://doi.org/10.1109/PLANS.2018.8373379

Dahlin Rodin, C., de Alcantara Andrade, F. A., Hovenburg, A. R., Johansen, T. A. (2019). A Survey of Practical Design Considerations of Optical Imaging Stabilization Systems for Small Unmanned Aerial Systems. *Sensors (Basel,*

Switzerland), *19*(21). https://doi.org/10.3390/s19214800

Derksen, R. C., Frantz, J., Ranger, C. M., Locke, J. C., Zhu, H., Krause, C. R. (2007). COMPARING GREENHOUSE HANDGUN DELIVERY TO POINSETTIAS BY SPRAY VOLUME AND QUALITY. *Transactions of the ASABE*, *51*(1), 27–33.

Diosi, A., Kleeman, L. (2005). *Laser Scan Matching in Polar Coordinates with Application to SLAM*. Retrieved from www.irrc.monash.edu.au/adiosi.

Dong, J., Noreikis, M., Xiao, Y., Ylä-Jääski, A. (2019). ViNav: A Vision-Based Indoor Navigation System for Smartphones. *IEEE Transactions on Mobile Computing*, *18*(6), 1461–1475. https://doi.org/10.1109/TMC.2018.2857772

Duarte-Galvan, C., Torres-Pacheco, I., Guevara-Gonzalez, R. G., Romero-Troncoso, R. J., Contreras-Medina, L. M., Rios-Alcaraz, M. A., Millan-Almaraz, J. R. (2012). Revisión. Ventajas y desventajas de los sistemas de control climático aplicados en agricultura de precisión. *Spanish Journal of Agricultural Research*, *10*(4), 926–938. https://doi.org/10.5424/sjar/2012104-487-11

Durmus, H., Gunes, E. O., Kirci, M. (2016). Data acquisition from greenhouses by using autonomous mobile robot. *2016 5th International Conference on Agro-Geoinformatics, Agro-Geoinformatics 2016*, 5–9. https://doi.org/10.1109/Agro-Geoinformatics.2016.7577696

Escolà, A., Planas, S., Rosell, J. R., Pomar, J., Camp, F., Solanelles, F., … Gil, E. (2011). Performance of an ultrasonic ranging sensor in apple tree canopies. *Sensors*, *11*(3), 2459–2477. https://doi.org/10.3390/s110302459

Fang, Y., Deng, Z., Xue, C., Jiao, J., Zeng, H., Zheng, R., Lu, S. (2015). Application of an improved K nearest neighbor algorithm in WiFi indoor positioning. *Lecture Notes in Electrical Engineering*, *342*, 517–524. https://doi.org/10.1007/978-3-662-46632-2_45

Faragher, R., Harle, R. (2014). An Analysis of the Accuracy of Bluetooth Low Energy for Indoor Positioning Applications. In *Proceedings of the 27th International Technical Meeting of The Satellite Division of the Institute of Navigation (ION GNSS+ 2014)* (pp. 201–210).

French, A. N., Gore, M. A., Thompson, A. (2016). Cotton phenotyping with lidar from a track-mounted platform. In *Autonomous Air and Ground Sensing Systems for Agricultural Optimization and Phenotyping* (Vol. 9866, p. 98660B). SPIE. https://doi.org/10.1117/12.2224423

Gan-Mor, S., Ronen, B., Josef, S., Yuri, B. (1996). (steel pipe guide) Guidance for Automatic Vehicle for greenhouse transportation.pdf. *Agricultural Research*

Organization, 99–103.

García-Quijano, M. J., Jensen, J. R., Hodgson, M. E., Hadley, B. C., Gladden, J. B., Lapine, L. A. (2008). *Significance of altitude and posting density on LiDAR-derived elevation accuracy on hazardous waste sites*.

Getzin, S., Wiegand, K., Schöning, I. (2012). Assessing biodiversity in forests using very high-resolution images and unmanned aerial vehicles. *Methods in Ecology and Evolution*. https://doi.org/10.1111/j.2041-210X.2011.00158.x

Gigl, T., Janssen, G. J. M., Dizdarevi´cdizdarevi´c, V., Witrisal, K., Irahhauten, Z. (2007). *Analysis of a UWB Indoor Positioning System Based on Received Signal Strength*.

Gil, E., Escolà, A., Rosell, J. R., Planas, S., Val, L. (2007). Variable rate application of plant protection products in vineyard using ultrasonic sensors. *Crop Protection*, *26*(8), 1287–1297. https://doi.org/10.1016/j.cropro.2006.11.003

González-Jorge, H., Martínez-Sánchez, J., Bueno, M., Arias, P. (2017, December 1). Unmanned aerial systems for civil applications: A review. *Drones*. MDPI AG. https://doi.org/10.3390/drones1010002

Haghighattalab, A., González Pérez, L., Mondal, S., Singh, D., Schinstock, D., Rutkoski, J., … Poland, J. (2016). Application of unmanned aerial systems for high throughput phenotyping of large wheat breeding nurseries. *Plant Methods*, *12*(1). https://doi.org/10.1186/s13007-016-0134-6

Harik, E. H. C., Korsaeth, A. (2018). Combining hector SLAM and artificial potential field for autonomous navigation inside a greenhouse. *Robotics*, *7*(2). https://doi.org/10.3390/robotics7020022

Hatfield, J. L. (2014). Radiation use efficiency: Evaluation of cropping and management systems. *Agronomy Journal*, *106*(5), 1820–1827. https://doi.org/10.2134/agronj2013.0310

Hauschildt, D., Kirchhof, N. (2010). Advances in thermal infrared localization: Challenges and solutions. *2010 International Conference on Indoor Positioning and Indoor Navigation, IPIN 2010 - Conference Proceedings*, (September), 15–17. https://doi.org/10.1109/IPIN.2010.5647415

Hemming, J., Wouter Bac, C., van Tuijl, B. A., Barth, R., Bontsema, J., Pekkeriet, E., van Henten, E. J. (2014). *A robot for harvesting sweet-pepper in greenhouses*. Retrieved from www.eurageng.eu

Hemming, S., Van Der Braak, N., Dueck, T., Jongschaap, R., Marissen, N. (2006).

150

Filtering Natural Light by the Greenhouse Covering Using Model Simulations-More Production and Better Plant Quality by Diffuse Light?

Hernández, N., Ocaña, M., Alonso, J. M., Kim, E. (2017). Continuous space estimation: Increasingwifi-based indoor localization resolution without increasing the site-survey effort. *Sensors (Switzerland)*, *17*(1). https://doi.org/10.3390/s17010147

Heuvelink, E., Challa, H. (1989). Dynamic optimization of artificial lighting in greenhouses. *Acta Horticulture*, *260*, 401–412.

Hilker, T., van Leeuwen, M., Coops, N. C., Wulder, M. A., Newnham, G. J., Jupp, D. L. B., Culvenor, D. S. (2010). Comparing canopy metrics derived from terrestrial and airborne laser scanning in a Douglas-fir dominated forest stand. *Trees - Structure and Function*, *24*(5), 819–832. https://doi.org/10.1007/s00468-010-0452-7

Hosoi, F., Nakabayashi, K., Omasa, K. (2011). 3-D modeling of tomato canopies using a high-resolution portable scanning lidar for extracting structural information. *Sensors*, *11*(2), 2166–2174. https://doi.org/10.3390/s110202166

Hug, C., Ullrich, A., Grimm, A. (2004). *LITEMAPPER-5600-A WAVEFORM-DIGITIZING LIDAR TERRAIN AND VEGETATION MAPPING SYSTEM*.

Hyuc Ko, M., Chul Kim, K., Suprem, A., Mahalik, N. P., Sahng Ryuh, B. (2014). 4WD mobile robot for autonomous steering using single camera based vision system. *International Journal of Intelligent Unmanned Systems*, *2*(3), 168–182. https://doi.org/10.1108/IJIUS-06-2014-0005

Ignjatovic, B. R., Andjelinic, B. B., Simic, M. I. (2013). Impact of the user orientation on WLAN positioning based upon the access point with the strongest signal. *2013 11th International Conference on Telecommunications in Modern Satellite, Cable and Broadcasting Services, TELSIKS 2013*, *1*, 233–236. https://doi.org/10.1109/TELSKS.2013.6704925

Ilkovicova, L. (2016). Positioning System in Indoor Environment Using Ultrasound Technology. *16th International Multidisciplinary Scientific GeoConference SGEM2016, Informatics, Geoinformatics and Remote Sensing*, *2*, 487–495. https://doi.org/10.5593/sgem2016/b22/s09.063

Israel, M. (2012). a Uav-Based Roe Deer Fawn Detection System. *ISPRS - International Archives of the Photogrammetry, Remote Sensing and Spatial Information Sciences*, *XXXVIII-1/*, 51–55. https://doi.org/10.5194/isprsarchives-xxxviii-1-c22-51-2011

Itagaki, Y., Suzuki, A., Iyota, T. (2012). Indoor positioning for moving objects using a hardware device with spread spectrum ultrasonic waves. *2012 International Conference on Indoor Positioning and Indoor Navigation, IPIN 2012 - Conference*

Proceedings, (November), 13–15. https://doi.org/10.1109/IPIN.2012.6418850

Iversen, B. B. (2018). Stereo Visual Odometry for Indoor Positioning, (June).

Jannoura, R., Brinkmann, K., Uteau, D., Bruns, C., Joergensen, R. G. (2015). Monitoring of crop biomass using true colour aerial photographs taken from a remote controlled hexacopter. *Biosystems Engineering*, *129*, 341–351. https://doi.org/10.1016/j.biosystemseng.2014.11.007

Januszkiewicz, Ł., Kawecki, J., Kawecki, R., Oleksy, P. (2016). Wireless indoor positioning system with inertial sensors and infrared beacons. *2016 10th European Conference on Antennas and Propagation, EuCAP 2016*, 5–7. https://doi.org/10.1109/EuCAP.2016.7481650

Jay, S., Rabatel, G., Hadoux, X., Moura, D., Gorretta, N. (2015). In-field crop row phenotyping from 3D modeling performed using Structure from Motion. *Computers and Electronics in Agriculture*, *110*, 70–77. https://doi.org/10.1016/j.compag.2014.09.021

Jeon, H. Y., Zhu, H. (2012). DEVELOPMENT OF A VARIABLE-RATE SPRAYER FOR NURSERY LINER APPLICATIONS, *55*(2002), 303–312.

Jin, X., Liu, S., Baret, F., Hemerlé, M., Comar, A. (2017). Estimates of plant density of wheat crops at emergence from very low altitude UAV imagery. *Remote Sensing of Environment*, *198*, 105–114. https://doi.org/10.1016/j.rse.2017.06.007

Keightley, K. E., Bawden, G. W. (2010). 3D volumetric modeling of grapevine biomass using Tripod LiDAR. *Computers and Electronics in Agriculture*, *74*(2), 305–312. https://doi.org/10.1016/j.compag.2010.09.005

Kim, S. C., Jeong, Y. S., Park, S. O. (2013). RFID-based indoor location tracking to ensure the safety of the elderly in smart home environments. *Personal and Ubiquitous Computing*, *17*(8), 1699–1707. https://doi.org/10.1007/s00779-012-0604-4

Kim, S. J., Kim, B. K. (2013). Dynamic ultrasonic hybrid localization system for indoor mobile robots. *IEEE Transactions on Industrial Electronics*, *60*(10), 4562–4573. https://doi.org/10.1109/TIE.2012.2216235

Kise, M., Zhang, Q. (2008). Development of a stereovision sensing system for 3D crop row structure mapping and tractor guidance. *Biosystems Engineering*, *101*(2), 191–198. https://doi.org/10.1016/j.biosystemseng.2008.08.001

Klose, R., Penlington, J., Ruckelshausen, A. (2011). Usability of 3D time-of-flight cameras for automatic plant phenotyping. *Bornimer Agrartechnische Berichte*, *69*,

93–105. Retrieved from http://www2.atb-potsdam.de/cigr-imageanalysis/images/09_110_Klose.pdf

Ko, M. H., Ryuh, B. S., Kim, K. C., Suprem, A., Mahalik, N. P. (2015). Autonomous Greenhouse Mobile Robot Driving Strategies from System Integration Perspective: Review and Application. *IEEE/ASME Transactions on Mechatronics*, *20*(4), 1705–1716. https://doi.org/10.1109/TMECH.2014.2350433

Koch, T., Körner, M., Fraundorfer, F. (2019). Automatic and semantically-aware 3D UAV flight planning for image-based 3D reconstruction. *Remote Sensing*, *11*(13). https://doi.org/10.3390/rs11131550

Kumar, G. A., Patil, A. K., Patil, R., Park, S. S., Chai, Y. H., Ajay Kumar, G., … Chai, Y. H. (2017). A LiDAR and IMU integrated indoor navigation system for UAVs and its application in real-time pipeline classification. *Sensors (Switzerland)*, *17*(6), 1268. https://doi.org/10.3390/s17061268

Lee, J. O., Kang, T., Lee, K. H., Im, S. K., Park, J. (2011). Vision-based indoor localization for unmanned aerial vehicles. *Journal of Aerospace Engineering*, *24*(3), 373–377. https://doi.org/10.1061/(ASCE)AS.1943-5525.0000064

Lei, L., Qiu, C., Li, Z., Han, D., Han, L., Zhu, Y., … Yang, G. (2019). Effect of leaf occlusion on leaf area index inversion of maize using UAV-LiDAR data. *Remote Sensing*, *11*(9). https://doi.org/10.3390/rs11091067

Li, R. A., Sha, X., Lin, K. (2014). Smart greenhouse: A real-time mobile intelligent monitoring system based on WSN. In *IWCMC 2014 - 10th International Wireless Communications and Mobile Computing Conference* (pp. 1152–1156). Institute of Electrical and Electronics Engineers Inc. https://doi.org/10.1109/IWCMC.2014.6906517

Li, R., Liu, J., Zhang, L., Hang, Y. (2014). LIDAR/MEMS IMU integrated navigation (SLAM) method for a small UAV in indoor environments. In *2014 DGON Inertial Sensors and Systems, ISS 2014 - Proceedings*. Institute of Electrical and Electronics Engineers Inc. https://doi.org/10.1109/InertialSensors.2014.7049479

Li, S., Gan, X., Huang, L., Zhang, H. (2019). Object Recognition and Simultaneous Indoor Localization Algorithm with Stereo Camera. *Proceedings of 2018 5th IEEE International Conference on Cloud Computing and Intelligence Systems, CCIS 2018*, 405–409. https://doi.org/10.1109/CCIS.2018.8691211

Li, Zhe, Yan, Y., Jing, Y., Zhao, S. G. (2015). The design and testing of a LiDAR platform for a UAV for heritage mapping. In *International Archives of the Photogrammetry, Remote Sensing and Spatial Information Sciences - ISPRS*

153

Archives (Vol. 40, pp. 17–24). International Society for Photogrammetry and Remote Sensing. https://doi.org/10.5194/isprsarchives-XL-1-W4-17-2015

Li, Zhenming, Lao, M., Phang, S. K., Redhwan, M., Hamid, A., Zuea Tang, K., Lin, F. (2017). *Development and Design Methodology of an Anti-Vibration System on Micro-UAVs*.

Lin, Y. (2015, November 1). LiDAR: An important tool for next-generation phenotyping technology of high potential for plant phenomics? *Computers and Electronics in Agriculture*. Elsevier B.V. https://doi.org/10.1016/j.compag.2015.10.011

Lin, Y., Hyyppä, J. (2016). A comprehensive but efficient framework of proposing and validating feature parameters from airborne LiDAR data for tree species classification. *International Journal of Applied Earth Observation and Geoinformation*, *46*, 45–55. https://doi.org/10.1016/j.jag.2015.11.010

Lindberg, E., Olofsson, K., Holmgren, J., Olsson, H. (2012). Estimation of 3D vegetation structure from waveform and discrete return airborne laser scanning data. *Remote Sensing of Environment*, *118*, 151–161. https://doi.org/10.1016/j.rse.2011.11.015

Liu, B., Paquin, N. (2018). *ViconMAVLink: A SOFTWARE TOOL FOR INDOOR POSITIONING USING A MOTION CAPTURE SYSTEM*.

Liu, J., Melloh, R. A., Woodcock, C. E., Davis, R. E., Painter, T. H., McKenzie, C. (2008). Modeling the view angle dependence of gap fractions in forest canopies: Implications for mapping fractional snow cover using optical remote sensing. *Journal of Hydrometeorology*, *9*(5), 1005–1019. https://doi.org/10.1175/2008JHM866.1

Liu, K., Dong, X., Qiu, B. (2018). Analysis of cotton height spatial variability based on UAV-LiDAR. *International Journal of Precision Agricultural Aviation*, *1*(1), 72–76. https://doi.org/10.33440/j.ijpaa.20200303.79

Llorens, J., Gil, E., Llop, J., Escolà, A., Methods, A. (2011). Ultrasonic and LIDAR sensors for electronic canopy characterization in vineyards: Advances to improve pesticide application methods. *Sensors*, *11*(2), 2177–2194. https://doi.org/10.3390/s110202177

Lowe, D. G. (1999). Object Recognition from Local Scale-Invariant Features. *Proceedings of the Seventh IEEE International Conference on Computer Vision*, *2*, 1150–1157.

Maddern, W., Pascoe, G., Newman, P. (2015). Leveraging experience for large-scale LIDAR localisation in changing cities. In *Proceedings - IEEE International Conference on Robotics and Automation* (Vol. 2015-June, pp. 1684–1691). Institute

of Electrical and Electronics Engineers Inc.
https://doi.org/10.1109/ICRA.2015.7139414

Madison, R., Andrews, G., Debitetto, P., Rasmussen, S., Bottkol, M. (2007). Vision-aided navigation for small UAVs in GPS-challenged environments. *Collection of Technical Papers - 2007 AIAA InfoTech at Aerospace Conference*, *3*(September 2015), 2733–2745. https://doi.org/10.2514/6.2007-2986

Mahfouz, M. R., Zhang, C., Merkl, B. C., Kuhn, M. J., Fathy, A. E. (2008). Investigation of high-accuracy indoor 3-D positioning using UWB technology. *IEEE Transactions on Microwave Theory and Techniques*, *56*(6), 1316–1330. https://doi.org/10.1109/TMTT.2008.923351

Mainetti, L., Patrono, L., Sergi, I. (2014). A survey on indoor positioning systems. In *2014 22nd International Conference on Software, Telecommunications and Computer Networks, SoftCOM 2014* (pp. 111–120). Institute of Electrical and Electronics Engineers Inc. https://doi.org/10.1109/SOFTCOM.2014.7039067

Mangiameli, M., Muscato, G., Mussumeci, G., Milazzo, C. (2013). *A GIS application for UAV flight planning*. *IFAC Proceedings Volumes* (Vol. 46). IFAC. https://doi.org/10.3182/20131120-3-FR-4045.00025

Matese, A., Di Gennaro, S. F., Zaldei, A., Genesio, L., Vaccari, F. P. (2009). A wireless sensor network for precision viticulture: The NAV system. *Computers and Electronics in Agriculture*, *69*(1), 51–58. https://doi.org/10.1016/j.compag.2009.06.016

Medina, C., Segura, J. C., De la Torre, Á. (2013). Ultrasound indoor positioning system based on a low-power wireless sensor network providing sub-centimeter accuracy. *Sensors (Switzerland)*, *13*(3), 3501–3526. https://doi.org/10.3390/s130303501

Medrano, E., Lorenzo, P., Sánchez-Guerrero, M. C., Montero, J. I. (2005). Evaluation and modelling of greenhouse cucumber-crop transpiration under high and low radiation conditions. *Scientia Horticulturae*, *105*(2), 163–175. https://doi.org/10.1016/j.scienta.2005.01.024

Meng, W., He, Y., Deng, Z., Li, C. (2012). Optimized access points deployment for WLAN indoor positioning system. *IEEE Wireless Communications and Networking Conference, WCNC*, 2457–2461. https://doi.org/10.1109/WCNC.2012.6214209

Merino, L., Caballero, F., Martínez-De-Dios, J. R., Maza, I., Ollero, A. (2012). An unmanned aircraft system for automatic forest fire monitoring and measurement. *Journal of Intelligent and Robotic Systems: Theory and Applications*, *65*(1–4), 533–548. https://doi.org/10.1007/s10846-011-9560-x

Miranda-Fuentes, A., Llorens, J., Rodríguez-Lizana, A., Cuenca, A., Gil, E., Blanco-Roldán, G. L., Gil-Ribes, J. A. (2016). Assessing the optimal liquid volume to be sprayed on isolated olive trees according to their canopy volumes. *Science of the Total Environment*, *568*, 296–305. https://doi.org/10.1016/j.scitotenv.2016.06.013

Moeckel, T., Dayananda, S., Nidamanuri, R. R., Nautiyal, S., Hanumaiah, N., Buerkert, A., Wachendorf, M. (2018). Estimation of vegetable crop parameter by multi-temporal UAV-borne images. *Remote Sensing*, *10*(5). https://doi.org/10.3390/rs10050805

Moltó, E., Martín, B., Gutiérrez, A. (2000). Design and testing of an automatic machine for spraying at a constant distance from the tree canopy. *Journal of Agricultural and Engineering Research*, *77*(4), 379–384. https://doi.org/10.1006/jaer.2000.0621

Moorthy, I., Miller, J. R., Hu, B., Chen, J., Li, Q. (2008). *Retrieving crown leaf area index from an individual tree using ground-based lidar data*. Retrieved from http://pubs.nrc-cnrc.gc.ca/cjrs

Mustafah, Y. M., Azman, A. W., Akbar, F. (2012). Indoor UAV positioning using stereo vision sensor. *Procedia Engineering*, *41*(Iris), 575–579. https://doi.org/10.1016/j.proeng.2012.07.214

Neburka, J., Tlamsa, Z., Benes, V., Polak, L., Kaller, O., Bolecek, L., … Kratochvil, T. (2016). Study of the performance of RSSI based bluetooth smart indoor positioning. In *2016 26th International Conference Radioelektronika, RADIOELEKTRONIKA 2016* (pp. 121–125). Institute of Electrical and Electronics Engineers Inc. https://doi.org/10.1109/RADIOELEK.2016.7477344

Ni, J., Yao, L., Zhang, J., Cao, W., Zhu, Y., Tai, X. (2017). Development of an unmanned aerial vehicle-borne crop-growth monitoring system. *Sensors (Switzerland)*, *17*(3). https://doi.org/10.3390/s17030502

Ni, L. M., Liu, Y., Lau, Y. C., Patil, A. P. (2003). LANDMARC: Indoor location sensing using active RFID. In *Proceedings of the 1st IEEE International Conference on Pervasive Computing and Communications, PerCom 2003* (pp. 407–415). https://doi.org/10.1109/percom.2003.1192765

Nirjon, S., Liu, J., DeJean, G., Priyantha, B., Jin, Y., Hart, T. (2014). COIN-GPS: Indoor localization from direct GPS receiving. In *MobiSys 2014 - Proceedings of the 12th Annual International Conference on Mobile Systems, Applications, and Services* (pp. 301–314). Association for Computing Machinery. https://doi.org/10.1145/2594368.2594378

Nolan, A. P., Park, S., O'Connell, M., Fuentes, S., Ryu, D., Chung, H. (2015).

Automated detection and segmentation of vine rows using high resolution UAS imagery in a commercial vineyard. *Proceedings - 21st International Congress on Modelling and Simulation, MODSIM 2015*, 1406–1412.

Nong, X., Cheng, L., Yating, D., Rui, P., Chen, Y., Wu, H. (2018). Research on indoor navigation of mobile robot based on INS and ultrasound. *Proceedings of the 2017 12th IEEE Conference on Industrial Electronics and Applications, ICIEA 2017*, *2018-Febru*, 231–235. https://doi.org/10.1109/ICIEA.2017.8282848

Nuyttens, D., Windey, S., Sonck, B. (2004). *Comparison of Operator Exposure for Five Different Greenhouse Spraying Applications*. *Journal of Agricultural Safety and Health* (Vol. 10).

Pahuja, R., Verma, H. K., Uddin, M. (2013). A Wireless Sensor network for greenhouse climate control. *IEEE CS*, *13*, 1536–1268.

Pang, Y., Lefsky, M., Sun, G., Ranson, J. (2011). Impact of footprint diameter and off-nadir pointing on the precision of canopy height estimates from spaceborne lidar. *Remote Sensing of Environment*, *115*(11), 2798–2809. https://doi.org/10.1016/j.rse.2010.08.025

Pawlowski, A., Guzman, J. L., Rodríguez, F., Berenguel, M., Sánchez, J., Dormido, S. (2009). Simulation of greenhouse climate monitoring and control with wireless sensor network and event-based control. *Sensors*, *9*(1), 232–252. https://doi.org/10.3390/s90100232

Piatti, D., Rinaudo, F. (2012). SR-4000 and CamCube3.0 Time of Flight (ToF) Cameras: Tests and Comparison. *Remote Sensing*, *4*(4), 1069–1089. https://doi.org/10.3390/rs4041069

Pierlot, V., Droogenbroeck, M. Van. (2014). BeAMS: A beacon-based angle measurement sensor for mobile robot positioning. *IEEE Transactions on Robotics*, *30*(3), 533–549. https://doi.org/10.1109/TRO.2013.2293834

Pilarski, T., Happold, M., Pangels, H., Ollis, M., Fitzpatrick, K., Stentz, A. (2002). The Demeter system for automated harvesting. *Autonomous Robots*, *13*(1), 9–20. https://doi.org/10.1023/A:1015622020131

Primicerio, J., Di Gennaro, S. F., Fiorillo, E., Genesio, L., Lugato, E., Matese, A., Vaccari, F. P. (2012). A flexible unmanned aerial vehicle for precision agriculture. *Precision Agriculture*, *13*(4), 517–523. https://doi.org/10.1007/s11119-012-9257-6

Radkowski, S., Szulim, P. (2014). Analysis of vibration of rotors in unmanned aircraft. In *2014 19th International Conference on Methods and Models in Automation and Robotics, MMAR 2014* (pp. 748–753). Institute of Electrical and Electronics

Engineers Inc. https://doi.org/10.1109/MMAR.2014.6957449

Radoglou-Grammatikis, P., Sarigiannidis, P., Lagkas, T., Moscholios, I. (2020). A compilation of UAV applications for precision agriculture. *Computer Networks*, *172*. https://doi.org/10.1016/j.comnet.2020.107148

Rafiq, A., Kalantari, D., Mashhadimeyghani, H. (2014). Construction and development of an automatic sprayer for greenhouse. *Agricultural Engineering International: CIGR Journal*, *16*(2), 36–40.

Rokhmana, C. A. (2015). The Potential of UAV-based Remote Sensing for Supporting Precision Agriculture in Indonesia. *Procedia Environmental Sciences*, *24*, 245–253. https://doi.org/10.1016/j.proenv.2015.03.032

Roldán, J. J., Joossen, G., Sanz, D., del Cerro, J., Barrientos, A. (2015). Mini-UAV based sensory system for measuring environmental variables in greenhouses. *Sensors (Switzerland)*, *15*(2), 3334–3350. https://doi.org/10.3390/s150203334

Rosell, J. R., Sanz, R. (2012, February). A review of methods and applications of the geometric characterization of tree crops in agricultural activities. *Computers and Electronics in Agriculture*. https://doi.org/10.1016/j.compag.2011.09.007

Rosell, Joan Ramon, Llorens, J., Sanz, R., Arnó, J., Ribes-Dasi, M., Masip, J., … Rosell, J. R. (2009). Obtaining the three-dimensional structure of tree orchards from remote 2D terrestrial LIDAR scanning. *Agricultural and Forest Meteorology*, *149*(9), 1505–1515. https://doi.org/10.1016/j.agrformet.2009.04.008

Ruiz-Larrea, A., Roldán, J. J., Garzón, M., Del Cerro, J., Barrientos, A. (2016). A UGV approach to measure the ground properties of greenhouses. In *Advances in Intelligent Systems and Computing* (Vol. 418, pp. 3–13). Springer Verlag. https://doi.org/10.1007/978-3-319-27149-1_1

Saab, S. S., Nakad, Z. S. (2011). A standalone RFID indoor positioning system using passive tags. *IEEE Transactions on Industrial Electronics*, *58*(5), 1961–1970. https://doi.org/10.1109/TIE.2010.2055774

Sammons, P., Furukawa, T., Bulgin, A. (2005). Autonomous pesticide spraying robot for use in a greenhouse. *Proceedings of the 2005 Australasian Conference on Robotics and Automation, ACRA 2005*, *1*(9), 1–9.

Santesteban, L. G., Di Gennaro, S. F., Herrero-Langreo, A., Miranda, C., Royo, J. B., Matese, A. (2017). High-resolution UAV-based thermal imaging to estimate the instantaneous and seasonal variability of plant water status within a vineyard. *Agricultural Water Management*, *183*, 49–59. https://doi.org/10.1016/j.agwat.2016.08.026

Sanz-Cortiella, R., Llorens-Calveras, J., Escolà, A., Arnó-Satorra, J., Ribes-Dasi, M., Masip-Vilalta, J., … Rosell-Polo, J. R. (2011). Innovative LIDAR 3D dynamic measurement system to estimate fruit-tree leaf area. *Sensors*, *11*(6), 5769–5791. https://doi.org/10.3390/s110605769

Schirrmann, M., Giebel, A., Gleiniger, F., Pflanz, M., Lentschke, J., Dammer, K. H. (2016). Monitoring agronomic parameters of winter wheat crops with low-cost UAV imagery. *Remote Sensing*, *8*(9). https://doi.org/10.3390/rs8090706

Schwend, T., Beck, M., Prucker, D., Peisl, S., Mempel, H. (2016). Test of a PAR sensor-based, Dynamic regulation of LED lighting in greenhouse cultivation of Helianthus annuus. *European Journal of Horticultural Science*, *81*(3), 152–156. https://doi.org/10.17660/eJHS.2016/81.3.3

Sezen, B. (2003). Modeling Automated Guided Vehicle Systems in Material Handling. *Doğuş Üniversitesi Dergisi*, *2*(4), 207–216. https://doi.org/10.31671/dogus.2019.319

Sharma, A., Kumar, V., Shahzad, B., Tanveer, M., Sidhu, G. P. S., Handa, N., … Thukral, A. K. (2019). Worldwide pesticide usage and its impacts on ecosystem. *SN Applied Sciences*, *1*(11), 1–16. https://doi.org/10.1007/s42452-019-1485-1

Sheng, Y. (2008). Quantifying the size of a lidar footprint: A set of generalized equations. *IEEE Geoscience and Remote Sensing Letters*, *5*(3), 419–422. https://doi.org/10.1109/LGRS.2008.916978

Siegfried, W., Viret, O., Huber, B., Wohlhauser, R. (2007). Dosage of plant protection products adapted to leaf area index in viticulture. *Crop Protection*, *26*(2), 73–82. https://doi.org/10.1016/j.cropro.2006.04.002

Sofonia, J. J., Phinn, S., Roelfsema, C., Kendoul, F., Rist, Y. (2019). Modelling the effects of fundamental UAV flight parameters on LiDAR point clouds to facilitate objectives-based planning. *ISPRS Journal of Photogrammetry and Remote Sensing*, *149*(August 2018), 105–118. https://doi.org/10.1016/j.isprsjprs.2019.01.020

Solanelles, F., Escolà, A., Planas, S., Rosell, J. R., Camp, F., Gràcia, F. (2006). An Electronic Control System for Pesticide Application Proportional to the Canopy Width of Tree Crops. *Biosystems Engineering*, *95*(4), 473–481. https://doi.org/10.1016/j.biosystemseng.2006.08.004

Stajnko, D., Berk, P., Lešnik, M., Jejčič, V., Lakota, M., Štrancar, A., … Rakun, J. (2012). Programmable ultrasonic sensing system for targeted spraying in orchards. *Sensors (Switzerland)*, *12*(11), 15500–15519. https://doi.org/10.3390/s121115500

Stajnko, D., Lakota, M., Hočevar, M. (2004). Estimation of number and diameter of apple fruits in an orchard during the growing season by thermal imaging. *Computers*

and Electronics in Agriculture, *42*(1), 31–42. https://doi.org/10.1016/S0168-1699(03)00086-3

Sylvester, G. (2018). *E-agriculture in Action: Drones for Agriculture*.

Szczerba, R. J., Galkowski, P., Glickstein, I. S., Ternullo, N. (2000). Robust algorithm for real-time route planning. *IEEE Transactions on Aerospace and Electronic Systems*, *36*(3 PART 1), 869–878. https://doi.org/10.1109/7.869506

Tiemann, J., Schweikowski, F., Wietfeld, C. (2015). Design of an UWB indoor-positioning system for UAV navigation in GNSS-denied environments. In *2015 International Conference on Indoor Positioning and Indoor Navigation, IPIN 2015*. Institute of Electrical and Electronics Engineers Inc. https://doi.org/10.1109/IPIN.2015.7346960

Tiemann, J., Wietfeld, C. (2017). Scalable and precise multi-UAV indoor navigation using TDOA-based UWB localization. *2017 International Conference on Indoor Positioning and Indoor Navigation, IPIN 2017*, *2017-Janua*(September), 1–7. https://doi.org/10.1109/IPIN.2017.8115937

Triggs, B., Mclauchlan, P. F., Hartley, R. I., Fitzgibbon, A. W. (2000). *Bundle Adjustment-A Modern Synthesis*. Retrieved from http://www.inrialpes.fr/movi/people/Triggs

Tulldahl, H. M., Larsson, H. (2014). Lidar on small UAV for 3D mapping. In *Electro-Optical Remote Sensing, Photonic Technologies, and Applications VIII; and Military Applications in Hyperspectral Imaging and High Spatial Resolution Sensing II* (Vol. 9250, p. 925009). SPIE. https://doi.org/10.1117/12.2068448

Tumbo, S. D., Salyani, M., Whitney, J. D., Wheaton, T. A., Miller, W. M. (2002). INVESTIGATION OF LASER AND ULTRASONIC RANGING SENSORS FOR MEASUREMENTS OF CITRUS CANOPY VOLUME. *Applied Engineering in Agriculture*, *18*(3), 367–372.

Turner, D., Lucieer, A., Watson, C. (2011). Development of an unmanned aerial vehicle (UAV) for hyper resolution vineyard mapping based on visible, multispectral, and thermal imagery. *34th International Symposium on Remote Sensing of Environment - The GEOSS Era: Towards Operational Environmental Monitoring*.

Uto, K., Seki, H., Saito, G., Kosugi, Y. (2013). Development of uav-mounted miniaturure hyperspectral sensor system for agricultural monitoring. In *International Geoscience and Remote Sensing Symposium (IGARSS)* (pp. 4415–4418). https://doi.org/10.1109/IGARSS.2013.6723814

Van Henten, E. J., Van Dijk, G., Kuypers, M. C., Van Tuijl, B. A. J., Van Willigenburg,

L. G. (2000). Motion Planning for a Cucumber Picking Robot. *IFAC Proceedings Volumes*, *33*(19), 39–44. https://doi.org/10.1016/s1474-6670(17)40886-x

Vega, F. A., Ramírez, F. C., Saiz, M. P., Rosúa, F. O. (2015). Multi-temporal imaging using an unmanned aerial vehicle for monitoring a sunflower crop. *Biosystems Engineering*, *132*, 19–27. https://doi.org/10.1016/j.biosystemseng.2015.01.008

Verbeke, J., Debruyne, S., Leuven, K. (2017). Vibration analysis of a UAV multirotor frame, (February), 1–9.

Vergouw, B., Nagel, H., Bondt, G., Custers, B. (2016). The Future of Drone Use. *Asser Press*, *27*, 21–46. https://doi.org/10.1007/978-94-6265-132-6

Walklate, P. J., Cross, J. V., Richardson, G. M., Murray, R. A., Baker, D. E. (2002). Comparison of different spray volume deposition models using LIDAR measurements of apple orchards. *Biosystems Engineering*, *82*(3), 253–267. https://doi.org/10.1006/bioe.2002.0082

Wallace, L. O., Lucieer, A., Watson, C. S. (2012). *ASSESSING THE FEASIBILITY OF UAV-BASED LIDAR FOR HIGH RESOLUTION FOREST CHANGE DETECTION*.

Walter, J. D. C., Edwards, J., McDonald, G., Kuchel, H. (2019). Estimating Biomass and Canopy Height With LiDAR for Field Crop Breeding. *Frontiers in Plant Science*, *10*. https://doi.org/10.3389/fpls.2019.01145

WANG, F., CUI, J.-Q., CHEN, B.-M., LEE, T. H. (2013). A Comprehensive UAV Indoor Navigation System Based on Vision Optical Flow and Laser FastSLAM. *Acta Automatica Sinica*, *39*(11), 1889–1899. https://doi.org/10.1016/s1874-1029(13)60080-4

Wang, F., Huang, Z., Yu, H., Tian, X., Wang, X., Huang, J. (2013). EESM-based fingerprint algorithm for Wi-Fi indoor positioning system. *2013 IEEE/CIC International Conference on Communications in China, ICCC 2013*, (Iccc), 674–679. https://doi.org/10.1109/ICCChina.2013.6671197

Ward, S., Hensler, J., Alsalam, B., Gonzalez, L. F. (2016). Autonomous UAVs wildlife detection using thermal imaging, predictive navigation and computer vision. *IEEE Aerospace Conference Proceedings*, *2016-June*, 1–8. https://doi.org/10.1109/AERO.2016.7500671

Wei, J., Salyani, M. (2004). DEVELOPMENT OF A LASER SCANNER FOR MEASURING TREE CANOPY CHARACTERISTICS: PHASE 1. PROTOTYPE DEVELOPMENT. *Transactions of the ASAE*, *47*(6), 2101–2107.

Wen, S., Han, J., Ning, Z., Lan, Y., Yin, X., Zhang, J., Ge, Y. (2019). Numerical analysis

and validation of spray distributions disturbed by quad-rotor drone wake at different flight speeds. *Computers and Electronics in Agriculture*, *166*. https://doi.org/10.1016/j.compag.2019.105036

Wu, T., Chen, L. K., Hong, Y. (2016). A vision-based indoor positioning method with high accuracy and efficiency based on self-optimized-ordered visual vocabulary. *Proceedings of the IEEE/ION Position, Location and Navigation Symposium, PLANS 2016*, 48–56. https://doi.org/10.1109/PLANS.2016.7479682

Wu, X., Angeles, J., Zou, T., Yang, J., Li, H., Li, W. (2020). Trajectory Planning with Lamé-Curve Blending for Motor-Saturation Avoidance upon Mobile-Robot Turning. *IEEE Access*, *8*, 58483–58496. https://doi.org/10.1109/ACCESS.2020.2982740

Wu, Y., Qi, L., Zhang, H., Musiu, E. M., Yang, Z., Wang, P. (2019). Design of UAV downwash airflow field detection system based on strain effect principle. *Sensors (Switzerland)*, *19*(11). https://doi.org/10.3390/s19112630

Xu, Z., Li, D., B, S. S., Wang, Z., Jiang, J. Y. (2019). *Based Probability Prediction Method* (Vol. 1). Springer Singapore. https://doi.org/10.1007/978-981-10-6571-2

Yan, T., Zhu, H., Sun, L., Wang, X., Ling, P. (2018). Detection of 3-D objects with a 2-D laser scanning sensor for greenhouse spray applications. *Computers and Electronics in Agriculture*, *152*(April), 363–374. https://doi.org/10.1016/j.compag.2018.07.030

Yang, C., Shao, H.-R. (2015). WiFi-Based Indoor Positioning. *IEEE Communications Magazine*, *53*(March), 150–157.

Yang, F. B., Xue, X. Y., Zhang, L., Sun, Z. (2017). Numerical simulation and experimental verification on downwash air flow of six-rotor agricultural unmanned aerial vehicle in hover. *International Journal of Agricultural and Biological Engineering*, *10*(4), 41–53. https://doi.org/10.25165/j.ijabe.20171004.3077

Yang, G., Zhao, L., Dai, Y., Xu, Y. (2017). A KFL-TOA UWB indoor positioning method for complex environment. *Proceedings - 2017 Chinese Automation Congress, CAC 2017*, *2017-Janua*, 3010–3014. https://doi.org/10.1109/CAC.2017.8243291

Yao, L., Wang, Q., Yang, J., Zhang, Y., Zhu, Y., Cao, W., Ni, J. (2019). UAV-Borne dual-band sensor method for monitoring physiological crop status. *Sensors (Switzerland)*, *19*(4). https://doi.org/10.3390/s19040816

Zaman, Q. U., Schumann, A. W., Hostler, H. K. (2006). ESTIMATION OF CITRUS FRUIT YIELD USING ULTRASONICALLY-SENSED TREE SIZE. *Applied Engineering in Agriculture*, *22*(1), 39–44.

162

Zaman, Q. U., Schumann, A. W., Miller, W. M. (2005). VARIABLE RATE NITROGEN APPLICATION IN FLORIDA CITRUS BASED ON ULTRASONICALLY-SENSED TREE SIZE, *21*(3), 331–336.

Zhang, B., Tang, Q., Chen, L. ping, Xu, M. (2016). Numerical simulation of wake vortices of crop spraying aircraft close to the ground. *Biosystems Engineering*, *145*, 52–64. https://doi.org/10.1016/j.biosystemseng.2016.02.014

Zhang, L., Grift, T. E. (2012). A LIDAR-based crop height measurement system for Miscanthus giganteus. *Computers and Electronics in Agriculture*, *85*, 70–76. https://doi.org/10.1016/j.compag.2012.04.001

Zheng, Y., Yang, S., Liu, X., Wang, J., Norton, T., Chen, J., Tan, Y. (2018). The computational fluid dynamic modeling of downwash flow field for a six-rotor UAV. *Frontiers of Agricultural Science and Engineering*, *5*(2), 159–167. https://doi.org/10.15302/J-FASE-2018216

Zhou, L., Gu, X., Cheng, S., Yang, G., Shu, M., Sun, Q. (2020). Analysis of plant height changes of lodged maize using UAV-LiDAR data. *Agriculture (Switzerland)*, *10*(5). https://doi.org/10.3390/agriculture10050146

Appendix A

A.1 Connecting to UAV onboard computer

Ensure all the peripherals are connected to the onboard computer, and the WiFi module is plugged in the USB port of the onboard computer. Insert the battery into the UAV and turn on the power. Connect the GC (Ground Computer) to the available WiFi network and enable its hotspot. The system was configured to connect automatically with the onboard computer. Once the connection is established, the information will be displayed on the hotspot connection window (Figure 52).
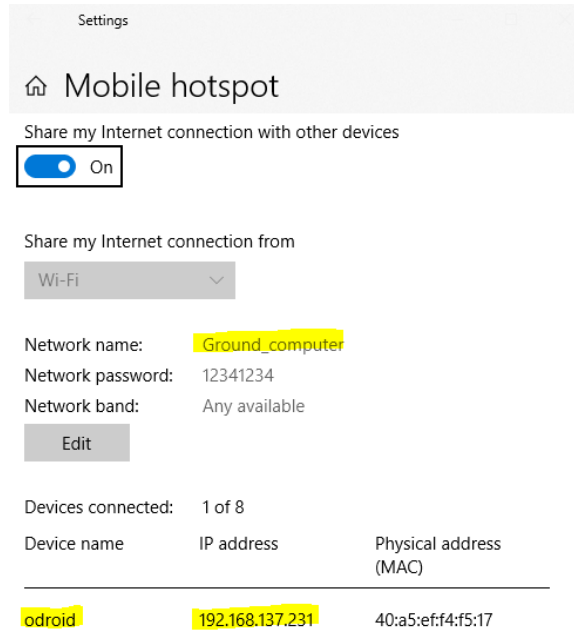
Figure 52. Hotspot window on GC displaying established connection with the onboard computer (odroid).

Run the **Aerial Sensing Platform** application in Qt, which will open the main window; an explanation of each pushbutton is available in the results section (Figure 19). Overall sequence of operation – Get greenhouse dimension by processing manual flight data, generate the flight plan based on the dimension and user's accuracy requirement, create flight commands, fly the UAV autonomously and process the flight data to get the point cloud data.

A.2 Extracting greenhouse dimension from manual flight

- Fly manually along the greenhouse boundary. Take replicates to get a better estimate or fly multiple times along the boundary within a single flight (Follow section A.3 Sequence of operation for manual flights for the recording manual flight data).

165

- Only IMU (orientation and linear acceleration) and Guidance (position and linear velocity) data are required for this analysis.

- Once data is available, send it to the ground computer for analysis and save in a dated folder, which can be later accessed in an orderly manner.

- Run *'greenhouse_dimension.m'* and the following window will appear

Figure 53. Dialog box for calculating greenhouse dimension.

- Enter the folder location where sensor data was saved, for example -

'C:\Aditya\MATLAB\Final_codes\Main\data\SAC_final_flights\mar_9\manual_fli ght\dimension'

- Enter the replicate number, followed accuracy requirement parameters such as – desired LiDAR scan width, UAV velocity, flight pattern, and overlapping percentage.

- Clicking OK will generate the greenhouse dimension and information needed for flight planning. It will be saved in a fixed location as indicated by *'Output Location'*, which will be later accessed by Qt to generate the plan.
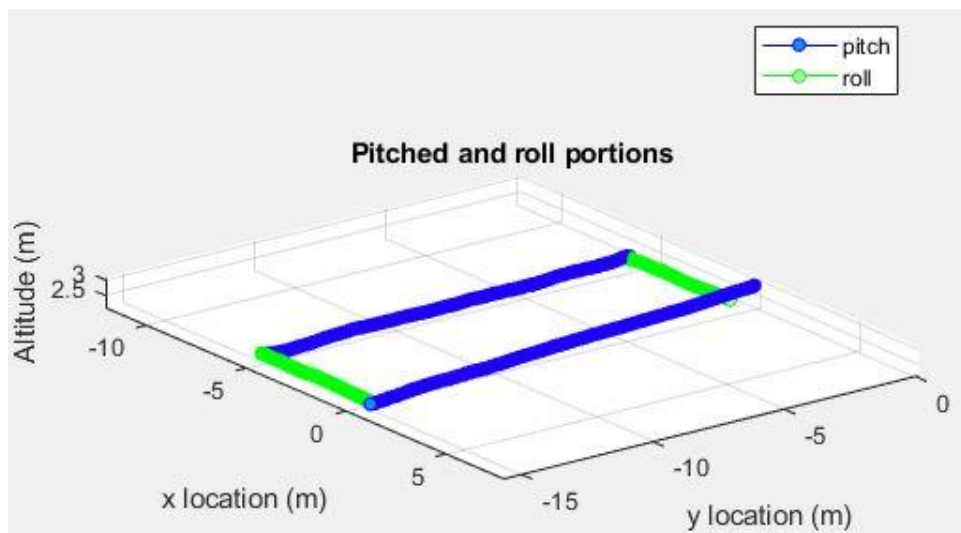
Figure 54. Pitched and rolled portion of the manual flight used for calculating the greenhouse dimensions.

A.2 Extracting the flight plan and generate commands

- Click ⊞ (import) button to read the greenhouse dimension.

- Click 🖩 (*calculator*) button to calculate the output parameter.

- Click 〰 (plot) button to plot the calculated flight path.

- Click ⌨ (*command*) button to generate flight commands.

167

- Click ✱ (*launch*) button to open flight control console.

A.3 Sequence of operation for manual flights

Once the flight control window is open, click the following pushbuttons (Id) described in Table 9 and Table 10–

- 1, 2, and 3 to enable all sensors.

- 5 and 6 to start saving sensor data and takeoff the UAV.

- Fly along the scan boundary by pitching along the length and rolling along the width. Ensure that the UAV heading is always maintained along the length and make corrections if the heading is unstable.

- 8 and 9 to land the UAV and stop recording.

  - o Recorded sensor data will be saved in two locations on the onboard computer – (a) /home/odroid/lidar_data/temp_sensor_data and (b) /home/odroid/lidar_data/temp_sensor_data_bkp

  - o Location (a) archives all flight records and location (Figure 55(a)). Location (b) keeps a record of current datasets (Figure 55(b)).

- 10 and turn off the UAV.

- Repeat step (1) to (6) for the number of times the user wants to scan the area.

- After completing the required number of scans (n) in the last scan before turning off the UAV, extract current flight data.

  - o Set *'Num of files'* to n (number of replications taken for one set)

  - o Click *'Extract and send to GC'* (Id = 11)

- o All the sensor data in location (b) will be processed (extract relevant sensor data, conversion from .bag to .txt format, creation of .zip file to combine all .txt file) and sequentially sent to fixed location of GC (C:\Aditya\Qt_file\Flight_command\UAV_odroid_data).
- o After the transfer of each dataset, it will be deleted from the onboard computer location (b).
- o After transferring all the recorded data, the information will be displayed on the Qt window (Figure 55(c)).

Figure 55. (a) Archive location on onboard computer to keep a record of older flights (timestamped)). (b) The current location saves the latest data, which are processed and deleted after completing an experiment. (c) Flight control window – set the num of files equal to the number of replicates taken in an experiment (shown in the red box), and post data transfer, the information is displayed in the Qt window (shown in the black box).

- Finally, the datasets are placed in a dated folder which MATLAB processes to generate point cloud data and greenhouse dimension. Once this information is available, the flight control application is used to fly the UAV autonomously.

A.4 Sequence of operation for autonomous flights

Below mentioned are the sequence id for autonomous flight and data recording.

- 4 to edit hover time (by default, it is set to 5 seconds).

- 1, 2, and 3 to enable all sensors, followed by 4 and 5.

- Click either 6 or 7 based on the type of altitude control to start the UAV flight. At the end of the last path, UAV will land, and the recording will stop automatically. (Currently, the auto-landing has been disabled to avoid UAV damage if the landing area is not clear). So, 8 to land the UAV post-flight completion.

- 10 and turn off the UAV. Repeat the above steps for the required number of replications.

- At the end of the experiment, specify the number of replication in 'Num of flight' input box and click *'Extract and send to GC'* to send the recorded sensor data to GC.

Appendix B

B.1 Extracting manual point cloud data

- Run *'manual_extraction.m'*, which will open a similar dialog box –

Figure 56. Dialog box for manual flight processing.

- Paste the folder location, for example -

'C:\Aditya\MATLAB\Final_codes\Main\data\nov30\owen\T3'

- Select the process (1) extract entire point cloud, (2) extract wall location (assuming walls are within LiDAR's range < 10 m), (3) extract log position, or (4) flight statistics

- Select the replication number range; by default, it processes 1st scan. Set the range as per requirement.

- Select the LiDAR angle, range, and viewing angle (mounting angle). By default, Guidance is set as height source.

- In the 'Enable yaw correction' type Y to remove error due to heading error. Figure 57 shows the effect of geometrical distortion correction in the flight path.
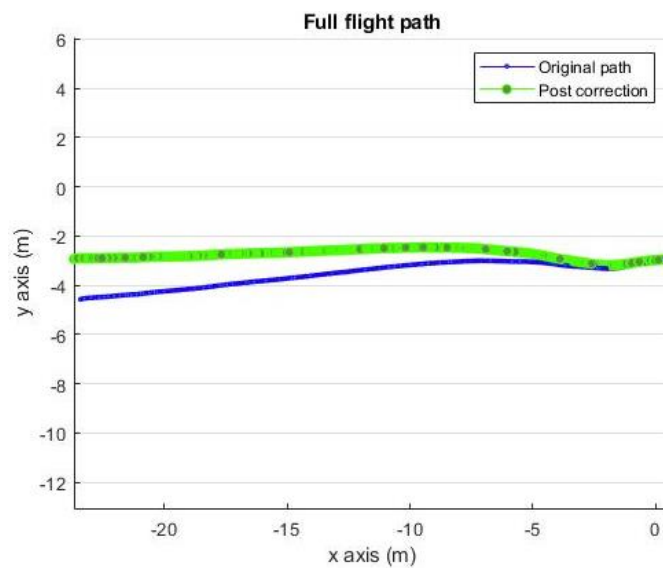
Figure 57. Geometrical distortion correction in the Guidance derived flight path.

- Selecting the entire point cloud option (1) will generate point cloud data (Figure 58) after error correction, which will be saved in the same folder location.
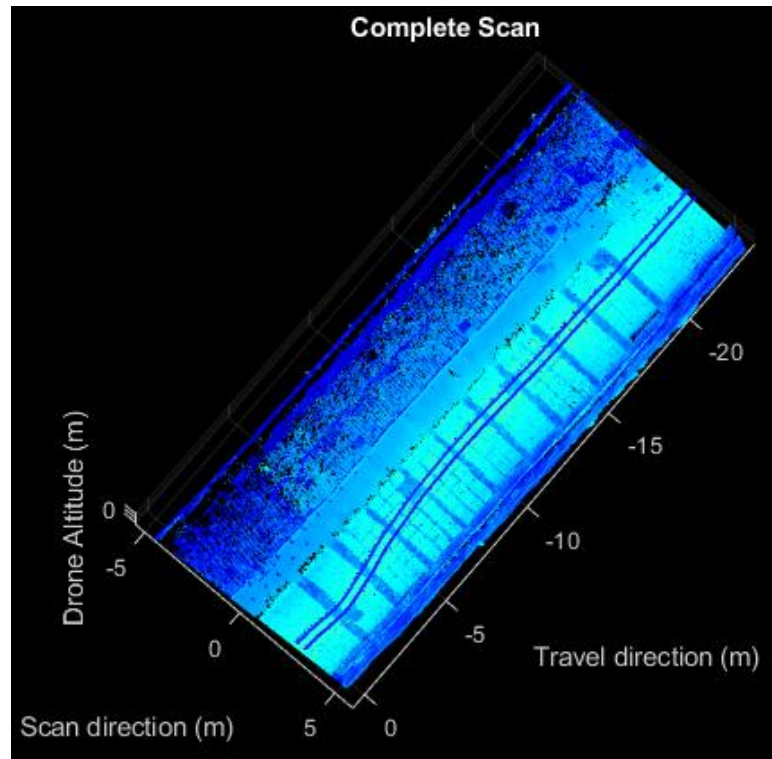
Figure 58. Output of point cloud data processing of manual flight

B.2 Extraction of the reference logs

- Run *'Complete_extraction.m'*, which will open the following window –

174
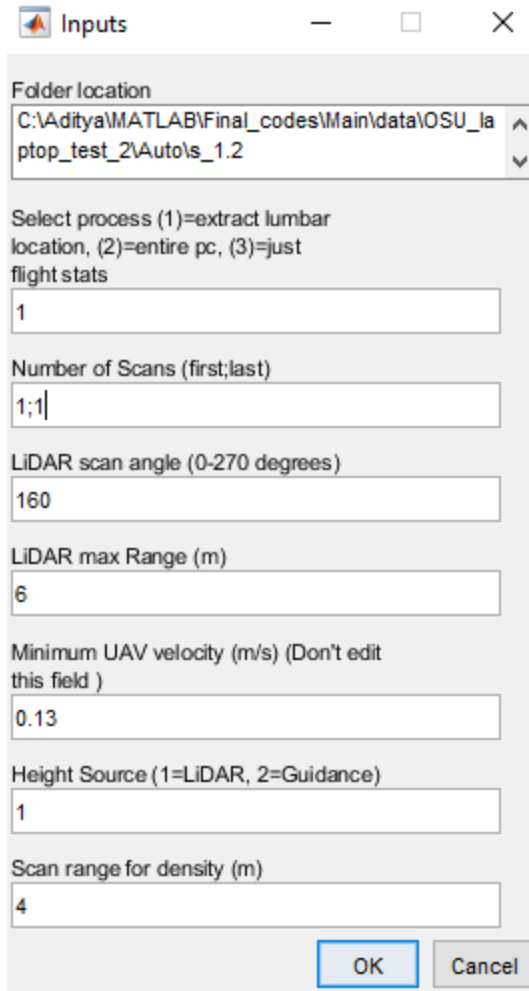
Figure 59. Dialog box for automated flight data processing with following inputs – (1) enter the location of the folder containing sensor data, (2) select the process, (3) select the number of replications to be processed, (4) set LiDAR scan angle and its maximum range, (5) the minimum UAV velocity before processing starts, (6) select the height source (1 for LiDAR and 2 for Guidance) and (7)scan range for density was used to calculate the point density within the given range of LiDAR (not evaluated).

- Enter the sensor data location and select process (1) extract lumbar location.

- Select the sensor for altitude correction either (1) LiDAR or (2) Guidance and click ok. Another dialog box will pop up asking the average z location of logs (which is pre-set by default); click ok to start the processing.

175
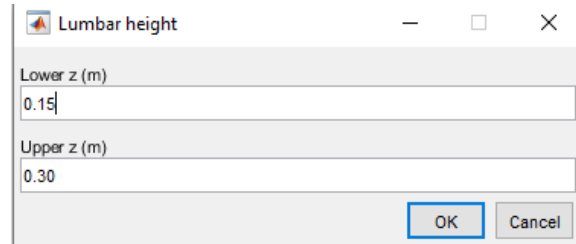
Figure 60. Approximate z location of logs

- The output (Figure 61) shows the location of logs in blue (located near the ground), the location of the UAV right arm in red (located near z = 2.0 m), and the Guidance location in green. Figure 62 shows the corresponding point cloud data of the scan area from which the logs and UAV arm were extracted.
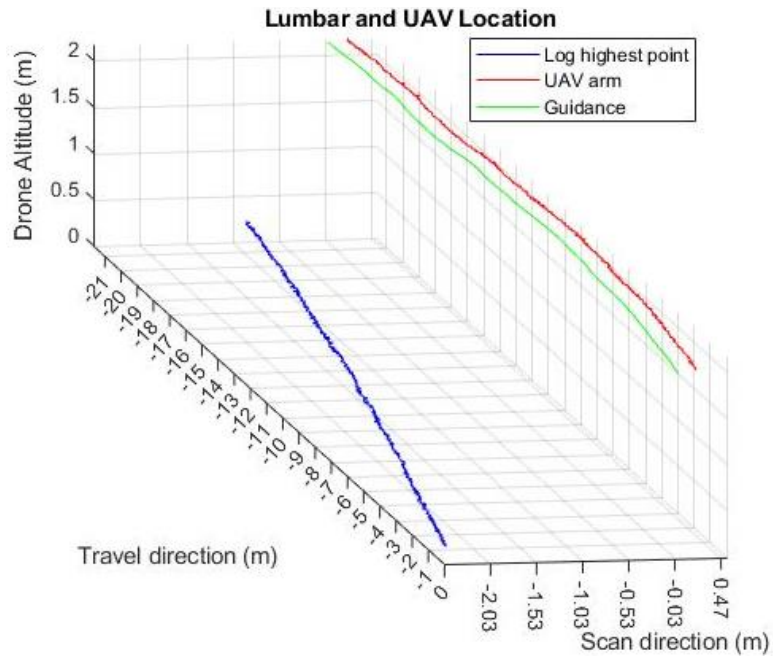
Figure 61. Location of wooden logs (blue), UAV right arm (red), and Guidance position (green), which were extracted from the point cloud data of the scan. In the next step, the UAV arm position was calculated relative to the log position.

176
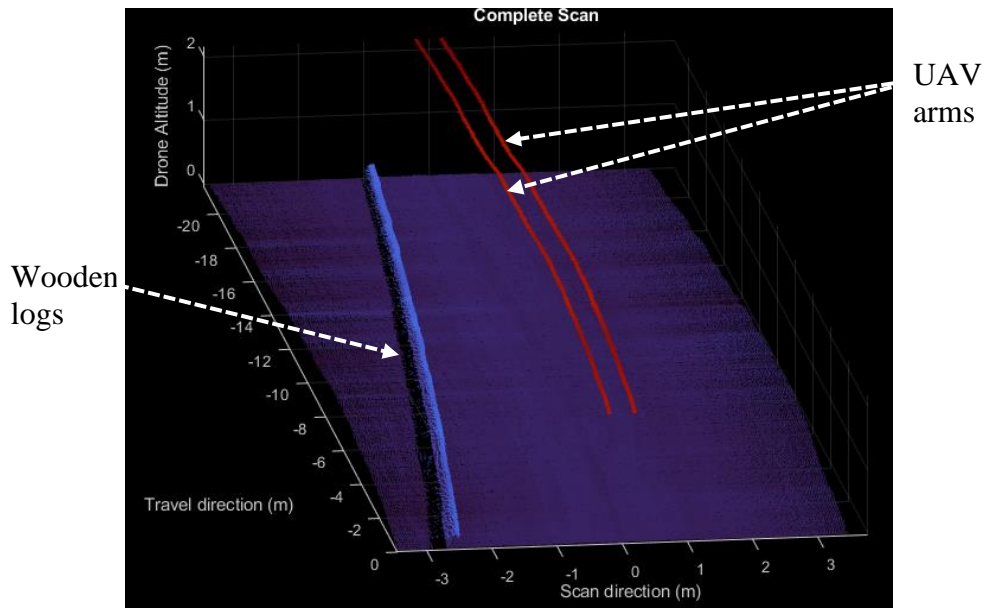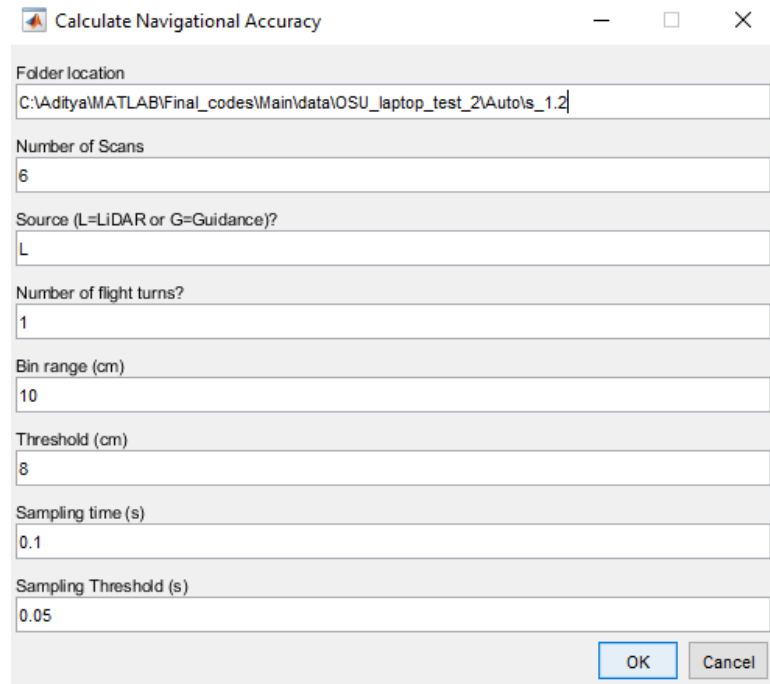
Figure 62. Corresponding point cloud data from which the wooden logs(bright blue) and UAV arm location (red) were extracted. The color variation is based on the relative height of the points.

- Post location extraction, the UAV arm location is calculated relative to the log

  location. Run *'Nav_accuracy_by_part.m'*, to get flight parameters at fixed

  distance (10 cm for this study). This will extract the UAV location relative to the

log position and calculate other flight parameters – speed, heading, LiDAR

height, and Guidance height.

Figure 63. Dialog box for 'Nav_accuracy_by_parts.m', enter the details as indicated by the prompt. The binning range was kept at 10 cm.

- Run *'drift_statistics_by_parts.m'* to plot flight data binned by distance. Figure 64

  shows the dialog box for the same, and the resulting plots (Figure 65) were

  displayed and saved in the same location as 'Folder location'.

Figure 64. Dialog box for 'drift_statistics_by_parts.m'. Enter the details as indicated by the prompts; it can also be used to visualize the variation in UAV speed, heading, LiDAR height, and Guidance height. However, for this study, only drift patterns were shown.
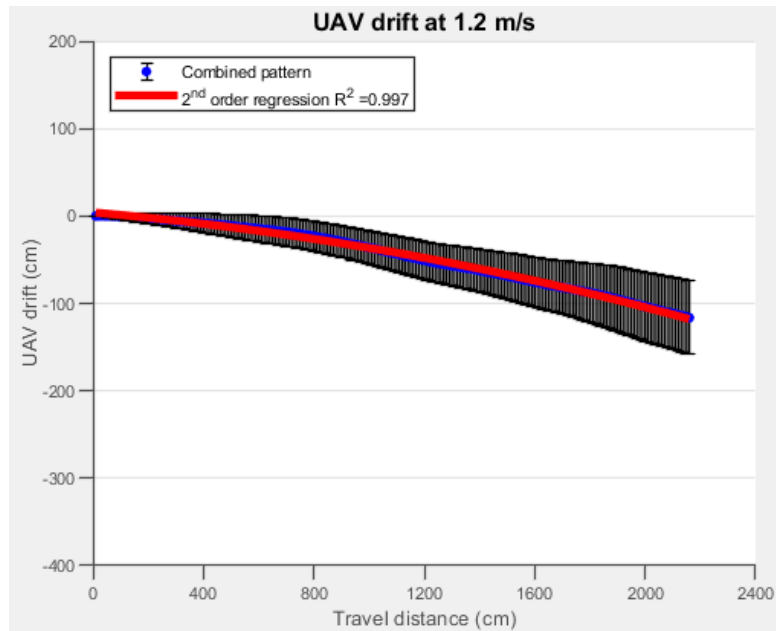
Figure 65. Resulting plot showing the combined flight path (blue) and deviation (error bars) among the replicates along with the second-order regression model of the flight path.

179

B.3 Extracting altitude from LiDAR measurements

- For the real-time altitude calculation from LiDAR measurements, two nodes were created in ROS (OCS) – (1) urg_node – to publish range and intensity data for the entire 270° sweep and (2) lidar_data – to calculate z component from the range data (the corresponding C++ code is mentioned below). The primary purpose of this code is to search in the 40° angular range from the LiDAR center, the point which corresponds to the ground (farthest z location).

```cpp
#include "ros/ros.h"
#include <cstdlib>
#include<sensor_msgs/LaserScan.h>
#include<geometry_msgs/PointStamped.h>
#include <stdio.h>
#include <stdlib.h>
#include <vector>
#include <iostream>
#include <math.h>
ros::Publisher loc_pub;
void chatterCallback(const sensor_msgs::LaserScan::ConstPtr&
msg)
{
  geometry_msgs::PointStamped loc;      // define location
which will hold altitude data
  int mid = 540, point_range = 80; //consider range of 160
points from LiDAR's center which corresponds to 40° angle
  float fact = 3.14159265 / 180 * 0.25; //convert point to
rad (each degree comprise 4 points, so each point
corresponds to 0.25 degree )
  std::vector< float > lid_arr;
  for (int i= mid - point_range; i <= mid + point_range;
i++) {
```

```cpp
        if (msg->ranges[i] < 10) {
            lid_arr.push_back(msg->ranges[i] * cos((i -
mid) * fact)); //find the z component of range
        }
        sort(lid_arr.begin(), lid_arr.end(),
std::greater<int>());//sort descending
    }

    loc.header.seq=msg->header.seq;
    loc.point.z = *min_element(lid_arr.begin(),
lid_arr.begin()+10); //choose the minimum among top 10
elements
    lid_arr.clear(); //clear the array for next iteration
    loc_pub.publish(loc);
}

int main(int argc, char **argv)
{

    ros::init(argc, argv, "lidar");
    ros::NodeHandle n;
    ros::Subscriber sub = n.subscribe("/scan", 10,
chatterCallback);
    loc_pub=
n.advertise<geometry_msgs::PointStamped>("/M100/",10);
    /**
     * ros::spin() will enter a loop, pumping callbacks.  With
this version, all
     * callbacks will be called from within this thread (the
main one).  ros::spin()
     * will exit when Ctrl-C is pressed, or the node is
shutdown by the master.
     */
    //ros::Rate rate(10);
    std::cout << "LiDAR height available" << std::endl;
    while(ros::ok())
    {
```

```
        ros::spin();
    }
       return 0;
    }
```

- The autonomous control algorithm then called this node (lidar_data) to receive real-time altitude from LiDAR measurement and control the UAV altitude.

B.4 Plant measurements

- Run *'Speed_track.m'* to extract point cloud data of the plant with ground removed. The code also corrects the mounting error of the drone on the speed track. Since the UAV was mounted manually, the 0° line of LiDAR was not vertical, causing the floor to tilt at an angle to the z-axis instead of being parallel. However, in the initial portion of the scan, the complete floor was visible and using this region, the floor angle was calculated. The entire scan was rotated by the same angle, making it parallel to the z-axis.

Figure 66. Dialog box for 'Speed_track.m' to extract point cloud data, post manual alignment error correction, and ground removal. The input prompts are self-explanatory and similar to previous dialog boxes.

- Owing to mounting error (Figure 67), it can be seen that the original scan had an

  error of 25 mm (Δz = absolute (33-8 = 25) for the same scan line), wherein at a

  given location of the platform (x = 1.21 m), the scan line was not aligned with the
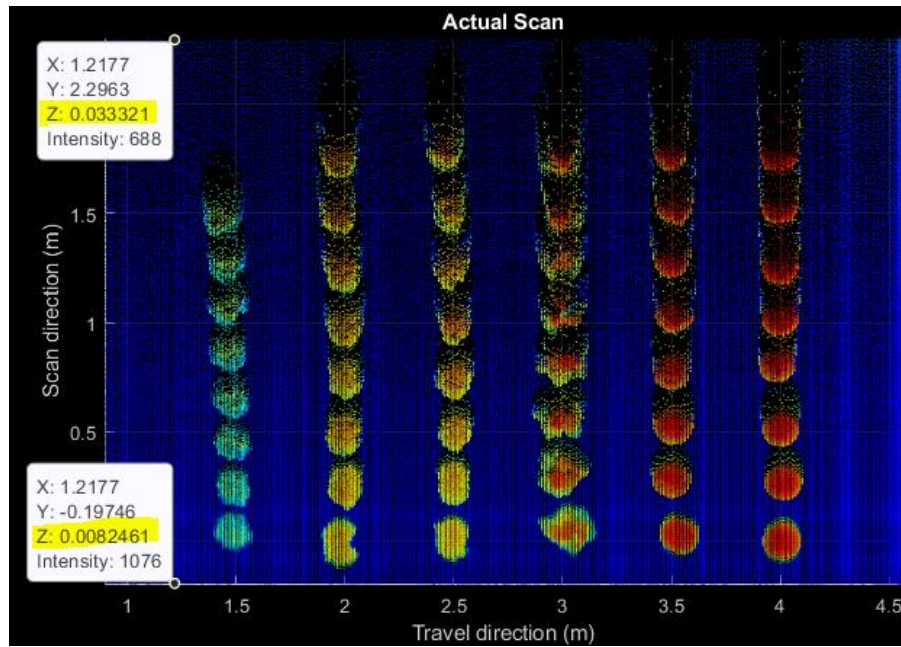
  z-axis.

183

Figure 67. Original scan wherein manual mounting led to alignment error between LiDAR 0° line (centerline) and z-axis, causing the floor to tilt by 25 mm (absolute(33-8) mm) about the x-axis.

- This angle was calculated by averaging the inclination (slope = $\Delta z/\Delta y$) of individual scan lines for the portion where the entire floor was visible. The entire scan was rotated about the x-axis by this angle. Post correction (Figure 68), this error reduced to 5 mm (Δz = absolute (6-11) = 5 mm).
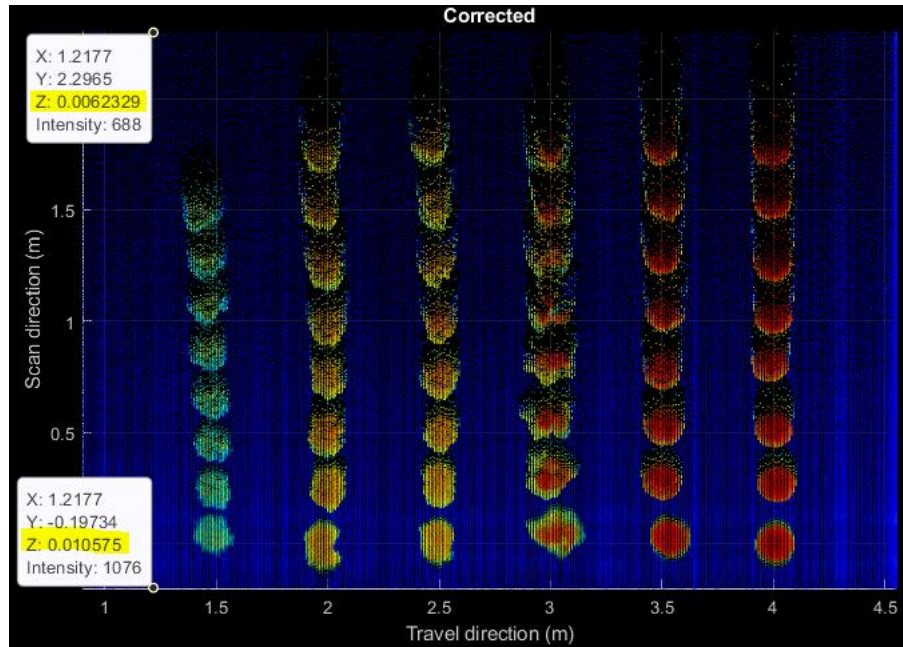
184

Figure 68. The output point cloud, post alignment correction along the z-axis, reduced the alignment error to 5 mm (absolute(6-10) mm).

- Finally, the code removed the ground data from the point cloud by fitting a plane along the z-axis and selecting the remaining dataset (Figure 69).
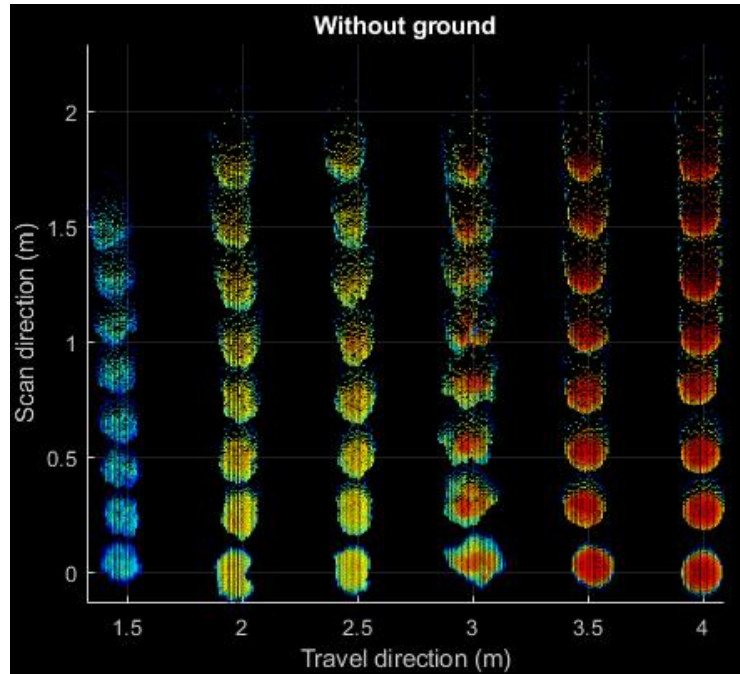
185

Figure 69. Ground removal from the point cloud by fitting a plane at the z-axis and selecting the remaining dataset.

- Run *'Clustering_with_Changing_Threshold.m'* to get the dimension of each object (by selecting appropriate threshold value ranging from 0.12 to 0.10), which was used for comparing plant data under propeller turned off and turned on. The dimension (height, width, length) of each object was grouped by its position and exported for comparison. The algorithm generated convex hull structures by clustering neighboring points (Figure 70).
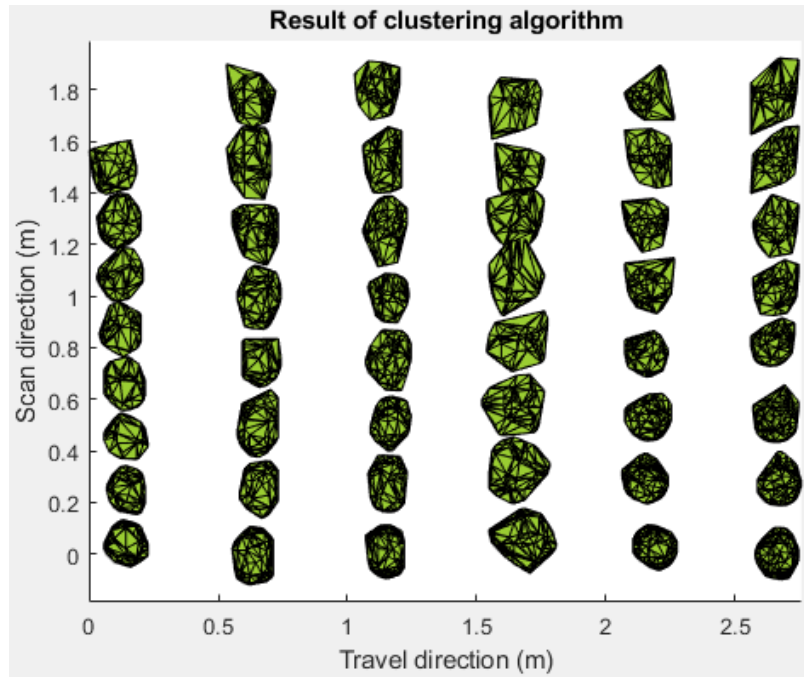
186

Figure 70. Output of clustering algorithm which generated a set of convex hull structures by grouping the neighboring points.

187